Self-energy corrected tight-binding framework in directed hybrid orbital basis from first principles

By

Manoar Hossain

Enrolment No: PHYS11201404006

National Institute of Science Education and Research, Bhubaneswar

A thesis submitted to the

Board of Studies in Physical Sciences

In partial fulfillment of requirements

for the Degree of

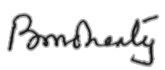DOCTOR OF PHILOSOPHY
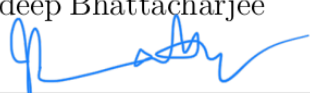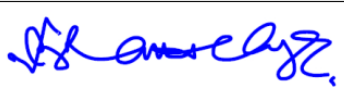
of

HOMI BHABHA NATIONAL INSTITUTE

August, 2021

Homi Bhabha National Institute

Recommendations of the Viva Voce Committee

As members of the Viva Voce Committee, we certify that we have read the dissertation prepared by **Manoar Hossain** entitled "**Self-energy corrected tight-binding framework in directed hybrid orbital basis from first principles**" and recommend that it may be accepted as fulfilling the thesis requirement for the award of Degree of Doctor of Philosophy.

Chairman - Prof. Bedangadas Mohanty		**Date** 15/02/2022
Guide/Convener - Dr. Joydeep Bhattacharjee		**Date** 15/04'22
Examiner - Prof. Saswata Bhattacharya		**Date** 15/02/2022
Member 1- Prof. Saroj Kumar Nayak		**Date** 15/02/2022
Member 2- Dr. Prasanjit Samal		**Date** 15/02/2022
Member 3- Dr. Anamitra Mukherjee	15/02/2022	**Date**

Final approval and acceptance of this thesis is contingent upon the candidate's submission of the final copies of the thesis to HBNI.

I/We hereby certify that I/we have read this thesis prepared under my/our direction and recommend that it may be accepted as fulfilling the thesis requirement.

Date: 15/02/2022

Place: NISER

Signature
Co-guide(if applicable)

Signature
Guide

STATEMENT BY AUTHOR

This dissertation has been submitted in partial fulfillment of requirements for an advanced degree at Homi Bhabha National Institute (HBNI) and is deposited in the Library to be made available to borrowers under rules of the HBNI.

Brief quotations from this dissertation are allowable without special permission, provided that accurate acknowledgement of source is made. Requests for permission for extended quotation from or reproduction of this manuscript in whole or in part may be granted by the Competent Authority of HBNI when in his or her judgment the proposed use of the material is in the interests of scholarship. In all other instances, however, permission must be obtained from the author.

Manoar Hossain

DECLARATION

I, hereby declare that the investigation presented in the thesis has been carried out by me. The work is original and has not been submitted earlier as a whole or in part for a degree / diploma at this or any other Institution / University.

Manoar Hossain

Manoar Hossain

List of Publications arising from the thesis

Journal

- **Published**

  1. "Transferability of self-energy correction in tight-binding basis constructed from first principles", **Manoar Hossain** and Joydeep Bhattacharjee, The Journal of Chemical Physics, 153(14):144103, **2020**.

  2. "Hybrid atomic orbital basis from first principles: Bottom-up mapping of self-energy correction to large covalent systems", **Manoar Hossain**, Joydev De, and Joydeep Bhattacharjee, The Journal of Physical Chemistry A, 125, 6805−6817, **2021**. *https://doi.org/10.1021/acs.jpca.1c00320*

- **Submitted to arXiv** (To be communicated soon)

  1. "Self-energy corrected tight binding parameters for few p-block semiconductors in the hybridized atomic orbital basis constructed from first principles", **Manoar Hossain** and Joydeep Bhattacharjee, *cond-mat.mtrl-sci*, arXiv:2106.10639, **2021**.

- **Manuscript under preparation**

  1. "Planar heterostructure of BC and CN embedded in graphene and hexagonal boron nitride for super-capacitor electrode applications", **Manoar Hossain** and Joydeep Bhattacharjee.

  2. "Self-energy corrected Hubbard U in magnetic carbon nano-structures", **Manoar Hossain** and Joydeep Bhattacharjee.

Conferences

1. **Manoar Hossain**. Current Trends in Condensed Matter Physics (CTCMP), 19th -22nd February, 2015, National Institute of Science Education and Research (NISER), Bhubaneswar

2. **Manoar Hossain**. Annual Condensed Matter Physics Meeting 2018, National Institute of Science Education and Research (NISER), Bhubaneswar

3. **Manoar Hossain**. Workshop and Symposium on Advanced Simulation Methods: DFT, MD and Beyond, March 6-10 2019, Indian Institute of Technology Delhi, New Delhi, India

4. **Manoar Hossain**. Fundamental Sciences and Quantum Technologies using Atomic Systems (FSQT), 28th September to 1st October, 2020, Physical Research Laboratory, Ahmedabad

5. **Manoar Hossain**. BerkeleyGW Tutorial Workshop and Berkeley Excited States Conference (BESC2021), 4-8 January 2021

Manoar Hossain

DEDICATIONS

Dedicated to

.....

My Grandparents

Akram Ali Mondal

Hasina Bibi

.....

.....

ACKNOWLEDGEMENTS

First of all, I would like to thank my family for their unconditional love and support as always. I would like to thank Prof. Joydeep Bhattacharjee for his immense support and guidance throughout my PhD journey, I am fortunate to have him as my PhD advisor. I am thankful to him for introducing the research problem(s) to me. His vision and ambition towards doing something new not only taught me how to handle pressure and keep going but also forced me to think out of the box and push the boundry of my comfort zone. He is my primary resource to get all my doubts and research questions answered. His constant support help me to crank out this thesis, all in one month.

I would like to express my sincere gratitude to my doctoral committee members Prof. Bedangadas Mohanty, Prof. Saroj Kumar Nayak, Prof. Prasanjit Samal and Prof. Anamitra Mukherjee for their valuable feedback and comments towards improvement of my research work.

I am fortunate enough to have excellent teachers throughout my carrier starting from my grandfather Late Ramzan Shaikh, "HATE KHORI" begins with him then the journey started, and from him I learnt all the basic mathematics beforehand.

I would also like to thank the Computational Materials Science Group members and all the members of theoretical condensed matter physics at NISER. I really had a lots of fruitful discussions with them which enriched and cultivated me a lot. I would like to mention our "Journal Club" and "Matter Matters" groups for beautiful and productive discussions. I shared a lots of fun memories and incidents with them too which made this journey bit easier.

I also thank my friends here at NISER, from AMU and from schools (too many to list out here but you know who you are!) for providing support and friendship that I needed.

Contents

SUMMARY

The goal of the thesis work has been to evolve methodologies for inexpensive computation of self-energy corrected electronic structure of experimentally realizable nano-systems which typically consist of thousands of atoms.

For calculation of electronic structures of materials Kohn-Sham(KS) density functional theory (DFT) has been widely used for bulk materials as well as finite systems with weak to modest correlation. However due to inherent defficiencies of the local-density based static approximation of exchange-correlation functionals used in DFT, it underestimate band gaps not only of correlated bulks with electrons in d or higher orbitals, but also of those with s and p valence electrons, and more importantly of finite systems with reducing system size owing to enhanced localization. Self-energy correction of KS single-particle levels calculated using the Green's function based GW approximation of many-body perturbation theory allows incorporation of explicitly constructed non-local dynamic dielectric function leading to a self-energy operator which comprehensively accounts for screening due to correlation, through a quasi-particle description of electrons. However the high computational cost prohibits GW approximations to be used in realistic systems beyond few tens of atoms. In my thesis work I find that instead of explicitly computing self-energy correction for large systems it is possible to effectively transfer self-energy correction from smaller isomorphic reference systems with similar atomic neighbourhoods through an appropriate tight-binding(TB) framework.

For effective transfer of self-energy correction to reproduce experimental bandgap through TB parameters we needed a TB basis which can describe bands above and below the Fermi energy, as done by the pure atomic orbtials and their hybrids. Recognising that in covlent systems the orientation and constitution of bonds are governed by the hybrid orbitals, a major part of the thesis is devoted to construction

of hybrid atomic orbitals as Wannier functions constructed from first principles as a set of localized orthonormal multi-orbital basis directed towards local coordination, followed by calculation of TB parameters in the proposed basis and incorporation of self-energy correction. Sections have been devoted to presenting an easy automated mapping scheme through which we tranfer TB parameters from smaller reference to larger target systems.

We demonstrated construction of the hybrid atomic orbital basis and transferability of TB parameters in it, including self-energy correction, in a representative range of covalent systems with sp^2 and sp^3 hybridized orbitals, namely, graphene and hexagonal boron nitride nano-ribbons and carbon, silicon, germanium and their hybrid nano-diamonds upto thousand atoms, for which TB parameters have been transferred from reference systems made of few tens of atoms. We also presented TB and self-energy correction TB parameters in a variety of p-block bulk semiconductors in diamond as well as zinc blende structures and discussed transferability of self-energy correction of TB parameters within blocks. We have also estimated the self-energy correction of the Hubbard U for the magnetic systems like ZGNR and finite graphene chunks. We have tested our scheme in a realistic length-scale where we calculated self-energy corrected quantum capacitance in a family of planar hybrid super-lattices made of hexagonal boron-carbide and carbon-nitride segments embedded in graphene and hexagonal boron nitride. As an ongoing work we are also working on simple model for the Coulomb-hole to account for screening in an inexpensive way.

List of Figures

Chapter 1

Preface

Computing energetics and spatial distribution of electrons in matter to understand their properties using quantum physics has been an evolving practise for almost over half a century now hand in hand with our increasing prowess in numerical computing infrastructure. However, the practice is no more confined within the community of computational condensed matter physicists and quantum chemists, but is being used as a tool to interpret results by experimentalists in the wider fraternity of materials science. Such a wide spread use brings all the efforts put in over the years to develop the computational framework for calculation of electronic structure of materials which is primarily based on the Kohn-Sham(KS) density functional theory(DFT)[1,2] close to fulfillment. The framework now evolves in an iteratively collaborative manner where the methodologies evolved by the computational quantum physicists and chemists are immediately put to test by the experimentalists making good of the huge strides in high performance computing, leading to further refinement.

Having established a fairly successful and robust framework for calculation of electronic structure of materials based on the mean-field and local approximation of the KS-DFT, a key direction of research, which has been continuously pursued by theorists in the condensed matter physics community, is to improve our grasp on the physics of interacting electrons beyond the mean-field approximations. This

is becoming particularly important to complement the huge progress made by the experimentalists to fabricate or synthesize low dimensional systems at nano-scale and study their electronic and magnetic properties towards applications.[3] The need to go beyond mean-field arises because the quantum mechanical interactions among the electrons are essentially non-local and dynamic in nature, which are amplified by the finiteness of their confinement with reduced size and dimensionality due to enhanced correlation, whereas the mean-field approximation of exchange-correlation functionals used in DFT are local and static. Furthermore, even for weak to moderately correlated bulks, due to the inherent lack of discontinuity of derivative of the local-density based approximation of exchange-correlation functionals used in DFT upon removal and addition of electron, DFT underestimates the band gaps estimated experimentally as the difference between the ionization potential and electron affinity.

To accurately estimate electronic structure from first principles particularly in systems where correlations are non-nominal, the quasi-particle nature of the electrons encompassing the effective holes due to its self-interaction, needs to be maximally incorporated beyond the ground state obtained using density-functional theory (DFT).[1,2] The non-local Green's functions are good alternatives to represent the non-local and dynamic effects of interaction among electrons accurately. Within the GW approximation[4,5,6] self-energy correction is estimated through correction to the exchange and Coulomb interactions due to dynamical screening incorporated through an explicitly computed non-local and dynamic dielectric function which also implicitly accounts for the derivative discontinuity lacking in the exchange-correlation functional used in DFT. However, due to the huge computational cost of calculating self-energy correction using GW approximation, its application in realistic scenarios, for example, the experimentally realizable nano-structures, which typically consists of thousands of atoms, has remained largely impossible. Key way forwards in this direction has been proposed[7,8] in recent years within the density functional tight-binding framework notwithstanding the difficulty in defining many electron interactions satisfactorily in terms of integrals covering few orbitals.

1.1   This thesis

The goal of my doctoral work has been to evolve methodologies for inexpensive computation of self-energy corrected electronic structure of experimentally realizable nano-systems which typically consists of thousands of atoms. A key finding of my thesis work is that instead of explicitly computing self-energy correction for large systems it is possible to effectively transfer self-energy correction from smaller isomorphic reference systems with similar atomic neighbourhoods through an appropriate tight-binding(TB) framework. However, for effective transfer of self-energy correction to reproduce experimental band-gap through TB parameters we needed a TB basis which can describe bands above and below the Fermi energy, as done by the pure atomic orbitals and their hybrids.

Constituting a major part of my thesis work, we have recently developed a method to numerically construct hybridized atomic orbitals based on as the approximate common eigenstates of finite first moment matrices through a self-consistently chosen gauge.[9,10] Wannier functions[11,12] constructed using the templates of hybridized atomic orbitals are directed towards the local atomic nearest neighbourhood of each atom in a given system and allow accurate extraction of multi-orbital tight-binding[13,14] parameters with all possible hopping present in the systems of concern through minimal number of terms. This method facilitate mapping of the multi-orbital tight-binding parameters calculated within the first principle calculations of electronic structure from smaller reference systems to much larger target systems with similar variety of atomic neighbourhood, based on mapping of neighbourhood up to second or third neighbours and projected Wannier charge centres of learned from reference systems. The mapping not only provides electronic structure of large systems at the level of Kohn-Sham density functional theory but also facilitate effective transfer of self-energy correction at the level of DFT+G_0W_0 from smaller reference systems to larger target systems for which an explicit computation of self-energy correction would be prohibitively expensive.

We started with demonstration of transferability in graphene and hexagonal boron nitride nano-ribbons in the basis of Wannier functions representing $2p_z$ electrons with modest success, and subsequently scaled up to the multi-orbital basis constituted by Wannier functions representing sp^3 hybridized orbitals to demonstrate transferability in finite nano-diamonds[15,16,17] made up of carbon, silicon, germanium and their hybrids with up to about a thousand atoms implying about 20 times escalation of system size. We also presented TB parameters and their self-energy correction in a representative variety of p-block bulk semiconductors in diamond and zinc blende structures and discussed transferability of self-energy correction of TB parameters within blocks. Transferability is tested not only through reproduction of band-gap at the quasi-particle level but also through match of the valence band width. For the magnetic systems like ZGNR systems we have also estimated self-energy correction of the Hubbard U term. Additionally, the proposed transfer of TB parameters do not require optimized structures of the large target systems. Using the mapping scheme we are able calculate self-energy corrected quantum capacitance in a family of planar hybrid systems made of boron-carbide or carbon-nitride embedded in graphene and hexagonal boron nitride we are proposing in my thesis.

On the methodological front, in tune with the central theme of my thesis whcich is to evolve inexpensive method to calculate the self-energy corrected electronic structure, we are also working on a model for the Coulomb-hole part of self-energy and derive an easily computable dielectric function which can also be used to screen the exchange. We hope that the thesis work will contribute towards paving the way for accurate computation of correlated electronic structure of finite systems in experimentally realizable length-scales typically consisting of thousands of atoms at the level of many-body perturbation theory from first principles.

Chapter 2

Theoretical background

2.1 Introduction

In this chapter I will summarily describe the computational methods used in this thesis to calculate electronic structure of systems dealt with. It is said that the atomic and molecular perspective of matter has been around from the ancient times. However, with the advent of the quantum theory of matter around the turn of the last century, the grand gateway to unravel the physics of matter beyond what could be seen through a microscope of the day, was opened to us, ushering the onset of the great journey that is still very much on, and traversing new landscapes which is growing more and more exotic by the day. The urge to connect physical and chemical properties of matter down to the valence electrons led us to evolve techniques to compute their energetics and distribution in matter, paving the way for emergence and progress of frameworks for computation of electronic structure of materials.

The journey in this direction began with the search of a solution to the exact many-electron Schrodinger equation, and evolves through a series of pragmatic approximations which made it possible to arrive at reasonable approximate solutions which are increasingly becoming accurate with methodological advancements and growing computational prowess. The first approximation is that of indepen-

dent electrons[18] wherein many electron wave-function could be written as combination of products of one electron wave-functions. Solving for these one-electron wave-functions which satisfies the many-electron Hamiltonian led to the Hartree-Fock(HF)[18,19] approach which led to realization of the Coulomb and exchange interactions, of which the second one being purely quantum in nature and was understood eventually to be central to ferro-magnetism. However the HF approach implemented within a fixed set of basis states crucially undermines correlation among electrons leading to incorrect estimation of energetics beyond atoms and small molecules. This problem is successfully circumvented by extending HF to the configuration interaction (CI) approach which however is computationally much more expensive than HF and almost impossible to perform for systems having few tens of atoms or so with even few thousands of computing cores. Similarly successful yet another computationally exorbitant extension of HF is the quantum Monte-Carlo approach. While these approaches were successful for small systems, their computational complication and cost nevertheless kept the capability of computing electronic structure confined only within the realm of generously funded research programs which could afford large computational infrastructure. The fraternity had to wait for the advent of the Kohn-Sham density functional theory (DFT) to break the ceiling.

As we discuss in this chapter, Kohn-Sham DFT is an exact theory which simplifies the complex N electrons Schrodinger equation to an effective single-particle equations where all the interaction of the single electron with all the other electrons, notwithstanding their self-interacting nature, can in principle be incorporated as a potential which must be derivable from a universal functional of the density of the ground state, implying essentially a self-consistent route to calculate the exact ground state. The observables of the many electron system can thus be obtain by solving the Kohn-Sham (KS) equation without knowledge of the full many-body wave function. However, since KS-DFT does not give any recipe to construct the universal functional, the efficacy of KS-DFT primarily depends on the correctness of formulation of the exchange-correlation functional in describing the many-electron

interaction in a given system. Formulations primarily in terms of the local density and their derivatives attempted so far have been widely successful to decribing electronic structure of systems with s and p valence electrons owing to their delocalized nature. However, to account for increased correlation due to localization on account of either occupation of d or higher orbitals or confinement in finite system, often the local density based approximations need to be supplemented by further corrections, either through adhoc model Hamiltonians or through a more elaborate self-consistent framework, namely, the many-body perturbation theory(MBPT). As discussed in this chapter, the GW approximation of MBPT has been adopted in my thesis work to dynamically account for the self-interaction correction. We also present a brief introduction of Wannier functions before we end this chapter since a major effort of my thesis work has been to point out the transferability of self-energy correction in terms of tight-binding parameters computed in the spatially localized hybrid atomic Wannier orbitals introduced in Chapters 3 and 4.

2.2   The many electron problem

In the most general form, the wave-function of non-relativistic interacting N electrons for a given set of nuclear coordinates is solution of the time-independent Schrodinger equation,

$$\hat{H}\psi(\{\mathbf{R}_I\}, \{\mathbf{x}_i\}) = E\psi(\{\mathbf{R}_I\}, \{\mathbf{x}_i\}), \tag{2.1}$$

where $\psi(\{\mathbf{R}_I\}, \{\mathbf{x}_i\})$ is the many-body wavefunction with position and spin coordinates of N electrons denoted as $\{\mathbf{x}_i\} \equiv \{\mathbf{r}_i, \sigma_i\}$ for $i = 1, 2, 3, \cdots, N$ as well as the position of M nuclei denoted as $\{\mathbf{R}_I\}$ for $I = 1, 2, 3, \cdots, M$. The many-body

Hamiltonian in Eq. 2.1 consists of five terms

$$
\begin{aligned}
\hat{H} &= \hat{T}_{\mathrm{n}}(\mathbf{R}) + \hat{T}_{\mathrm{e}}(\mathbf{r}) + \hat{V}_{\mathrm{nn}}(\mathbf{R}) + \hat{V}_{\mathrm{ee}}(\mathbf{r}) + \hat{V}_{\mathrm{ne}}(\mathbf{r}, \mathbf{R}) \\
&= -\frac{\hbar^2}{2} \sum_{I=1}^{M} \frac{1}{M_I} \nabla^2_{R_I} - \frac{\hbar^2}{2m_e} \sum_{i=1}^{N} \nabla^2_{r_i} + \frac{e^2}{4\pi\epsilon_0} \sum_{I}^{M} \sum_{J>I}^{M} \frac{Z_I Z_J}{|\mathbf{R}_I - \mathbf{R}_J|} \\
&\quad - \frac{e^2}{4\pi\epsilon_0} \sum_{I}^{M} \sum_{i}^{N} \frac{Z_I}{|\mathbf{R}_I - \mathbf{r}_i|} + \frac{e^2}{4\pi\epsilon_0} \sum_{i}^{N} \sum_{j>i}^{N} \frac{1}{|\mathbf{r}_i - \mathbf{r}_j|},
\end{aligned}
\tag{2.2}
$$

where the first term represents the kinetic energy of the nuclei with atomic numbers Z_I and nuclear masses M_I. The second term represents the kinetic energy of electrons with electron mass m_e and last three terms represent the interaction between nuclei-nuclei ($\hat{V}_{\mathrm{nn}}$), nuclei-electron ($\hat{V}_{\mathrm{ne}}$) and electron-electron ($\hat{V}_{\mathrm{ee}}$) respectively. In principle, by solving the above Schrodinger equation exactly one can get all the information about the system. Born-Oppenheimer approximation[20] which takes into account the fact that nucleus is much much heavier than the electrons and as a result move much slower compared to the electrons, separate the motion of nuclear and electronic degrees of freedom. Hence total wavefunction ψ can be written as a product of a nuclei part ψ_n and an electronic part ψ_e as

$$
\psi(\{\mathbf{R}_I\}, \{\mathbf{x}_i\}) = \psi_{\mathrm{n}}(\{\mathbf{R}_I\})\psi_{\mathrm{e}}(\{\mathbf{R}_I\}; \{\mathbf{x}_i\}).
\tag{2.3}
$$

With the help of Born-Oppenheimer approximation one can fix the nuclear configuration at some particular value $\mathbf{R}_c$ then solve the electronic wavefunction $\psi_{\mathrm{e}}(\{\mathbf{R}_c\}; \{\mathbf{x}_i\})$ which depends parametrically on R as:

$$
\hat{H}_{\mathrm{e}}\psi_{\mathrm{e}}(\{\mathbf{R}_I\}; \{\mathbf{x}_i\}) = E_{\mathrm{e}}\psi_{\mathrm{e}}(\{\mathbf{R}_I\}; \{\mathbf{x}_i\}),
\tag{2.4}
$$

where the corresponding Hamiltonian is given as

$$
\hat{H}_{\mathrm{e}} = -\sum_{i=1}^{N} \frac{1}{2}\nabla^2_i + \sum_{i}^{N} \sum_{j>i}^{N} \frac{1}{|\mathbf{r}_i - \mathbf{r}_j|} - \sum_{I}^{M} \sum_{i}^{N} \frac{Z_I}{|\mathbf{R}_I - \mathbf{r}_i|},
\tag{2.5}
$$

with $\hbar, e, m_e, 4\pi\epsilon_0$ all set to 1 as per the atomic unit system used in the thesis unless otherwise stated categorically.

The next level of approximation involves the fact that if we consider all electrons to see on the average a same effective potential due to all other electrons as in a jellium model, the Hamiltoanian becomes separable in the electron coordinates, implying that many electron wave-function $\psi_e(\mathbf{r}_1, \mathbf{r}_2, ...\mathbf{r}_N)$ can be written in terms of products of one electron wave-functions $\{\phi_i(\mathbf{r}_i), i = 1, 2, ...N\}$ or a combination of them. and eventually solve for each ϕ.

The first wave function based methods to solve the many-electron Schrodinger equation is the Hartree-Fock approximation,[18,19] which was first introduced by Hartree in 1928[18] where the many electron wavefunction is simply product of individual one electron wavefunctions, and then Fock generalized it by including the antisymmetric nature of wave function of electrons in 1930[19] to be consistent with the Pauli exclusion principle. In Hartree-Fock (HF) approximation we seek a solution for the many-electron wave-function in the form of a Slater determinant[21] made of N electrons in N orbitals $\psi^{\mathrm{HF}}(\mathbf{r}_1, ..., \mathbf{r}_N)$ as:

$$\psi^{\mathrm{HF}}(\mathbf{r}_1, ..., \mathbf{r}_N) = \frac{1}{\sqrt{N!}} \begin{vmatrix} \phi_1(\mathbf{r}_1) & \phi_1(\mathbf{r}_2) & \dots & \phi_1(\mathbf{r}_N) \\ \phi_2(\mathbf{r}_1) & \phi_2(\mathbf{r}_2) & \dots & \phi_2(\mathbf{r}_N) \\ \vdots & \vdots & \ddots & \vdots \\ \phi_N(\mathbf{r}_1) & \phi_N(\mathbf{r}_2) & \dots & \phi_N(\mathbf{r}_N) \end{vmatrix} \tag{2.6}$$

HF approximation gives reasonably accurate results for atoms and small molecules. However, not only the increasing computational cost but also the reduced accuracy due to underestimation of correlation, which restrict applications of HF beyond small molecules. In fact, with a single Slater determinant wave-function written for fixed set of basis, HF Hamiltonian incorporates only a static screening which does not have self-interaction and is exact for one electron. It is not possible to include dynamic screening in HF since wave-functions are not energy dependent. This problem is successfully circumvented by considering a combination of Slater determinant wave-

functions within in a variable configuration of basis sets whose range is a parameter of convergence. This approach, known as the configuration interaction (CI), still constitutes the *state-of-the-art* of accurate computation of electronic structure of materials but is also computationally extremely expensive and almost impossible to perform for systems having few tens of atoms or so with even few thousands of computing cores. The quantum Monte-Carlo approach where the Monte-Carlo algorithm is used to make choices for the basis sets with an appropriate weight-factor is another approach on the same footing. We will not go further in discussing these techniques since we take a different route, namely, the MBPT approach, to dynamically incorporate effects of correlation in my thesis work.

As a departure from dependency on $3N$ degrees of freedom, Thomas[22] and Fermi[23] independently proposed an approximate model with electron density as central variable influnce by an external potential. Unlike the $3N$ coordinates used in the many-body wave function, the electron density can be expressed with only a single position vector $\vec{r}$. However, the homogeneous approximation of the kinetic energy term in Thomas-Fermi(TF) model oversimplifies the inherent structure of the net effective potential and thereby unable to predict electronic properties for inhomogenous systems correctly. Nevertheless, the TF approach brought to the fore the possibility to replace wave-function based computation of electronic structure by a density based computation. About fifty years later, on a far more robust and exact footing the Kohn-Sham DFT brought the density to the core of computing electronic structure of materials.

2.3   Density Functional Theory

The theoretical formulation of DFT is based on two theorems given by Hohenberg and Kohn[1] which can be summarized as follows.

1. There exist a one-to-one correspondence between the external potential $V_{ext}(r)$ and the ground-state electron density $n_0(r)$. For any system of N interacting particles in an external potential $V_{ext}(r)$, the potential $V_{ext}(r)$ can be determined uniquely

from the ground state electronic density $n_0(r)$, except for a constant.

2. An universal functional $F[n]$ of the electronic density $n_0(r)$ can be defined, such that the ground-state energy, as a functional of the external potential $V_{ext}(r)$, $E_0[V_{ext}]$, can be derived with the help of variational principle.

Hohenberg-Kohn (HK) theorems suggest that the ground-state total energy of a system can be manifested as a functional of density, i.e., $E_{tot} = E_{tot}[n]$. With complete knowledge of the functional, Kohn and Sham (KS) DFT reduced a system of interacting electrons bound by some external potentials to a fictitious system of non-interacting particles known as the KS system of single particles, wherein a particle is subjected to a virtual external potential constructed such that the single-particle density as well as the total energy of the KS system would match those of the many-body interacting system. All the properties of the gound state can be derived from the KS single particle states $\{\phi_{i=1,N}\}$. However, the two theorems do not suggest any recipe to analytically construct the exact functional, which is thus a subject of realistic assumptions.

The universal density functional at the core of the KS framework can be written as follows

$$F[n] = T_{\mathrm{s}}[n] + E_{\mathrm{H}}[n] + E_{\mathrm{xc}}[n], \tag{2.7}$$

where,

$$n(\mathbf{r}) = \sum_{i=1}^{N} |\phi_i(\mathbf{r})|^2 \quad \text{and} \quad T_{\mathrm{s}}[n] = -\frac{1}{2}\sum_{i=1}^{N} \langle \phi_i | \nabla^2 | \phi_i \rangle. \tag{2.8}$$

The Hartree term:

$$E_{\mathrm{H}}[n] = \frac{1}{2} \int \int \frac{n(\mathbf{r})n(\mathbf{r}')}{|\mathbf{r} - \mathbf{r}'|} d\mathbf{r} d\mathbf{r}',$$

accounts for the total potential energy due to Coulomb repulsion among elctrons contributing to the net charge density $n(r)$. $E_{xc}[n]$, known as the exchange-correlation energy functional, incorporates all the other interactions, namely, the exchange interaction due to the Pauli exclusion principle and the effects of correlation, and is exclusively a matter of pragmatic speculative formulation.

Finally the KS total energy functional becomes:

$$E_{\text{KS}}[n] = T_{\text{s}}[n] + \int n(\mathbf{r})v_{\text{ext}}(\mathbf{r})d\mathbf{r} + E_{\text{H}}[n] + E_{\text{xc}}[n]. \qquad (2.9)$$

$E_{\text{KS}}[n] \equiv E_{\text{KS}}[\phi_1, \phi_2, ..., \phi_N]$ is variationally minimized with respect to ϕ_i with the N^2 orthonormality constraint:

$$\langle \phi_i | \phi_j \rangle = \delta_{i,j}$$

following the Euler Lagrange's equation through introduction of $\{\varepsilon_i\}$ as the undetermined multiplier as:

$$\frac{\delta}{\delta\phi_i^*}\left\{ E_{\text{KS}}[n] - \sum_j \varepsilon_j \langle \phi_j | \phi_j \rangle \right\} = 0, \qquad (2.10)$$

leading to Schrodinger like single-particle KS equation:

$$\hat{H}_{\text{KS}}\phi_i(\mathbf{r}) = \varepsilon_i \phi_i(\mathbf{r}), \qquad (2.11)$$

where

$$\hat{H}_{\text{KS}} = \sum_{i=1}^{\text{N}} \left[-\frac{1}{2}\nabla_i^2 + v_{\text{KS}}(\mathbf{r}_i) \right]. \qquad (2.12)$$

where the effective potential $v_{\text{KS}}(\mathbf{r})$ consists of three terms:

$$v_{\text{KS}}(\mathbf{r}) = v_{\text{ext}}(\mathbf{r}) + v_{\text{H}}(\mathbf{r}) + v_{\text{xc}}(\mathbf{r}), \qquad (2.13)$$

where, $v_{\text{H}}(\mathbf{r}) = \int \frac{n(\mathbf{r}')}{|\mathbf{r}-\mathbf{r}'|}d\mathbf{r}'$ is the Hartree potential and $v_{\text{xc}}(\mathbf{r}) = \frac{\delta E_{\text{xc}}}{\delta n(\mathbf{r})}$ is the exchange-correlation (XC) potential. The KS equation implies a self-consistent solution for $\{\phi_{i=1,N}\}$ as presented in Fig.2.2.

To compute $\{\phi_{i=1,N}\}$, they are expanded in a basis of either a set of linearly independent spatially localized orbitals like the atomic orbitals, or a set of plane waves $e^{i\vec{G}.\vec{r}}$ whose number is set by a kinetic energy cutoff $\hbar^2|\vec{G}|^2/2 \leq E_{cutoff}$. Since the core electrons confined within the core region defined by R_c, remain effectively
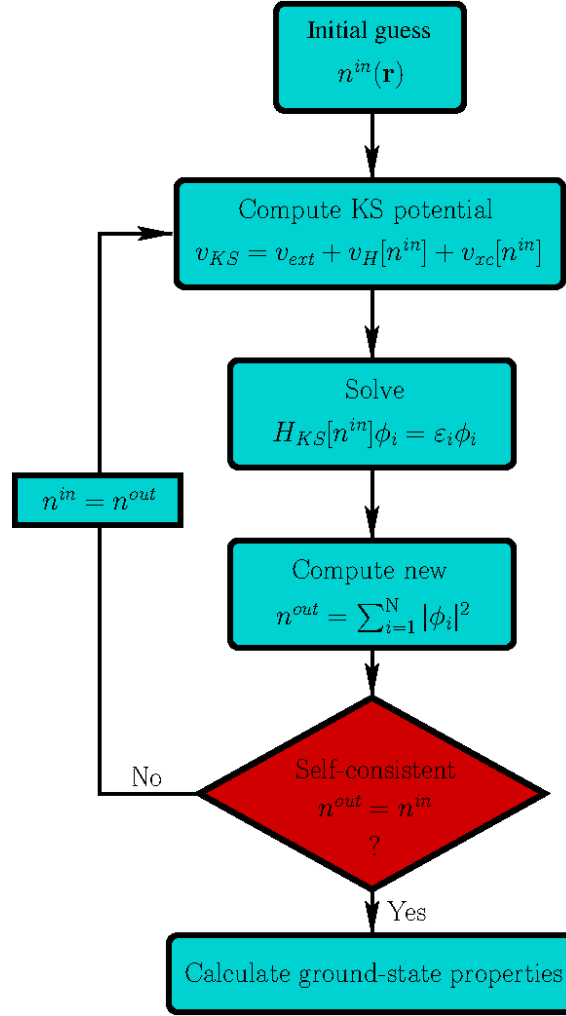
Figure 2.1: Flowchart for the iterative solution of the KS equation.

unaltered irrespective of chemical environment, they have negligible contribution in low energy properties such as chemical bonding, conductivity, optical excitation etc. The valence wave functions have complex nature in the core region $|r| < R_c$ due to the presence of nodes which demands a large set of plane wave basis and hence a large kinetic energy cutoff. In a standard DFT calculation, valence electrons are considered to be subjected to a pseudo-potential, so that the valence wave functions becomes smooth enough within the core region to be described by a reasonably small set of plane waves. These pseudopotentials are generated from all electron calculations of atoms such that the pseudo wave functions satisfy the properties of valence electrons outside the cutoff radius R_c. The accuracy of the pseudopotentials

depends on their 'transferability', which implies that the same pseudopotential of a given element can be used in various chemical environments to reproduce the different physical and chemical properties specific to the environments. Norm-conserving ones[24] are the most commonly used pseudopotential which, as the name suggests conserve the normalization of the pseudo wave function inside the core region so that the total charge remain preserved. Ultrasoft[25] pseudopotentials constitute the other set of commonly used variant of pseudopotentials, which maximally smoothen (delocalize) the pseudo wave functions inside the core region at the cost of deviation from conservation of total charge which can nevertheless be easily corrected.

The KS single particle energy eigenstates and their eigenvalues not only provide description of energetics and spatial distribution of electrons at the ground state within the approximation adopted for E_{xc}, but also scope for estimation of minimum energy configuration of materials. Hellmann-Feynman theorem enables computation of forces on atoms from the electronic structure of ground state. Atoms can be moved under the action of this forces to minimize total energy as per the Broyden-Fletcher-Goldfarb-Shanno(BFGS) scheme[26,27,28,29] Through successive computation of electronic structure and evolution of atomic configurations, structure of materials can be optimized towards the minimum energy configuration starting from a reasonable guess. For crystalline solids, total energy as a parameter of unit cell volume is further fit to Murnaghan[30] equation of state to estimate the size of the unit cell which minimizes the total energy. Notably, with all other contributions to the total energy described exclusively from first-principles, an initial set of coordinates of atoms and a formulation of the E_{xc} functional are thus the only input to the entire computational framework of KS DFT leading to determination of structure, energetics and thereby a wide range of physical and chemical properties at or near the ground state of a given material.

2.3.1 Exchange correlation

Among the several approximations of the exchange-correlation functional $E_{xc}[n]$ developed over the years, the oldest, simplest and also the most commonly used is the local density approximation (LDA), which was suggested by Kohn and Sham[2] The exchange-correlation functional $E_{xc}[n]$ of an inhomogeneous system of interacting electrons is approximated as that of a homogeneous electron gas with the same charge-density $n(r)$ at any point r. The exchange-correlation term in LDA approximation can be written as

$$E_{\mathrm{xc}}^{\mathrm{LDA}} = \int n(\mathbf{r})\epsilon_{\mathrm{xc}}(n(\mathbf{r}))d\mathbf{r}, \tag{2.14}$$

where $\epsilon_{\mathrm{xc}}(n(\mathbf{r}))$ is the XC energy density for the interacting electron gas of density $n(\mathbf{r})$. The LDA approximation reasonably reproduces experimentally observed structural and vibrational properties of weakly correlated systems. However, since LDA is rooted at the uniform electron gas, it inherently favours uniformity in distribution of charge density typical of metals, leading to delocalization charge away from atoms to interstitials which should strengthen covalent interactions in general. This results into over-binding of atoms, leading to overestimates the binding energies of molecules[31] as well as the cohesive energies of solids[32] and underestimates the bond lengths.[33] Most importantly, delocalization favored by LDA causes dispersion of bands which leads to underestimates the band-gap of semiconductors and insulators. To improve the accuracy, the gradient $\nabla n(\mathbf{r})$ of density is further included in formulating the approximation for exchange-corelation for systems having substantial inhomogeneities in density distribution. Introduced by Perdew and Wang,[34] this is known as generalized gradient approximation (GGA) whose functional form is adopted such that it can incorporate the correction over the LDA XC energy while following the exact sum rules. The exchange energy functional within GGA takes the form

$$E_{\mathrm{x}}^{\mathrm{GGA}} = \int n(\mathbf{r})\epsilon_{\mathrm{x}}(n(\mathbf{r}))F_{\mathrm{x}}^{\mathrm{GGA}}(s)d\mathbf{r}, \tag{2.15}$$

where $F_x^{GGA}(s)$ is the exchange enhancement factor which determines the enhanced exchange energy over the LDA for a given density and 's' is the dimensionless reduced density gradient

$$s = \frac{|\nabla n(\mathbf{r})|}{2\,(3\pi^2)^{1/3}\,n(\mathbf{r})^{4/3}}.\tag{2.16}$$

These approximate XC functionals (LDA, GGAs) are remarkably accurate in reproducing and predicting lattice constants, phonon structures, and a host of ground-state properties of wide band gap semiconductors of the p-block, as well as structure of molecules with covalent and ionic bonding primarily with s and p valence electrons. However, with increased correlation due to occupation of the d or higher orbitals which have sharper localization than the s and p electrons due to higher number of nodal plane and cones, the inadequacy of representation of correlation in LDA and GGA functionals which inherently borough from node-less charge distribution, show up as deviation of predicted properties from experimental observations. The LDA+U approach is reasonably successful in this regard but largely heuristic in nature. Hybrid functionals which partially incorporates exact exchange at the HF level has also been modestly successful.

However, in terms of matching the experimental band gap which is estimated as the difference between the ionization potential(IP) and the electron affinity(EA), both LDA and GGA fails even for the $2p$ block diamond and zinc-blende structures of bulk C, Si, BN etc. Fundamentally, these failures of LDA and GGA can be attributed to the inherent lack of discontinuity of the derivative of the local and static mean-field approximation of the exchange-correlation functional, upon addition or removal of electron. In reality, a new states starts getting filled or emptied once the electron number changes by one starting from some other integer value. As a result, the overall behaviour of the system is expected to change depending on the effect of the state with growing or depleted occupation on the interaction among electrons. However, the static nature of the XC functional used in LDA or GGA does not support any such change in the nature of many-electron interactions they represent. In principle, inclusion of dynamic correlation in the form of dynamic

screening should largely address this issue since it would in effect allow the inherent collective oscillatory (plasmonic) response of electrons to any evolution of charge density, much like ripples on the surface of water when we disturb it. In the next section I will discuss the GW approximation of many-body perturbation theory (MBPT), which naturally incorporates dynamical screening in the quasi-particle description of electron.

2.4 GW approximation of Many-body perturbation theory

In this section I aim to present a schematic overview of the GW approximation of the many-body perturbation theory based approach to dynamically account for self-energy correction. We will begin with general introduction of one particle Green's function and then derive the Dyson series for a generic one particle perturbation. We will then go over to the space-time Green's function as propagator and motivate the Lehman representation. Finally we will treat the two particle interaction term with a two particle Green's function and then express it in terms of the one particle Green's functions to obtain a self-energy operator which will account for the quasi-particle nature of electron due to self-interaction correction.

2.4.1 Prelude to Green's function

Let us start with time independent Schrodinger equation:

$$[H_0(\mathbf{r}) - E]\psi_0(\mathbf{r}) = 0 \tag{2.17}$$

The Green's function corresponding to Schrodinger equation(2.17) is defined as:[35]

$$[H_0(\mathbf{r}) - E]G_0(\mathbf{r}, \mathbf{r}', E) = -\delta(\mathbf{r} - \mathbf{r}') \tag{2.18}$$

where $G_0(\mathbf{r}, \mathbf{r}', E)$ satisfies the same boundary conditions as $\psi_0(\mathbf{r})$.

The primary reason for introduction of Green's function is to be able to solve inhomogeneous equation from the known solutions of the corresponding homogeneous equation. If we have a inhomogeneous equation of the form:

$$[H_0(\mathbf{r}) - E]\psi(\mathbf{r}) = f(\mathbf{r}) \tag{2.19}$$

where $f(\mathbf{r})$ is a known function, then $\psi(\mathbf{r})$ can be shown to be obtained as[36]

$$\psi(\mathbf{r}) = -\int f(\mathbf{r}')G_0(\mathbf{r}, \mathbf{r}', E)d\mathbf{r}' \tag{2.20}$$

Thus, knowing the Green's function we can have solution of the entire class of inhomogeneous differential equations whose homogeneous counterparts are same. Returning back to the definition of Green's function Eqn.(2.18) we note that it is the representation of the operator equation:

$$(E - \hat{H}_0)\hat{G}_0(E) = 1 \tag{2.21}$$

in the $\{|\mathbf{r}\rangle\}$ basis. Using the completeness of the $\{\psi_0\}$ we can derive the $\hat{G}_0(E)$ as:

$$\hat{G}_0(E) = \sum_n \frac{|\psi_{0n}\rangle\langle\psi_{0n}|}{E - E_n} \tag{2.22}$$

which, in the $\{|\mathbf{r}\rangle\}$ basis leads to:

$$\hat{G}_0(E, \mathbf{r}, \mathbf{r}') = \sum_n \frac{\psi_{0n}(\mathbf{r})\psi_{0n}(\mathbf{r}')}{E - E_n} \tag{2.23}$$

where, $\psi_{0n}(\mathbf{r})$'s and E_n's are the eigenfunctions and eigenvalues of H_0 respectively. Eqn.(2.23) allow us to represent $\hat{G}_0(E)$ in any other complete orthonormal basis. Now if:

$$f(\mathbf{r}) = -V(\mathbf{r})\psi(\mathbf{r}) \tag{2.24}$$

The solution[Eqn.(2.20)] using Green's function is given as:

$$\psi(\mathbf{r}) = \psi_0(\mathbf{r}) + \int G_0(\mathbf{r}, \mathbf{r}', E) V(\mathbf{r}') \psi(\mathbf{r}') d\mathbf{r}' \qquad (2.25)$$

which points to a recursive approach which results into an expansion in the order of V upon successive recursion(substitution of ψ on RHS by that of the LHS). Terminating the expansion at the linear order of V, as done in most cases,

$$\psi(\mathbf{r}) = \psi_0(\mathbf{r}) + \int G_0\left(\mathbf{r}, \mathbf{r}', E\right) V\left(\mathbf{r}'\right) \psi_0\left(\mathbf{r}'\right) d\mathbf{r}' + \mathcal{O}\left(V^2\right) \qquad (2.26)$$

In a compact notation successive recursion implies:

$$\begin{aligned}
\psi &= \psi_0 + G_0 V \psi_0 + G_0 V G_0 V \psi_0 + G_0 V G_0 V G_0 V \psi_0 + \cdots \\
&= \psi_0 + \left(G_0 + G_0 V G_0 + G_0 V G_0 V G_0 + \cdots\right) V \psi_0
\end{aligned} \qquad (2.27)$$

which further allows us write a net G as:

$$\begin{aligned}
G &= G_0 + G_0 V G_0 + G_0 V G_0 V G_0 + \cdots \\
&= G_0 + G_0 V \left(G_0 + G_0 V G_0 + \cdots\right)
\end{aligned} \qquad (2.28)$$

implying:

$$G = G_0 + G_0 V G \qquad (2.29)$$

using which we can obtain:

$$\psi(\mathbf{r}) = \psi_0(\mathbf{r}) + \int G(\mathbf{r}, \mathbf{r}', E) V(\mathbf{r}') \psi_0(\mathbf{r}') d\mathbf{r}'. \qquad (2.30)$$

In the sense of Taylor expansion, $G(\mathbf{r}, \mathbf{r}', E)$ can thus be understood as a linear response of $V(\mathbf{r}')$ to ψ at $(\mathbf{r})$.

Straight forward expansion of the above framework in the case of time dependent

Schrodinger equations:[37]

$$[i\partial_t - H_0(\mathbf{r})]\,\psi_0(\mathbf{r}, t) \;\; = \;\; 0 \tag{2.31}$$

$$[i\partial_t - H_0(\mathbf{r}) - V(\mathbf{r})]\,\psi(\mathbf{r}, t) \;\; = \;\; 0 \tag{2.32}$$

which lead to the definition of space-time Green's function as:

$$[i\partial_t - H_0(\mathbf{r})]G_0(\mathbf{r}, \mathbf{r}', E) \;\; = \;\; \delta(\mathbf{r} - \mathbf{r}')\delta(t - t'), \tag{2.33}$$

$$[i\partial_t - H_0(\mathbf{r}) - V(\mathbf{r})]G(\mathbf{r}, \mathbf{r}', E) \;\; = \;\; \delta(\mathbf{r} - \mathbf{r}')\delta(t - t'), \tag{2.34}$$

which are used to obtain:

$$\psi(\mathbf{r}, t) = \psi_0(\mathbf{r}, t) + \int G_0\left(\mathbf{r}, \mathbf{r}'; t, t'\right) V\left(\mathbf{r}'\right) \psi\left(\mathbf{r}', t'\right) d\mathbf{r}' dt', \tag{2.35}$$

$$\psi(\mathbf{r}, t) = \psi_0(\mathbf{r}, t) + \int G\left(\mathbf{r}, \mathbf{r}'; t, t'\right) V\left(\mathbf{r}'\right) \psi_0\left(\mathbf{r}', t'\right) d\mathbf{r}' dt'. \tag{2.36}$$

following Eqn.(2.30).

In case of time-dependent Schrodinger equation, where the Hamiltonian H does not depend on time (see Eqn.(2.32)), the Green's function does not depend individually on time t and t', but only on the difference $(t - t')$. Therefore, the Green's function which depends on $(t - t')$ can be defined as a Fourier transform of the energy-dependent Green's function as:

$$G\left(\mathbf{r}, \mathbf{r}', t - t'\right) = \frac{1}{2\pi} \int G\left(\mathbf{r}, \mathbf{r}', E\right) e^{-iE(t-t)/\hbar} dE \tag{2.37}$$

which is a solution of Eqn.(2.34). We can use a Green's function in $\mid \mathbf{r} \rangle$-representation similar to Eqn.(2.23) in the above equation:

$$G\left(\mathbf{r}, \mathbf{r}', t - t'\right) = \frac{1}{2\pi} \int \left\{ \sum_n \frac{\psi_n(\mathbf{r})\psi_n^*\left(\mathbf{r}'\right)}{E - E_n} \right\} e^{-iE(t-t')/\hbar} dE \tag{2.38}$$

which is an undefined integral unless the nature of the wavefunctions at the numer-

ator are known at the poles where the denominator vanishes. As a way forward, the integral is performed as a contour integral and the poles are shifted infinitesimally away from the real axis. Depending on how we shift the poles we define two new types of Green's functions: The so-called retarded Green's function:

$$\text{(i)} \quad G^{\mathrm{R}}\left(\mathbf{r},\mathbf{r}',E\right) = \sum_n \frac{\psi_n(\mathbf{r})\psi_n^*(\mathbf{r}')}{E - E_n + i\epsilon} \tag{2.39}$$

and the advanced Green's function:

$$\text{(ii)} \quad G^A\left(\mathbf{r},\mathbf{r}',E\right) = \sum_n \frac{\psi_n(\mathbf{r})\psi_n^*(r')}{E - E_n - i\epsilon} \tag{2.40}$$

whose physical interpretation becomes evident upon their Fourier transformation:

$$G^{\mathrm{R}}\left(\mathbf{r},\mathbf{r}',t-t'\right) = \sum_n \psi_n(\mathbf{r})\psi_n^*(\mathbf{r})\, e^{-iE_n(t-t')/\hbar} \quad (t > t')$$
$$= 0 \quad (t < t') \tag{2.41}$$

and

$$G^{\mathrm{A}}\left(r,r',t-t'\right) = -\sum_n \psi_n(\mathbf{r})\psi_n^*(\mathbf{r})\, e^{iE_n(t-t)/\hbar} \quad (t < t')$$
$$= 0 \quad (t > t') \tag{2.42}$$

respectively, as we note that in Eqn.(2.41) t is later than t' while in Eqn.(2.42) t is ahead of t'.

Interpretation of Green's function becomes clearer as we note that:

$$\psi(\mathbf{r},t) = \int G\left(\mathbf{r},\mathbf{r}';t,t'\right)\psi\left(\mathbf{r}',t'\right)d\mathbf{r}'dt'. \tag{2.43}$$

which we can verify through Eqn.(2.32) and Eqn.(2.34). This property of Green's function interprets it also as a propagator, since it facilitates description of the state of a particle at $\mathbf{r}$ at time t if we knew its description at $\mathbf{r}'$ at prior time t'. It is therefore obvious that the retarded Green's function is causal since $t > t'$ while the

advanced Green's function is anti-causal since $t' > t$.

2.4.2 Time ordered Green's function for N electrons

Generalizing the propagator interpretation of Green's function in the realm of N electrons systems, the generic one particle Green's function (describing propagation of one particle) is defined as:[5,36]

$$G_{\alpha\beta}(\mathbf{r}, t, \mathbf{r}', t') = -i\langle N, 0 \mid \hat{T}[\hat{\psi}_\alpha(\mathbf{r}, t)\hat{\psi}_\beta^\dagger(\mathbf{r}', t')] \mid N, 0\rangle \qquad (2.44)$$

where $\mid N, 0\rangle$ is an N electron ground state, $\psi_\alpha^\dagger(\mathbf{r}, t)$ and $\psi_\alpha(\mathbf{r}, t)$ are respectively the creation and annihilation field operator and $\hat{T}$ is time ordering operator to ensure that the sequence of operation of the operators from right to left are causal in time:

$$\begin{aligned}
\hat{T}\left[\hat{\psi}_\alpha(\mathbf{r}, t)\hat{\psi}_\beta^\dagger(\mathbf{r}', t')\right] &= \hat{\psi}_\alpha(\mathbf{r}, t)\hat{\psi}_\beta^\dagger(\mathbf{r}', t'), \quad t > t' \\
&= \pm\hat{\psi}_\alpha^\dagger(\mathbf{r}', t')\,\hat{\psi}_\beta(\mathbf{r}, t), \quad t < t'
\end{aligned} \qquad (2.45)$$

"+" sign is for bosons and "-" sign is for fermions which take care of the commutators and anticommutators conditions. Implying:

$$\begin{aligned}
iG(x, t, x', t') =\ & \langle N, 0 \mid \hat{\psi}(x, t)\hat{\psi}^\dagger(x', t')) \mid N, 0\rangle\theta(t - t') \\
& \pm\langle N, 0 \mid \hat{\psi}^\dagger(x', t')\hat{\psi}(x, t)) \mid N, 0\rangle\theta(t' - t)
\end{aligned} \qquad (2.46)$$

where, $\theta(t - t')$ is a step function. We have denoted $\mathbf{r}, \alpha \Rightarrow x$; $\mathbf{r}', \beta' \Rightarrow x'$ and $\sum_{spin} \alpha \int d\mathbf{r} \Rightarrow \int dx$.

2.4.3 Lehman representation

Adopting the Heisenberg picture[38] for field operator $\hat{\psi}(x, t)$:

$$\hat{\psi}(x, t) = e^{\frac{i\hat{H}t}{\hbar}}\hat{\psi}(x)e^{-\frac{i\hat{H}t}{\hbar}} \qquad (2.47)$$

and using the completeness condition:

$$\sum_j \mid M, j\rangle\langle M, j \mid = 1 \tag{2.48}$$

along with

$$\hat{H}|N,0\rangle = E_N^0|N,0\rangle \qquad \text{and} \qquad \hat{H} \mid M, j\rangle = E_M^j \mid M, j\rangle \tag{2.49}$$

where $j \geq 0$ being the order of the M electron state, we take the Fourier transform of $G(x, x', t, t')$ as in Eqn.(2.46) to obtain the energy dependent Green's function as

$$G(x, x', E) = \sum_j \left\{ \frac{\langle N, 0 \mid \hat{\psi}(x) \mid N+1, j\rangle\langle N+1, j \mid \hat{\psi}^\dagger(x') \mid N, 0\rangle}{E - (E_{N+1}^j - E_N^0) + i\delta} \right.$$
$$\left. \pm \frac{\langle N, 0 \mid \hat{\psi}^\dagger(x') \mid N-1, j\rangle\langle N-1, j \mid \hat{\psi}(x) \mid N, 0\rangle}{E + (E_{N-1}^j - E_N^0) - i\delta} \right\} \tag{2.50}$$

where the denominators can be interpreted as:[36]

$$E - (E_{N+1}^j - E_N^0) = E - (E_{N+1}^j - E_{N+1}^0) - (E_{N+1}^0 - E_N^0)$$
$$= E - \epsilon_{N+1}(j) - \mu \tag{2.51}$$
$$E + (E_{N-1}^j - E_N^0) = E + (E_{N-1}^j - E_{N-1}^0) + (E_{N-1}^0 - E_N^0)$$
$$= E + \epsilon_{N-1}(j) - \mu \tag{2.52}$$

$\epsilon_{N\pm 1}(j)$ being the excitation energy to the j-th excited $N \pm 1$ particle state and μ is chemical potential defined here as $(E_{N+1}^0 - E_N^0)$ or $(E_{N-1}^0 - E_N^0)$.

In the basis of plane waves:

$$\hat{\psi}(x) = \sum_k e^{ikx}\hat{b}_k$$

$$\hat{\psi}^\dagger(x) = \sum_k e^{-ikx}\hat{b}_k^\dagger \tag{2.53}$$

$$\hat{p} = \sum_k \hbar k \hat{b}_k^\dagger b_k$$

where $(\mathbf{k}, \alpha)$ is denoted as k. In a analogy with the Heisenberg transformation we can rewrite the field operator in terms of the momentum operator as:

$$\hat{\psi}(x) = e^{-ipx/\hbar}\hat{\psi}(0)e^{ipx/\hbar} \tag{2.54}$$

Substituting above equation into Eqn.(2.50) we get

$$
\begin{aligned}
G(x - x', E) &= \sum_j \Bigg\{ \frac{e^{ip_j(x-x')/\hbar}|\langle N, 0|\hat{\psi}(0)|N+1, j\rangle|^2}{E - \epsilon_{N+1}(j) - \mu + i\delta} \\
&\pm \frac{e^{-ip_j(x-x')/\hbar}|\langle N, 0|\hat{\psi}^\dagger(0)|N-1, j\rangle|^2}{E + \epsilon_{N-1}(j) - \mu - i\delta} \Bigg\}
\end{aligned}
\tag{2.55}
$$

with momentum p_j correspond to the $N \pm 1$ particle system at jth excited state. Using Fourier transformation from real space to momentum space

$$G(k, E) = \int G(x - x', E)e^{-ik(x-x')/\hbar}d(x - x') \tag{2.56}$$

we can write Eqn.(2.55) in k-space as:

$$G(k, E) = \sum_j \left\{ \frac{|\langle N, 0|\hat{\psi}(0)|N+1, j, k\rangle|^2}{E - \epsilon_{N+1}(j, k) - \mu + i\delta} \pm \frac{|\langle N, 0|\hat{\psi}^\dagger(0)|N-1, j, -k\rangle|^2}{E + \epsilon_{N-1}(j, -k) - \mu - i\delta} \right\} \tag{2.57}$$

where $\pm k$ in $|N \pm 1, j, \pm k\rangle$ is introduced for momentum $\pm \vec{k}$ of a particle in the jth excited level of $|N \pm 1\rangle$ system. This expression of Green's function is known as the Lehman's representation which facilitates an easy description of interact-

ing electrons. This is understood by noting that in the non-interacting regime creation(annihilation) of an electron at any unoccupied(occupied) level, will not impact the levels themselves, implying that $\langle N, 0|\hat{\psi}(0)$ will have non-zero overlap with $|N+1, j = n(k)+1, k\rangle$, $n(k)$ being the order of the highest occupied level at k in $|N, 0\rangle$. This will simple render poles at the $E = E(j = n(k)+1, k)$. However, in the interacting regime, $\langle N, 0|\hat{\psi}(0)$ will have non-negligible overlap with a wide range of values of j simply because the states calculated with N interacting electrons constitute a different subspace from that constituted by states calculated with $N+1$ interacting electrons.

For interacting electrons the momentum will spread among the other electrons, so the state label j will be more of a continuous variable(E) than a discrete set of states. therefore, it is meaningful to convert the discrete sum over j to integration over E as follow

$$\sum_j \frac{|\langle N+1, j, \mathbf{k}|\hat{\psi}^\dagger(0)|N, 0\rangle|^2}{E - \epsilon_{N+1}(j, \mathbf{k}) - \mu + i\delta} \Rightarrow \int_0^\infty \frac{A(k, E')}{E - E' - \mu + i\delta} dE' \qquad (2.58)$$

therefore, we can rewrite Eqn.(2.57) as:

$$G(k, E) = \int_0^\infty \left[\frac{A(k, E')}{E - E' - \mu + i\delta} \pm \frac{B(k, E')}{E + E' - \mu - i\delta} \right] dE' \qquad (2.59)$$

where, A and B in the above equation are called the spectral weight functions. The spectral weight function can be defined as[6] $A(k, E) = \frac{1}{\pi}|ImG(k, E)|$. This expression of Green's function in terms of the spectral weight functions is also a popular form of Lehman representation, which facilitates an easy interpretation of interacting electrons as quasi-particles marked by a spatially localized structure of the weight functions. Note that for the non-interacting electrons the weight functions are perfect delta functions at the poles.

2.4.4 Two body interaction

Let us consider a generic two body interaction as the perturbation. The Hamiltonian is given as[38]

$$\hat{H}(x_1, t_1) = \hat{H}_0(x_1) + v(x_1, x_2)\delta(t_1 - t_2) \tag{2.60}$$

where $\hat{H}_0(x_1)$ is the one-particle part of the Hamiltonian and $v(x_1, x_2)$ can be the coulomb interaction i.e., $\frac{e^2}{|\vec{r_1} - \vec{r_2}|}$.

In Heisenberg picture the field operator $\hat{\psi}(x_1, t_1)$ has the equation of motion

$$i\hbar \frac{\partial}{\partial t}\hat{\psi}(x_1, t_1) = [\hat{\psi}(x_1, t_1), \hat{H}] \tag{2.61}$$

Using field operators the above Hamiltonian can be rewritten as:

$$\hat{H} = \int \hat{\psi}^\dagger(x, t)\hat{H}_0(x)\hat{\psi}(x, t)dx + \int \hat{\psi}^\dagger(x, t)\hat{\psi}^\dagger(x', t') \times$$
$$v(x, x')\delta(t - t')\hat{\psi}(x', t')\hat{\psi}(x, t)dxdx' \tag{2.62}$$

With this representation of $\hat{H}$ the equation of motion becomes:

$$i\hbar \frac{\partial}{\partial t_1}\hat{\psi}(x_1, t_1) = \left\{\hat{H}_0(x_1) + \int v(x_1, x_3)\hat{\psi}^\dagger(x_3, x_1)\hat{\psi}(x_3, t_1)dx_3\right\}\hat{\psi}(x_1, t_1) \tag{2.63}$$

multiplying the above equation by field operator $\hat{\psi}^\dagger(x_2, t_2)$ from right with proper introduction of time ordering operator $\hat{T}$ and then taking expectation values with respect to ground state, we get

$$[i\hbar \frac{\partial}{\partial t} - \hat{H}_0(x_1)]G(x_1, t_1, x_2, t_2)$$
$$+ i\int v(x_1, x_3)\langle N|\hat{T}[\hat{\psi}^\dagger(x_3, t_1)\hat{\psi}(x_3, t_1)\hat{\psi}(x_1, t_1)\hat{\psi}^\dagger(x_2, t_2)]|N\rangle dx_3$$
$$= \hbar\delta(x_1 - x_2)\delta(t_1 - t_2) \tag{2.64}$$

Above equation can be interpreted as:[36]

Non-interacting one-particle term + interaction term $= \hbar\delta(x_1 - x_2)\delta(t_1 - t_2)$

If we have exactly soluble non-interacting Hamiltonian, namely:

$$[i\hbar\frac{\partial}{\partial t} - \hat{H}_0(x_1)]G_0(x_1, t_1, x_2, t_2) = \hbar\delta(x_1 - x_2)\delta(t_1 - t_2) \qquad (2.65)$$

where $G_0(x_1, t_1, x_2, t_2)$ is the non-interacting Green's function corresponding to $\hat{H}_0(x_1)$, as in our case where we use DFT to represent the non-interacting regime, we can then focus on the interaction term, which, on account of the two particle interaction term naturally involve a two particle Green's function:

$$\langle N|\hat{T}[\hat{\psi}^\dagger(x_3, t_1)\hat{\psi}(x_3, t_1)\hat{\psi}(x_1, t_1)\hat{\psi}^\dagger(x_2, t_2)]|N\rangle \qquad (2.66)$$

defined as

$$G_2(x_1, t_1, x_2, t_2, x_3, t_3, x_4, t_4)$$

$$=$$

$$(i)^2\langle N|\hat{T}[\hat{\psi}(x_1, t_1)\hat{\psi}(x_3, t_3)\hat{\psi}^\dagger(x_4, t_4)\hat{\psi}^\dagger(x_2, t_2)|N\rangle$$

Thus, equation of motion for the single-particle Green's function contains the two-particle Green's function on account of the two body interaction term. We can similarly write equation of motion for a two particle Green's function which will contain a three particle Green's function and so on. However, even the two particle Green's function is considerably difficult to compute numerically and it is desirable to limit our means of description of interacting electrons to one particle Green's function without any substantial loss of information.

It is obvious that one of the t_1 must be $t_1^+ = t_1 + \eta$ in the two-particle Green's

function in Eqn.(2.66), where η is an infinitesimal positive number. Therefore, we have $G_2\left(x_1, t_1, x_2, t_2, x_3, t_1, x_3, t_1^+\right)$ which gives two different possible time orderings and can be interpreted as:[36]

(1) $t_1 > t_2$: a particle propagates from (x_2, t_2) to (x_1, t_1) or (x_3, t_1^+) and a hole propagates from (x_1, t_1) or (x_3, t_1^+) to (x_3, t_1) and

(2) $t_1 < t_2$: two holes propagate from (x_1, t_1), (x_3, t_1) to (x_2, t_2), (x_3, t_1^+) or (x_3, t_1^+), (x_2, t_2)

Assuming the propagation of the two particles (or holes) to be independent of each other, which is the simplest approach at this stage to treat the interactions term, we can write:

$$G_2(x_1, t_1, x_2, t_2, x_3, t_1, x_3, t_1^+)$$

$$= \tag{2.67}$$

$$G(x_1, t_1, x_2, t_2)G(x_3, t_1, x_3, t_1^+) + G(x_1, t_1, x_3, t_1^+)G(x_3, t_1, x_2, t_2)$$

which upon substituting into Eqn.(2.64), leads to

$$\left[i\hbar\frac{\partial}{\partial t_1} - \hat{H}_0(x_1) - V_H(x_1, t_1)\right]G(x_1, t_1, x_2, t_2) + i\int v(x_1, x_3) \times$$
$$G(x_1, t_1, x_3, t_1^+)G(x_3, t_1, x_2, t_2)dx_3 = \hbar\delta(x_1 - x_2)\delta(t_1 - t_2) \tag{2.68}$$

where V_H can be derived from the first term of Eqn.(2.67) as:

$$V(x_1, t_1) = -i\int v(x_1, x_3)G(x_3, t_1, x_3, t_1^+)dx_3$$
$$= \int v(x_1, x_3)\langle N|\hat{\psi}^\dagger(x_3, t_1)\hat{\psi}(x_3, t_1)|N\rangle dx_3$$
$$= \int v(x_1, x_3)n(x_3, t_1)dx_3 \tag{2.69}$$
$$= V_H(x_1, t_1)$$

Reverting to the independent particle Green's function the second term can be understood as the exchange term of the Hartree-Fock equation which we know does not

involve self-interaction correction. It is therefore clear that the simple assumption of independent propagation is not capable of incorporating the dynamical correlation that we started of aiming at.

We will next aim to go beyond the independent propagation but as minimally possible to factor in self-interaction correction dynamically. Introducing an external field ϕ in the basic equation of motion (Eqn.(2.64)) as:

$$
\begin{aligned}
[i\hbar\frac{\partial}{\partial t} &- \hat{H}_0(x_1) - \phi(x_1, t_1)]G(x_1, t_1, x_2, t_2) \\
&+ i \int v(x_1, x_3)\langle N|\hat{T}[\hat{\psi}^\dagger(x_3, t_1)\hat{\psi}(x_3, t_1)\hat{\psi}(x_1, t_1)\hat{\psi}^\dagger(x_2, t_2)]|N\rangle dx_3 \\
&= \hbar\delta(x_1 - x_2)\delta(t_1 - t_2)
\end{aligned}
\tag{2.70}
$$

it is possible to derive an exact expression of the two particle Green's function as:

$$
\hbar\frac{\delta G(1, 2)}{\delta\phi(3)} = G_2(1, 2, 3, 3^+) - G(1, 2)G(3, 3^+)
\tag{2.71}
$$

using Gellmann-Low theorem[39] in the interaction representation. As obvious, we denote the labels "1,2,...,N" as "$(x_1, t_1),(x_2, t_2),...,(x_N, t_N)$".

Using the above expression of two particle Green's function in Eqn.(2.64), we obtain:

$$
[i\frac{\partial}{\partial t} - H_0(x_1) - V_H]G(1, 2) + i \int v(1, 3)\frac{\delta G(1, 2)}{\delta\phi(3)}d(3) = \delta(1 - 2)
\tag{2.72}
$$

Note that $\frac{\delta G(1,2)}{\delta\phi(3)}$ above is notional at this stage and we need to find way to calculate it which we defer to the next section.

Rather, at this point, instead of solving above equation as is we revert to Egn.(2.70), and we notionally introduce the "self-energy operator" which contain all the interaction terms in it as:

$$
[i\frac{\partial}{\partial t} - H_0(x_1) - V(1)]G(1, 2) - \int \Sigma(1, 2)G(3, 2)d(3) = \delta(1 - 2).
\tag{2.73}
$$

where $V(1) = \phi(1) + V_H(1)$.

Note that Σ is inherently non-local, dynamic and non-hermitian in nature.

Fourier transform of above equation yields an energy dependent self-energy operator as in:

$$[E - H_0(x_1) - V(x_1, E)]G(x_1, x_2, E) - \int \Sigma(x_1, x_3, E)G(x_3, x_2, E)dx_3 = \delta(x_1 - x_2)$$
(2.74)

Writing the above equation in matrix form:

$$(\tilde{E} - \tilde{H}_0 - \tilde{V})\tilde{G} - \tilde{\Sigma}\tilde{G} = 1 \tag{2.75}$$

$$\Rightarrow \tilde{G}^{-1} = (\tilde{E} - \tilde{H}_0 - \tilde{V} - \tilde{\Sigma}) \tag{2.76}$$

The non-interacting (i.e. without Σ) equation has a solution

$$\tilde{G_0}^{-1} = \tilde{E} - \tilde{H}_0 - \tilde{V} \tag{2.77}$$

therefore,

$$\tilde{G}^{-1} = \tilde{G_0}^{-1} - \tilde{\Sigma} \tag{2.78}$$

or

$$G = G_0 + G_0 \Sigma G \tag{2.79}$$

The poles of the Green's function G are shifted in energy by Σ from those of the non-interacting Green's function G_0. Thus, the self-energy may be considered as the correction to the total energy of the system. In the next section our task is to find way to construct Σ and calculate the self-energy correction.

2.4.5 Hedin's Equations and Approximations

This section contains the derivations of equations leading to construct of Σ following the two landmark papers published by Hedin in 1965 and 1969.[4,5] Comparing

equations (2.72) and (2.73), we get

$$\int \Sigma(1,3)G(3,2)d(3) = i\hbar \int v(1,3)\frac{\delta G(1,2)}{\delta \phi(3)}d(3) \qquad (2.80)$$

Noting $G^{-1}G = 1$ which lead to

$$\frac{\delta G}{\delta \phi} = -G\frac{\delta G^{-1}}{\delta \phi}G \qquad (2.81)$$

we find:

$$\Sigma(1,2) = -i\int v(1,3)G(1,4)\frac{\delta G^{-1}(4,2)}{\delta \phi(3)}d(3)d(4) \qquad (2.82)$$

consistent with Eqn.(2.73).

To interpret the Σ in terms of physically observable and measurable quantities we define few quantities.

Recalling:

$$
\begin{aligned}
V(x_1, t_1) &= \phi(x_1, t_1) - i\int v(x_1, x_2)G(x_2, t_1, x_2, t_1^+)dx_2 \\
&= \phi(x_1, t_1) + \int v(x_1, x_2)n(x_2, t_1)dx_2
\end{aligned} \qquad (2.83)
$$

dielectric response function can be obtained as:

$$\epsilon^{-1}(x_1, t_1, x_2, t_2) = \frac{\delta V(x_1, t_1)}{\delta \phi(x_2, t_2)} \qquad (2.84)$$

implying:

$$\epsilon^{-1}(1,2) = \delta(1-2) + \int v(1,3)\frac{\delta n(3)}{\delta \phi(2)}d(3) \qquad (2.85)$$

which can be written as:

$$\epsilon(1,2) = \delta(1-2) - \int v(1,3)P(3,2)d(3) \qquad (2.86)$$

where the polarization function is defined as

$$
\begin{aligned}
P(1,2) &= \frac{\delta n(1)}{\delta V(2)} \\
&= -i \int G(1,3)\Gamma(3,4,2)G(4,1^+)d(3)
\end{aligned}
\tag{2.87}
$$

where,

$$
\Gamma(1,2,3) = -\frac{\delta G^{-1}(1,2)}{\delta V(3)}
\tag{2.88}
$$

is known as vertex function.

With Γ defined above and the screened potential defined as:

$$
W(1,2) = \int \epsilon^{-1}(1,3)v(3,2)d(3)
\tag{2.89}
$$

we can rewrite the self-energy operator as:

$$
\Sigma(1,2) = i \int W(1,4)G(1,3)\Gamma(3,2,4)d(3)d(4).
\tag{2.90}
$$

In principle, we now have the complete recipe to calculate the self-energy operator which we summarize below

$$
\begin{aligned}
V(1) &= \phi(1) - i \int v(1,3)G(3,3^+)d(3) & (2.91)\\
\Gamma(1,2,3) &= -\frac{\delta G^{-1}(1,2)}{\delta V(3)} & (2.92)\\
P(1,2) &= -i \int G(1,3)\Gamma(3,4,2)G(4,1^+)d(3) & (2.93)\\
\epsilon(1,2) &= \delta(1-2) - \int v(1,3)P(3,2)d(3) & (2.94)\\
W(1,2) &= \int \epsilon^{-1}(1,3)v(3,2)d(3) & (2.95)\\
\Sigma(1,2) &= i \int W(1,4)G(1,3)\Gamma(3,2,4)d(3)d(4) & (2.96)
\end{aligned}
$$

These equations are known as Hedin's equations and are solved self-consistently.

However, in most cases it is sufficient to calculate the self-energy operator only up to
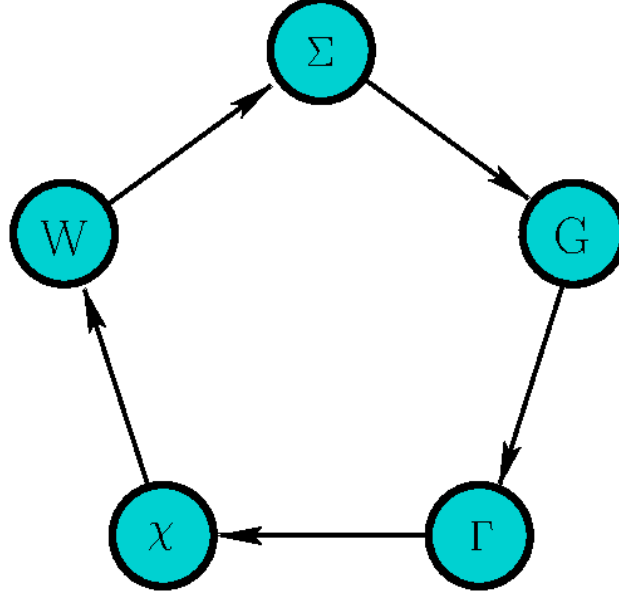
Figure 2.2: Flowchart for the iterative solution of the Hedin's equations.

the first iteration. As the first approximation, it is found reasonable to approximate the vertex function Γ as

$$\Gamma(1,2,3) = -\frac{\delta G^{-1}(1,2)}{\delta V(3)} \simeq \frac{\delta G_0^{-1}(1,2)}{\delta V(3)} = \delta(1-2)\delta(1-3) \qquad (2.97)$$

Using above approximation into expression of P, we get

$$P_0(1,2) = -iG_0(1,2)G_0(2,1^+) \qquad (2.98)$$

and the self-energy operator takes a simple form as

$$\Sigma(1,2) = iG_0(1,2)W(1,2) \qquad (2.99)$$

Fourier transform of all the Hedin's equations with the first approximation yields:

$$P_0(\mathbf{r}_1, \mathbf{r}_2, E) = -\frac{i}{2\pi} \int G_0(\mathbf{r}_1, \mathbf{r}_2, E - E') G_0(\mathbf{r}_1, \mathbf{r}_2, E') dE' \qquad (2.100)$$

$$\epsilon(\mathbf{r}_1, \mathbf{r}_2, E) = \delta(\mathbf{r}_1 - \mathbf{r}_2) - \int v(\mathbf{r}_1, \mathbf{r}_3) P_0(\mathbf{r}_3, \mathbf{r}_2, E) d\mathbf{r}_3 \qquad (2.101)$$

$$W(\mathbf{r}_1, \mathbf{r}_2, E) = \int \epsilon^{-1}(\mathbf{r}_1, \mathbf{r}_3, E) v(\mathbf{r}_3, \mathbf{r}_2) d\mathbf{r}_3 \qquad (2.102)$$

$$\Sigma(\mathbf{r}_1, \mathbf{r}_2, E) = \frac{i}{2\pi} \int G_0(\mathbf{r}_1, \mathbf{r}_2, E - E') W(\mathbf{r}_1, \mathbf{r}_2, E') dE' \qquad (2.103)$$

We now recall Eqn.(2.73) and write the corresponding homogeneous equation as:

$$\left(-\frac{1}{2} \nabla^2 + V_{ext} + V_H \right) \psi_{n\mathbf{k}}(\mathbf{r}) + \int \Sigma(\mathbf{r}, \mathbf{r}', E_{n\mathbf{k}}) \psi_{n\mathbf{k}}(\mathbf{r}') d\mathbf{r}' = E_{n\mathbf{k}} \psi_{n\mathbf{k}}(\mathbf{r}) \quad (2.104)$$

This is a Dyson equation for single-particle levels, upon solving we can obtain quasi-particle eigen functions and quasi-particle energies.

In the standard implementation of GW approximation it is assumed that the system is periodic in all directions and all the properties should therefore be invariant under translation with an arbitrary lattice vector $\mathbf{R}$. For a correlation functions like the dielectric function we can write: $\epsilon(\mathbf{r} + \mathbf{R}, \mathbf{r}' + \mathbf{R}; \omega) = \epsilon(\mathbf{r}, \mathbf{r}'; \omega)$ For extended systems it is easy to work in the reciprocal space. Therefore, the dielectric function takes the form in the the the reciprocal space

$$\epsilon_{\mathbf{G}\mathbf{G}'}(\mathbf{q}; \omega) = \delta_{\mathbf{G}\mathbf{G}'} - \sum_{\mathbf{G}_1} v_{\mathbf{G}\mathbf{G}_1}(\mathbf{q}) P_{\mathbf{G}_1\mathbf{G}'}(\mathbf{q}; \omega) \qquad (2.105)$$

where $\mathbf{q}$ is wave vector in the first Brillouin zone. In the usual 3D implementation the Coulomb potential in reciprocal space we can rewrite in Fourier space as:

$$v_{\mathbf{G}\mathbf{G}'}(\mathbf{q}) = \frac{4\pi \delta_{\mathbf{G}\mathbf{G}'}}{|\mathbf{q} + \mathbf{G}|^2} \qquad (2.106)$$

so that the sum over $\mathbf{G}$-vectors could have been left out in Eqn.(2.105). The screened interaction [Eqn.(2.102)] can be written in terms of the energy and wave-vector using

the Fourier transformation as:

$$W\left(\mathbf{r}, \mathbf{r}'; E\right) = \sum_{\mathbf{q}, \mathbf{G}, \mathbf{G}'} e^{i(\mathbf{q}+\mathbf{G})-\mathbf{r}} W_{\mathbf{G}\mathbf{G}'}(\mathbf{q}, \omega) e^{-i(\mathbf{q}+\mathbf{G}')-\mathbf{r}'} \qquad (2.107)$$

which after Fourier transformation takes the form:

$$W_{\mathbf{G}\mathbf{G}'}(\mathbf{q}, \omega) = v_{\mathbf{G}}(\mathbf{q})\epsilon_{\mathbf{G}\mathbf{G}'}^{-1}(\mathbf{q}, \omega) = \sqrt{v_{\mathbf{G}}(\mathbf{q})}\bar{\epsilon}_{\mathbf{G}\mathbf{G}'}^{-1}(\mathbf{q}, \omega)\sqrt{v_{\mathbf{G}'}(\mathbf{q})} \qquad (2.108)$$

An expression for the dielectric function can directly be found from Eqn.(2.105) which however depends on the irreducible polarizability $P_{\mathbf{G}\mathbf{G}'}(\mathbf{q}, \omega)$ matrix which in the G_0W_0 approximation is given within the random-phase approximation(RPA) by expression as given in Eqn.(2.98). Now with the help of the Lehmann representation we can obtain an expression for the irreducible polarizability in real space and frequency given by[40,41]

$$P\left(\mathbf{r}, \mathbf{r}'; \omega\right) = \sum_i \sum_j f_i \left(1 - f_j\right) \left[\frac{\psi_i(\mathbf{r})\psi_j^*(\mathbf{r})\psi_i^*\left(\mathbf{r}'\right)\psi_j\left(\mathbf{r}'\right) + c.c}{\omega + \varepsilon_i - \varepsilon_j} \right] \qquad (2.109)$$

where f_i is 0 if $\varepsilon_i > \mu$ and 1 if $\varepsilon_i < \mu$.

If we use DFT wave functions as an approximation for the quasiparticle wave functions the Green's functions are approximated by the DFT non-interacting Green's functions $G(12) \equiv G_0^{KS}(12)$ and the RPA irreducible polarization $P(12)$ turns out to be equivalent to the non-interacting polarizability $\chi^0(12)$. In terms of KS wave functions this takes the form

$$\chi^0\left(\mathbf{r}, \mathbf{r}'; \omega = 0\right) = \sum_{\mathbf{k},n} \sum_{\mathbf{k}',n'} f_{n\mathbf{k}} \left(1 - f_{n'\mathbf{k}'}\right) \left[\frac{\phi_{n\mathbf{k}}(\mathbf{r})\phi_{n'\mathbf{k}'}^*(\mathbf{r})\phi_{n\mathbf{k}}^*\left(\mathbf{r}'\right)\phi_{n'\mathbf{k}}'\left(\mathbf{r}'\right) + c.c}{\varepsilon_{n\mathbf{k}} - \varepsilon_{n'\mathbf{k}'}} \right]$$

$$(2.110)$$

where $f_{n\mathbf{k}}$ is the occupation number of the single-particle KS state $|n\mathbf{k}\rangle$. Fourier

transformation of above Eqn.(2.110) gives[6,40,41]

$$
\chi^0_{\mathbf{GG'}}(\mathbf{q}) = \frac{2}{V} \sum_{n,n',\mathbf{k}} \frac{f_{n,\mathbf{k}}\left(1 - f_{n',\mathbf{k}+\mathbf{q}}\right)}{\varepsilon_{n,\mathbf{k}} - \varepsilon_{n',\mathbf{k}+\mathbf{q}}} \times
$$
$$
\left[\left\langle n, \mathbf{k} \left| e^{-i(\mathbf{q}+\mathbf{G})\cdot\mathbf{r}} \right| n', \mathbf{k}+\mathbf{q} \right\rangle \left\langle n', \mathbf{k}+\mathbf{q} \left| e^{i(\mathbf{q}+\mathbf{G'})\cdot\mathbf{r'}} \right| n, \mathbf{k} \right\rangle + \mathbf{c} \cdot \mathbf{c}. \right] \tag{2.111}
$$

the factor 2 before the summation accounts for spin degeneracy and symbol V represents the volume of the cell.

Now the static dielectric matrix $\epsilon_{\mathbf{GG'}}(\mathbf{q}; \omega = 0)$ is calculated using Eqn.(2.111) in Eqn.(2.105) and then it extends to the finite frequencies with the help of generalized plasmon-pole (GPP) model proposed by the Hybertsen-Louie[6] where, the effective bare plasma frequency $\Omega_{\mathbf{GG'}}(\mathbf{q})$ is estimated (within the GPP model) as:

$$
\Omega^2_{\mathbf{GG'}}(\mathbf{q}) = \omega_p^2 \frac{(\mathbf{q}+\mathbf{G})\cdot(\mathbf{q}+\mathbf{G'})}{|\mathbf{q}+\mathbf{G}|^2} \frac{\rho(\mathbf{G}-\mathbf{G'})}{\rho(\mathbf{0})} \tag{2.112}
$$

where, ρ is the crystalline charge density.

We can expand the quasiparticle wave function in terms of the DFT wave functions

$$
\psi_{n\mathbf{k}}(\mathbf{r}) = \sum_{n'} \alpha_{nn'}(\mathbf{k}) \phi_{n'\mathbf{k}}(\mathbf{r}) \tag{2.113}
$$

in order to solve the quasi-particle eigenvalue equation(2.104). In above equation wave functions $\phi_{n\mathbf{k}}$ are obtained from solving the effective one-particle KS equations of DFT.

Now with help of sprectal weight functions A and B of Green's function and screened ineraction respectively, the real part of the self-energy operator splits into two terms screened-exchange(SEX) and Coulomb-hole(COH) for whcih a more detailed description is included in Chapter 7. The screened interaction can be expanded in plane waves and the dielectric function can be expressed by the GPP model then we can calculate the screened-exchange term and the Coulomb-hole

term of COHSEX seperately. The screened-exchange term is computed as:

$$
\begin{aligned}
\langle n\mathbf{k} \left| \Sigma_{\text{SEX}}\left(\mathbf{r}, \mathbf{r}'; E\right) \right| n'\mathbf{k} \rangle = &-\sum_{n_1}^{occ} \sum_{\mathbf{q}, \mathbf{G}, \mathbf{G}'} \langle n\mathbf{k} \left| e^{i(\mathbf{q}+\mathbf{G}|\cdot\mathbf{r}} \right| n_1, \mathbf{k} - \mathbf{q} \rangle \\
&\left\langle n_1, \mathbf{k} - \mathbf{q} \left| e^{-i(\mathbf{q}+\mathbf{G}')\cdot\mathbf{r}'} \right| n'\mathbf{k} \right\rangle \times \\
&\left[1 + \frac{\Omega^2_{\mathbf{GG}'}(\mathbf{q})}{\left(E - \varepsilon_{n_1\mathbf{k}-\mathbf{q}}\right)^2 - \widetilde{\omega}^2_{\mathbf{GG}'}(\mathbf{q})} \right] v\left(\mathbf{q} + \mathbf{G}'\right),
\end{aligned}
\tag{2.114}
$$

and the Coulomb-hole term is computed as:

$$
\begin{aligned}
\langle n\mathbf{k} \left| \Sigma_{\text{COH}}\left(\mathbf{r}, \mathbf{r}'; E\right) \right| n'\mathbf{k} \rangle = &\sum_{n_1} \sum_{\mathbf{q}, \mathbf{G}, \mathbf{G}'} \langle n\mathbf{k} \left| e^{i(\mathbf{q}+\mathbf{G})\cdot\mathbf{r}} \right| n_1, \mathbf{k} - \mathbf{q} \rangle \\
&\left\langle n_1, \mathbf{k} - \mathbf{q} \left| e^{-i(\mathbf{q}+\mathbf{G}')\cdot\mathbf{r}'} \right| n'\mathbf{k} \right\rangle \times \\
&\frac{1}{2} \frac{\Omega^2_{\mathbf{GG}'}(\mathbf{q})}{\widetilde{\omega}_{\mathbf{GG}'}(\mathbf{q}) \left[E - \varepsilon_{n_1\mathbf{k}-\mathbf{q}} - \widetilde{\omega}_{\mathbf{GG}'}(\mathbf{q})\right]} v\left(\mathbf{q} + \mathbf{G}'\right)
\end{aligned}
\tag{2.115}
$$

to which $\alpha_{nn'} \approx \delta_{nn'}$. We stop here the technical aspects of GW approximation but one can find a detail information of the implementation and evaluation of GW approximation in Ref..[6,41,42] Finally, assuming the quasi-particle wavefunctions are same as that of the Kohn-Sham orbitals, the quasi-particle energies can be calculated as:

$$
E^{QP}_{\vec{k},n} = E^{KS}_{\vec{k},n} + \langle \psi^{KS}_{\vec{k},n} \left| \Sigma - V^{KS}_{xc} \right| \psi^{KS}_{\vec{k},n} \rangle
\tag{2.116}
$$

GW is an accurate technique for computing correlated electronic structure of materials which inherently requires a faithful representation of excitation of each electron in response to perturbation due to motion of other electrons. However, in a typical *GW* implementation, the computational cost is $O(N^4)$, with each Green's function accounting for $O(N^2)$ for a system of size N, which is the number of states considered for their construction. For example in Fig.[2.3] reproduced from Ref.,[42] the computational cost in terms of wall time and required memory is ploted as a function of number of CPUs used for calculation of ϵ and Σ with 800 unoccupied bands in a 1x1x256 finner k-mesh for a unit cell of (20,20) single-walled carbon

nanotube of 80 carbon atoms implying 160 occupied bands.
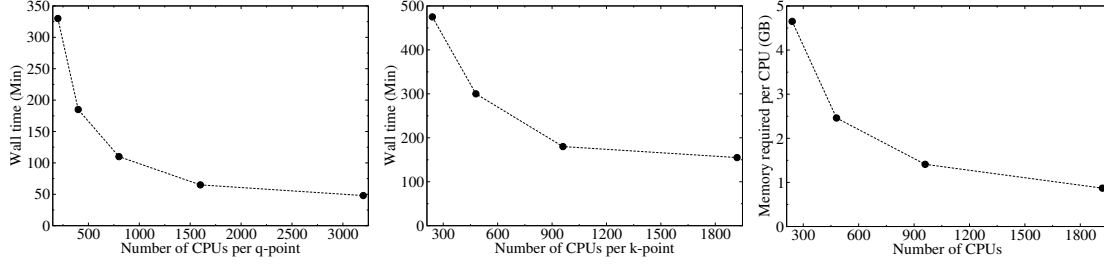
Figure 2.3: Computational cost of GW calculation of a (20,20) single-walled carbon nanotube. These data are taken from Ref.[42]

2.5 Electron in periodic potential: Tight-binding framework

In this section I will briefly introduce the Bloch formalism and the conceptual basis of Wannier function and the tight-binding framework based on it.

A periodic system is characterized by an effective periodic potential that a non-interacting electron in it is subjected to. Such a potential satisfies:

$$V(\mathbf{r}) = V(\mathbf{r} + \mathbf{R}), \tag{2.117}$$

where

$$\mathbf{R} = n_1\mathbf{a}_1 + n_2\mathbf{a}_2 + n_3\mathbf{a}_3 \tag{2.118}$$

is any real space lattice vector with $\{n_i\} \rightarrow \mathbb{Z}$, $\mathbf{a}_i$(i=1,2,3) being three primitive lattice vectors enclosing a finite volume which is defined as the primitive unit-cell which defines the periodicity of the system. For a given system, although the volume of the primitive unit-cell is uniquely defined, the primitive unit-cell itself is not.

The potential defines a non-interacting Hamiltonian which satisfies:

$$H(\mathbf{r}) = H(\mathbf{r} + \mathbf{R}), \tag{2.119}$$

Within the Born-von Karman(BVK) periodic boundary condition(PBC), which is central to the Bloch formalism that we resort in order to describe non-interacting electrons in such a periodic systems, the infinitely extended perfect crystal is divided into chunks of crystals containing, say, $N_1 \times N_2 \times N_3$ number of unit-cells which may or may not be primitive but rather a convenient choice. Analytic description, namely, the Bloch formalism, is derived for finite $\{N_i\}$, which are then notionally set to ∞ to represent a perfect crystal.

For such a chunk of crystal, wave functions describing non-interacting electrons within the BVK PBC satisfy:

$$\psi(\mathbf{r}) = \psi(\mathbf{r} + N_1\mathbf{a}_1 + N_2\mathbf{a}_2 + N_3\mathbf{a}_3). \tag{2.120}$$

which allows expansion in the Fourier basis $\{e^{i\mathbf{f}.\mathbf{r}}\}$ defined by wave-vectors:

$$\mathbf{f} = \sum_{i=1}^{3} \frac{m_i}{N_i}\mathbf{b}_i, \tag{2.121}$$

with $m_i \to \mathbb{Z}$ and $\mathbf{b}_i$(i=1,2,3) are primitive reciprocal lattice vectors which satisfy $\mathbf{b}_i.\mathbf{a}_j = 2\pi\delta_{ij}$.

However, such a solution to the periodic Hamiltonian defined in Eqn.(2.119) becomes possible if the Fourier coefficients $\{C_{\mathbf{f}}\}$ seperates out into $N_1 \times N_2 \times N_3$ linearly indipendent sets each idenified by a unique $\mathbf{f}$ defined by $\{m_i = 0, 1, 2, ..., N_i - 1\}_{i=1,2,3}$.

Denoting the unique set of wave-vectors $\{\mathbf{f}\}$ as $\{\mathbf{k}\}$, referred as the allowed values of crystal momentum, we therefore have for each unique $\mathbf{k}$:

$$\psi_{\mathbf{k}}(\mathbf{r}) = \frac{1}{\sqrt{\Omega}} \sum_{\mathbf{G}} C_{\mathbf{k}-\mathbf{G}} e^{i(\mathbf{k}-\mathbf{G}).\mathbf{r}} \tag{2.122}$$

where $\Omega = N_k\Omega_{cell}$, with $N_k = N_1N_2N_3$, and $\mathbf{k} = \sum_{i=1}^{3} \frac{m_i}{N_i}\mathbf{b}_i$ with $m_i = 0, 1, 2, ..., N_i - 1$ and $\mathbf{G} = l_1\mathbf{b}_1 + l_2\mathbf{b}_2 + l_3\mathbf{b}_3$ is a reciprocal lattice vector with $l_i \to \mathbb{Z}$

Eqn.(2.122) implies

$$\psi_{\mathbf{k}}(\mathbf{r}) = \frac{1}{\sqrt{N_k}} u_{\mathbf{k}}(\mathbf{r}) e^{i\mathbf{k}.\mathbf{r}}, \tag{2.123}$$

where $u_{\mathbf{k}}(\mathbf{r})$ has the same periodicity as the Hamiltonian, and obtained as:

$$u_{\mathbf{k}}(\mathbf{r}) = \frac{1}{\sqrt{\Omega_{cell}}} \sum_{\mathbf{G}} C_{\mathbf{k}-\mathbf{G}} e^{i-\mathbf{G}.\mathbf{r}}. \tag{2.124}$$

The cell periodic functions $u_{\mathbf{k}}(\mathbf{r})$ can be obtained as eigen function of the Bloch Hamiltonian:

$$H(\mathbf{k}) = -\frac{(\hat{\mathbf{p}} + \hbar\mathbf{k})^2}{2m_e} + V(\mathbf{r}). \tag{2.125}$$

The eigenvalues and eigenstates of $H(\mathbf{k})$ provides the description of energy levels and charge density of non-interacting electrons in a periodic potential. In the Kohn-Sham analogue to Bloch Hamiltonian $V = V_H + V_{XC} + V_{ext}$.

The cell periodic function and the Bloch functions satify the following orthoronmality conditions:

$$\int_{\Omega_{cell}} u_{n\mathbf{k}}^*(\mathbf{r}) u_{n'\mathbf{k}}(\mathbf{r}) d\mathbf{r} = \delta_{nn'} \tag{2.126}$$

$$\int_{\Omega} \psi_{n\mathbf{k}}^*(\mathbf{r}) u_{n'\mathbf{k}'}(\mathbf{r}) d\mathbf{r} = \delta_{nn'} \delta_{\mathbf{k}\mathbf{k}'} \tag{2.127}$$

Following Eqn.(2.122) we note that

$$\psi_{\mathbf{k}+\mathbf{G}'}(\mathbf{r}) = \psi_{\mathbf{k}}(\mathbf{r}) \tag{2.128}$$

This periodicity of Bloch function in the reciprocal space suggests that Bloch function must have a Fourier expansion in plane waves with wave-vectors in the reciprocal of the reciprocal lattice, that is, the lattice in real space, namely, $\{\mathbf{R}\}$. $\psi_{n\mathbf{k}}(\mathbf{r})$ can therefore be expanded in the basis of $\{e^{\mathbf{k}.\mathbf{R}}\}$ as:

$$\psi_{n\mathbf{k}}(\mathbf{r}) = \frac{1}{\sqrt{N_k}} \sum_{\mathbf{R}} e^{i\mathbf{k}.\mathbf{R}} W_n(\mathbf{r} - \mathbf{R}). \tag{2.129}$$

where $W_n(\mathbf{r} - \mathbf{R})$ are known as the Wannier functions[11,12] . The sum over $\mathbf{R}$ in Eqn.(2.129) goes over all the $N_1 \times N_2 \times N_3$ unit-cells. Notably, often it is also conversely stated that $\psi_{n\mathbf{k}}(\mathbf{r})$ is expanded in terms of the Wannier functions in Eqn.(2.129). Wannier functions can therefore be obtained inverse Fourier transform of $\psi_{n\mathbf{k}}(\mathbf{r})$ as:

$$W_n(\mathbf{r} - \mathbf{R}) = \frac{1}{\sqrt{N_k}} \sum_{\mathbf{k}} e^{-i\mathbf{k}.\mathbf{R}} \psi_{n\mathbf{k}}(\mathbf{r}). \tag{2.130}$$

or more generally:

$$W_n(\mathbf{r} - \mathbf{R}) = \frac{1}{\sqrt{N_k}} \sum_{\mathbf{k}} e^{-i\mathbf{k}.\mathbf{R}} \sum_{m} U_{nm} \psi_{m\mathbf{k}}(\mathbf{r}). \tag{2.131}$$

With proper choice of gauge $\underline{U}$, Wannier functions can be constructed to be localized within a desired unit-cell. Orthonormality condition satisfied by Wannier functions:

$$\langle W_n(\mathbf{r}, \mathbf{R}) \mid W_{n'}(\mathbf{r}, \mathbf{R}^{'}) \rangle = \delta_{nn'} \delta_{\mathbf{R}\mathbf{R}'} \tag{2.132}$$

Localized set of orthonormal Wannier functions thus constitute an ideal set of localized orthogonal basis.

2.5.1 Tight-Binding model

Tight-binding(TB) model is the simplest single particle approach for calculation of electronic structure of a system of atoms. A representation of a given Hamiltonian is constructed in the basis of a chosen set of N number of orthonormal localized functions $\{\phi_i(\mathbf{r})\}$. For isolated(periodic) systems the wave functions (Wannier functions) are considered as a linear combinations of the chosen basis functions.

$$W_n(\mathbf{r}, \mathbf{R}) = \sum_{m}^{N} C_{nm} \phi_m(\mathbf{r}, \mathbf{R}). \tag{2.133}$$

where $\mathbf{R}$ is a lattice vector spanning the entire crystal and $\{\phi_n(\mathbf{r}, \mathbf{R})\}$ are considered translated to the unit-cell defined by $\mathbf{R}$. For isolated systems only $\mathbf{R} = 0$ is

considered.

Depending on the range of the basis functions used, a TB model can be chosen to represent either only few bands about the Fermi energy, or a wide subspace of bands covering not only the entire occupied subspace but also an equal number of bands from the unoccupied subspace, as is the case in this thesis.

Traditionally, $\{\phi_i(\mathbf{r})\}$ are chosen to be atomic orbitals obtained as:

$$H_{at}\phi_j(\mathbf{r}) = E_j\phi_j(\mathbf{r}). \tag{2.134}$$

H_{at} being the atomic Hamiltonian and E_j being the energy levels of a single atom.

Referring to the Bloch functions introduced in the previous section, Schrödinger equation for the crystal can be written as,

$$H\psi_{m\mathbf{k}}(\mathbf{r}) = (\sum_{atom} H_{at} + \Delta V)\psi_{m\mathbf{k}}(\mathbf{r}) = \varepsilon_m(\mathbf{k})\psi_{m\mathbf{k}}(\mathbf{r}), \tag{2.135}$$

where, H is the crystal Hamiltonian and ΔV contains the corrections to reproduce the full periodic potential of the crystal in terms of the ionic potentials.

Taking inner product of both sides of Eq.2.135 with $\phi_n^*(\mathbf{r})$ at $\mathbf{R} = 0$:

$$\int \phi_n^*(\mathbf{r})(\sum_{atom} H_{at} + \Delta V)\psi_{m\mathbf{k}}(\mathbf{r})d^3r = \varepsilon_m(\mathbf{k})\int \phi_n^*(\mathbf{r})\psi_{m\mathbf{k}}(\mathbf{r})d^3r. \tag{2.136}$$

using Eqn.2.130 and (2.133):

$$\varepsilon_m(\mathbf{k})\sum_l C_{ml}\sum_{\mathbf{R}}\int d^3r\phi_n^*(\mathbf{r})\phi_l(\mathbf{r} - \mathbf{R})e^{i\mathbf{k}.\mathbf{R}} =$$

$$\sum_j C_{mj}\sum_{\mathbf{R}}\int d^3r\phi_n^*(\mathbf{r})(H_{at} + \Delta V)\phi_j(\mathbf{r} - \mathbf{R})e^{i\mathbf{k}.\mathbf{R}}$$

which simplifies to:

$$(\varepsilon_m(\mathbf{k}) - E_n)\sum_l C_{ml}\sum_{\mathbf{R}}\alpha_{nl}(\mathbf{R})e^{i\mathbf{k}.\mathbf{R}} = \sum_j C_{mj}\sum_{\mathbf{R}}\gamma_{nj}(\mathbf{R})e^{i\mathbf{k}.\mathbf{R}} \tag{2.137}$$

with

$$\alpha_{mn}(\mathbf{R}) = \int d^3r \ \phi_m^*(\mathbf{r})\phi_n(\mathbf{r} - \mathbf{R}) \tag{2.138}$$

$$\gamma_{mn}(\mathbf{R}) = -\int d^3r \ \phi_m^*(\mathbf{r})\Delta V \phi_n(\mathbf{r} - \mathbf{R}). \tag{2.139}$$

Notably, there will be N number of equations like (2.137) for $n = 1, 2, 3, ..., N$. Noting that $\alpha_{mn}(\mathbf{R} = 0) = \delta_{mn}$ we can rearrange (2.137) as a eigenvalue problem. $\alpha_{mn}(\mathbf{R} \neq 0)$ is the overlap of m-th and n-th atomic orbitals located at different unit-cells, and is often considered negligible. The most important parameter is $\gamma_{m,n}(\mathbf{R})$, is also known as 'hopping' parameter, which is often considered negligible beyond neighbouring unit-cells due to localized nature of the basis.

Chapter 3

Transferability of self-energy correction in localized orbital basis

In this chapter we first present a scheme for construction of atomic Wannier orbitals from first principles spanning a subspace of valence and conduction bands and calculations of tight-binding parameters in the basis of the constructed orbitals. The primary result of the chapter is the demonstration of transferability of self-energy correction in the atomic Wannier orbital basis. In this chapter we have only consider a single $2p_z$ orbital per atom.

3.1 Introduction

Designing new materials at nanoscale, typically consisting of few tens of atoms, necessitates increase in accuracy of estimation of electronic structure preferably without a commensurate increase in computational cost. Particularly with increasing spatio-temporal resolution of synthesis,[43] spectroscopic,[44] and transport[45] measurements of nanostructures, it has become imperative to match measured values to computed results in order to precisely determine atomic constitution of samples. Accordingly, computational methodologies have been evolved[46] over the years for estimation of electronic structure of systems typically with a few hundreds of elec-

trons, large enough to be within the experimentally accessible length-scales, primarily at the level of Kohn-Sham (KS) density-functional theory (DFT).[1,2] As a possible approach to compute self-energy corrected energetics of electrons in such large systems, in this work we demonstrate bottom-up transferability of self-energy correction when incorporated in a suitable tight-binding basis constituted from first principles.

Mean-field approximation of the Kohn-Sham ("KS") density-functional theory ("DFT"),[1,2] has established itself as a powerful tool for calculation of electronic structures of materials from first principles, to study ground state properties with reasonable accuracy, primarily in systems with weak localization of electrons in the valence sub-shells. Wannier functions,[11,47,48] constructed from KS single particle states, have been used as TB basis[49,50,51,52,53,54] to derive model Hamiltonians to focus only on the relevant group of orbitals. However, DFT being essentially a ground state theory, the inherent lack of discontinuity[55] of the derivative of the static and local[56] or semi-local[57] mean-field approximations of exchange-correlation functionals, upon addition or removal of electrons, leads to underestimation of band-gap compared to their experimentally measured values as the difference between the ionization potential ("IP") and electron affinity ("EA"). As a result, TB parameters computed from DFT often need further tuning parameters to match experimental data, such as band-gap, particularly in systems with increased correlation mainly due to localized electrons[58] Multitude of efforts to address these inadequacies have been pursued over last few decades, within and beyond the framework of DFT. Improvement of the exchange-correlation functionals either by correcting for derivative discontinuity explicitly[59,60] , or more popularly through incorporation of the inherently non-local nature of many-electron interactions by deriving non-local functionals[61] and partial inclusion of Hartree-Fock exact exchange in hybrid functionals[62,63] have been reasonably successful in addressing particularly the issue of underestimation of band-gap by DFT, with appropriate choice of relevant parameters.

A more general parameter free approach beyond the framework of DFT, is the many-body perturbation theory("MBPT")[64,65] wherein, many-electron effects are

treated as perturbation, resulting in description of interacting electrons as quasi-particles(QP) whose energies include corrections to the KS single-particle levels due to effective holes associated with electrons in lieu of their interaction with other electrons. These corrections, thereby known as self-energy ("SE") corrections("SEC"), computed up to the first order, have been shown[66] to be sufficient in accounting for the experimentally accessible SE corrected band-gap (IP-EA). However, since both the approaches - hybrid functionals and MBPT, are computationally expensive, MBPT being more so, scaling typically as N^4 with system size, it poses a formidable computational challenge to compute SE corrected band-gap till date even for nanostructures with dimensions in single digits of nanometers, using standard computational platforms. Notably though, considerable amount of effort and progress has been made in recent years in reducing the computational cost by using specialized basis sets.[67,68,69,70]

In this work our approach has been to first incorporate the SEC of KS single particle levels as corrections to TB parameters in a suitable basis and subsequently see if such corrections derived from a smaller reference systems can be reasonably applied to TB parameters derived for larger systems for realistic representation of SEC in such systems without needing to explicitly compute SEC for KS states which can be computationally prohibitively expensive with growing system size. Estimation of QP band-gap within a TB framework has been attempted in recent years,[71,72,73,74] largely based on tuning TB parameters to match the relevant QP structure. In the following we first discuss construction of the atomic orbital basis from the KS single-particle states, in which SEC is mapped, followed by brief description of the GW approximation of MBPT used in this work for calculation of SEC. We demonstrate our approach in graphene nano-ribbons(GNR), where GW approximation of SEC has been reported in details,[75] and also in hexagonal boron-nitride ribbons (hBNNR) as example of wide band-gap insulator.

3.2 Construction of atomic Wannier orbitals

The TB basis used in this work are orthonormal Wannier[11,47,48] orbitals constructed as linear combination of KS energy eigen-states with a specific choice of gauge that maximally retains their character as individual atomic orbtial. Since in this work we consider only $2p_z$ orbitals, we limit our discussion here on generation of one orbital per atom. We begin with a template consisting of one of the $2p$ orbitals each of B, C, N calculated using norm-conserving pseudo-potentials. The $2p$ orbital is chosen to be arbitrarily one of the lowest three degenerate set of KS states of an isolated B, C or N atom. The full system is then decorated with such orbitals to associate one single $2p_z$ orbital with each atom, aligned perpendicularly to the local plane defined by the nearest neighbourhood. These orbitals constitute a non-orthogonal set of localized basis from which a set of quasi-Bloch states are constructed as:

$$\tilde{\psi}_{\vec{k},j}(\vec{r}) = \frac{1}{\sqrt{N}} \sum_{\vec{R}} e^{i\vec{k}\cdot\vec{R}} \phi_{\vec{R},j}(\vec{r}), \tag{3.1}$$

where $\phi_{\vec{R},j}(\vec{r})$ is the j-th member of the non-orthogonal basis localized in the unit-cell denoted by the lattice vector $\vec{R}$ which spans over N unit-cells that define the periodicity of the Bloch states. Next we calculate the projection of the non-orthogonal quasi-Bloch states on the orthonormal Bloch states constructed from the cell-periodic KS-single particle states at all allowed $\vec{k}$, as:

$$O_{\vec{k},m,j} = \langle \psi_{\vec{k},m}^{KS} \mid \tilde{\psi}_{\vec{k},j} \rangle. \tag{3.2}$$

Subsequently the overlaps between the representation of the non-orthogonal quasi-Bloch states within the manifold of of the KS single-particle states, are calculated as:

$$S_{\vec{k},m,n} = \sum_{l} O_{\vec{k},m,l}^{*} O_{\vec{k},n,l}. \tag{3.3}$$

Finally, we use the Löwdin symmetric orthogonalization[76] scheme to construct a new set of orthonormal Bloch states from the KS single particle states as:

$$\Psi_{\vec{k},n}(\vec{r}) = \sum_m S_{\vec{k},m,n}^{-\frac{1}{2}} \sum_l O_{\vec{k},l,m} \psi_{\vec{k},l}^{KS}(\vec{r}), \tag{3.4}$$

using which, a set of localized orthonormal Wannier functions are constructed as:

$$\Phi_{\vec{R}',j}(\vec{r}) = \frac{1}{\sqrt{N}} \sum_{\vec{k}} e^{-i\vec{k}\cdot\vec{R}'} \Psi_{\vec{k},j}(\vec{r}). \tag{3.5}$$

Löwdin symmetric orthogonalization thus provides a choice of gauge for linear combination of KS states such that the resultant Wannier functions $\left\{\Phi_{\vec{R}',j}(\vec{r})\right\}$ would have minimal deviation from the non-orthogonal orbtials $\left\{\phi_{\vec{R},j}(\vec{r})\right\}$. Hence we here onwards refer these Wannier functions as atomic Wannier orbtials ("AWO"). TB parameters are computed in the AWO basis as:

$$t_{\vec{R}',\vec{R},i,j} = \langle \Phi_{\vec{R}',i} \mid H^{KS} \mid \Phi_{\vec{R},j} \rangle = \sum_{\vec{k}} e^{i\vec{k}\cdot(\vec{R}'-\vec{R})} \sum_l (OS^{-\frac{1}{2}})_{li}^* (OS^{-\frac{1}{2}})_{lj} E_{\vec{k},l}^{KS} \tag{3.6}$$

As obvious, the AWOs used here can in principle be substituted by any localized atomic orbitals constructed as linear combination of KS single particle states. To estimate self-energy("SE") correction("SEC") of the KS single particle levels we followed the GW approximation[6,41] of Hedin's formulation[4,5] of the many-body perturbation theory ("MBPT")[64,65] to describe single-particle excitations, wherein, many electron interactions are represented beyond mean-field by an energy dependent, non-local and non-Hermitian SE operator Σ, derived by considering the many-electron effects as perturbation treated within a self-consistent framework of Dyson's equation in terms of the one-particle non-local Green's functions G, as:

$$\Sigma(\vec{r},\vec{r}',E) = \frac{i}{2\pi} \int dE' e^{-i\delta E'} G(\vec{r},\vec{r}',E-E') W(\vec{r},\vec{r}',E') \tag{3.7}$$
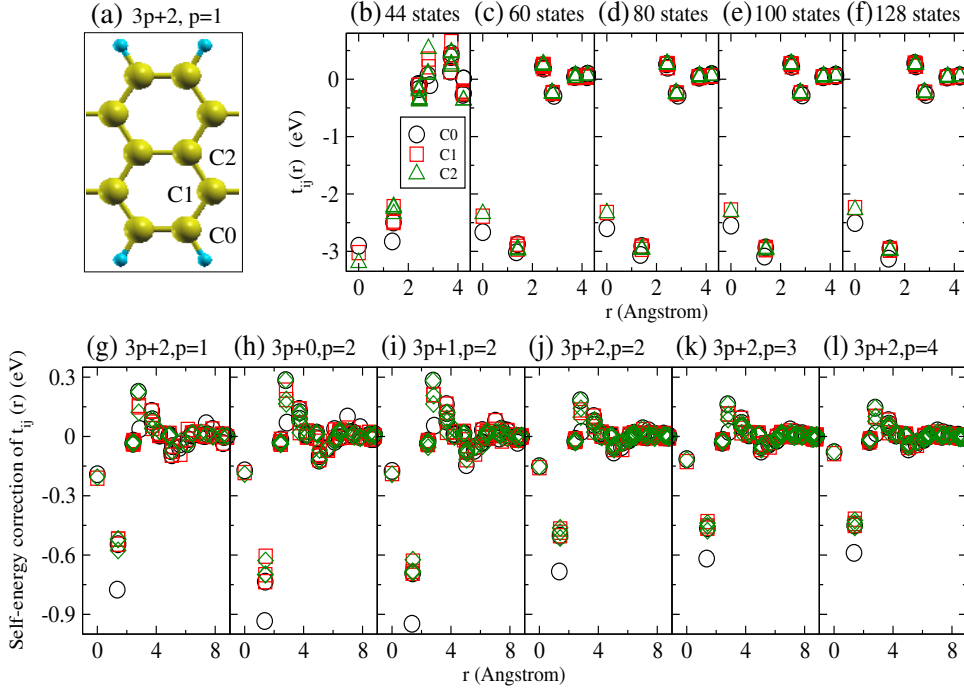
Figure 3.1: For the three inequivalent atoms marked in (a): (b-f): convergence of TB parameters $(t_{ij}(r))$ in terms of the number of KS bands considered for construction AWO($2p_z$); (g-l): self energy correction to TB parameters $(\Delta t_{ij}(r))$ in AGNRs of different families of increasing width.

where $\delta = 0^+$ and W is the Coulomb interaction screened by a non-local dynamic dielectric screening function computed approximately within the random phase approximation as extension of its static counterpart to finite frequencies following a generalized plasmon pole model.[6] With the underlying assumption that correction to the KS single particle states are negligible, the quasiparticle energies are approximated as:

$$E^{QP}_{\vec{k},n} = E^{KS}_{\vec{k},n} + \langle \psi^{KS}_{\vec{k},n} \mid \Sigma - V^{KS}_{xc} \mid \psi^{KS}_{\vec{k},n} \rangle \tag{3.8}$$

where V^{KS}_{xc} is the mean-field exchange-correlation potential derived from the exchange-correlation functionals used in DFT. Estimation of quasi-particle energies within GW approximation is computationally expensive primarily due to the slow convergence of ϵ^{-1} and G, and therefore of Σ, with respect to unoccupied single particle KS states. Substituting $E^{KS}_{\vec{k},n}$ in Eqn.(3.6) by quasiparticle energies $E^{QP}_{\vec{k},n}$ we calculate the SE corrected TB parameters $\left\{ t^{QP}_{\vec{R}',\vec{R},i,j} \right\}$. SEC of the TB parameters is thus
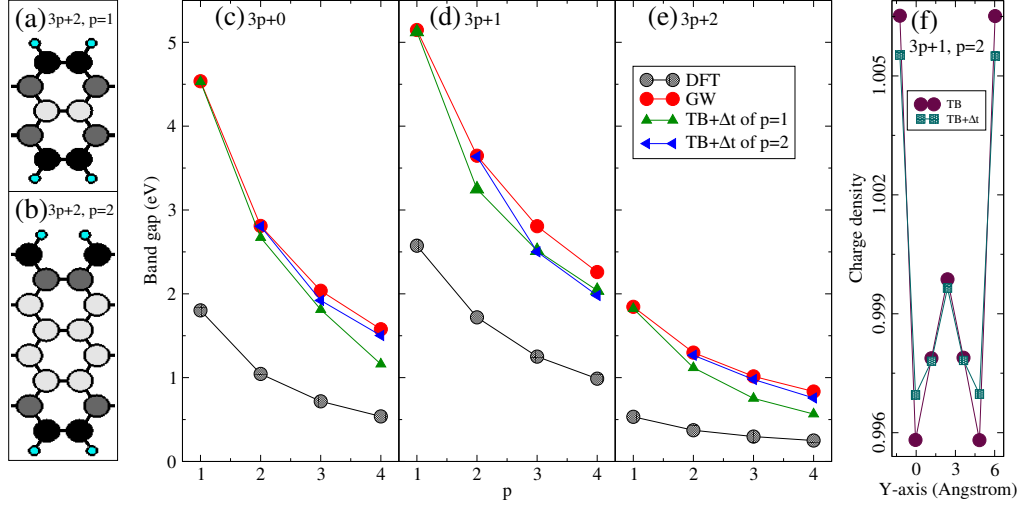
Figure 3.2: With transfer of (Δt) exemplified in (a) and (b): (b-d): comparison of band-gaps rendered by DFT,DFT+G_0W_0, and TB+Δt(of p=1 & 2) for three families of AGNRs with increasing width; (f) charge density from TB and TB+Δt.

estimated as:

$$\Delta t_{\vec{R}',\vec{R},i,j} = t^{QP}_{\vec{R}',\vec{R},i,j} - t^{KS}_{\vec{R}',\vec{R},i,j}, \tag{3.9}$$

3.3 Computational Details

There are two main steps in the proposed approach: (1) computation of the ground state electronic structure followed by construction of AWOs as per Eqn.(3.5) using the KS single particle states transformed as shown in Eqn.(3.4) followed further by calculation of TB parameters as per Eqn.(3.6), (2) calculation of SEC of KS single particle states using GW approximation and subsequent estimation of SEC of TB parameters [Δt] from QP energies.

Ground state electronic structures are calculated using a plane-wave based implementation of DFT.[77] Unit cells are structurally optimized with variable cell size using the BFGS scheme. Ground state energies are calculated using norm conserving pseudo-potentials with Perdew-Zunger (LDA) exchange-correlation[56] functional and plane wave energy cutoff of 60 Ry. Grid of $\vec{k}$-points 1x1x15 and 1x1x29 are used
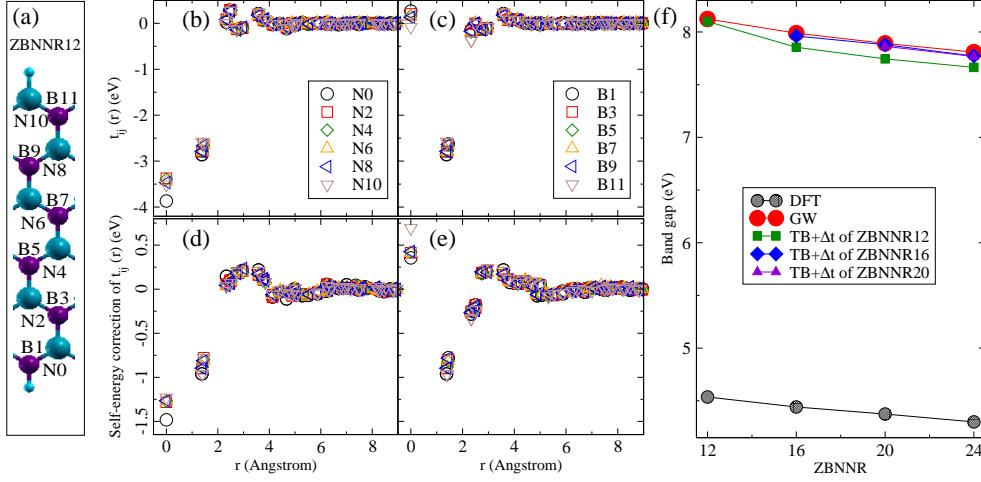
Figure 3.3: For the inequivalent atoms marked in (a): (b-c): TB parameters ($t_{ij}(r)$) in ZBNNR12; (d-e): corresponding self energy correction $\Delta t_{ij}(r)$; (f) comparison of band-gaps rendered by DFT,DFT+G_0W_0, and TB+Δt(of ZBNNR12) for wider ZBNNRs.

for AGNRs and ZGNRs respectively. Separation of more than 10 Angstrom is used between periodic images of nano-ribbons. We restricted to the non-self-consistent (G_0W_0) level for estimation of quasi-particle energies using the BerkeleyGW (BGW) implementation.[42] Parameters for calculation of SEC have been chosen as per Ref.-.[75] Band-gaps have been further converged with respects finer $\vec{k}$ grid through interpolation based on the AWOs. Construction of AWO, calculation of TB parameters in AWO basis, and estimation of SEC of TB parameters are performed using our implementation interfaced with the Quantun Espresso code.

3.4   Results and Discussion

In the following we primarily demonstrate our approach by accounting for SEC of KS band-gap in wider ribbons through correction to their TB band-gap calculated using SEC of TB parameters (Δt) obtained in a narrower ribbon. We chose AGNRs, ZGNRs and hBNNRs in order to span a wide range of band-gaps and magnetism with only $2p_z$ electrons.
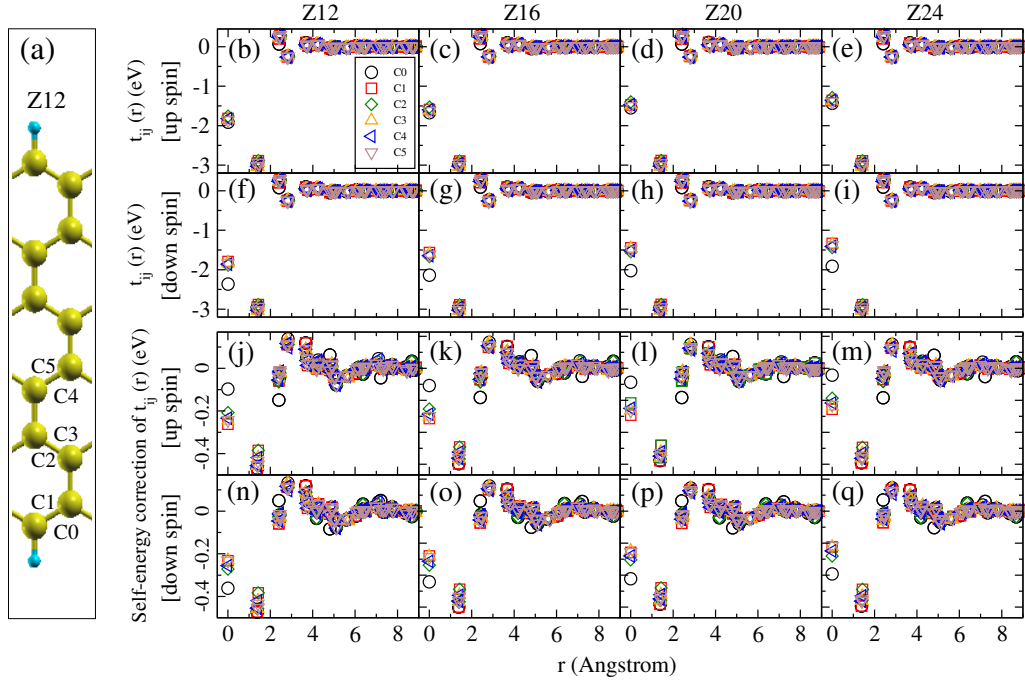
Figure 3.4: For the inequivalent atoms marked in (a) from edge towards bulk: TB parameters $(t_{ij}(r))$ for spin-1(a-e) and spin-2(f-i) in ZGNRs of increasing width; corresponding self energy corrections $\Delta t_{ij}(r)$ for spin-1(j-m) and spin-2(n-q).

3.4.1 Armchair Graphene Nanoribbons

We consider H-passivated AGNRs and ZGNRs of varying width wherein AGNRs are specified by a number of the dimer lines and ZGNRs by the number of zigzag chains. AGNRs are categorized in three different families as per the number(n) of dimer lines: $n = 3p + 0$, $n = 3p + 1$ and $n = 3p + 2$, p being an integer. In this work we consider only the $2p_z$ orbitals since they are well known to adequately describe the edge of the valence and conduction bands in GNRs. To maximize the $2p_z$ character of the corresponding AWOs, sufficient participation of the anti-bonding orbitals are required in order to match the weightage of bonding orbitals, which in GNRs are represented increasingly by bands closer to the conduction and valence band edges respectively. Fig.3.1(b-f) accordingly shows convergence of t_{ij} for all inequivalent atoms with respect to the total number of KS bands considered for construction of the AWOs. The fluctuation of hopping parameters from nearest to next-nearest and beyond, represent the favorable(unfavorable) nature of hopping

between dissimilar(similar) sub-lattices, as generic in bipartite systems. As per Fig.3.1(d), we consider on the average about extra 40 unoccupied states from the valence band for construction of AWOs.

Fig.3.1(g-l) shows SEC of TB parameters $\{\Delta t_{ij}\}$ for all the inequivalent atoms to their neighbours, for a representative set of AGNRs from all the three families, arranged in increasing order of width. Fig.3.1(g,j,k,l) suggests that correction to nearest neighbor(n-n) hopping reduced marginally after p=1 and convergence beyond p=2. However, Fig.3.1(g-i or h-j) indicates that corrections for 3p+1 and 3p+0 are lower than that of 3p+2 for same p, consistent with the fact that AGNRs with n=3p+2 are inherently metallic in nature with a small gap arising exclusively due to variation in TB parameters from the edge to the bulk due to relaxation of bond lengths. Notably, the n-n hopping term, which is between dissimilar sub-lattices, has the most significant negative correction implying consolidation of the n-n π-bond leading to enhanced localization of the π-bonding orbitals between atoms due to SEC. Positive correction of further hopping term between dissimilar sub-lattices also imply the same. Such localization all across the system, as implied by similar correction to hopping between nearest sites for all inequivalent atoms, would in effect result into withdrawal of charge from edge towards bulk, as evident Fig.3.1(f), due to consolidation of π bonds in the bulk. The resultant overall increase in uniformity of charge distribution effectively reduces mutual Couloumb repulsion between electrons of opposite spins, leading to lowering of the on-site term due to SEC. Consistent lowering of correction to the on-site term with increasing width indicates reduced levels of SEC in general with increasing value of p. Correction to the hopping between sites within the same sub-lattice, like the hopping between next nearest sites, is negligible since it is weak in the DFT level itself.

TB Band-gap with TB parameters in AWO basis derived from KS eigen-states of a given system, would match the KS band-gap of the same system by construction. Similarly, with SEC of TB parameters, referred here onwards as Δt, the correction to TB band-gap (SEC(TB)), would match the SEC of KS band-gap (SEC(KS)) of a given system, if Δt is obtained from SEC of KS single particle levels of the same sys-

tem, as evident in Fig.3.2(c-e) for p=1 and p=2. Motivated by the overall similarity in SEC of TB parameters within each families of AGNRs shown in Fig.3.1(g,j,k,l), we next test if SEC(KS) of a wider AGNR with p > 1 can be matched by SEC(TB) estimated with TB parameters calculated from KS states of the same system (p > 1), but using Δt obtained for p=1 ($\Delta t(p = 1)$) of the same family. As evident in Fig.3.2(c-e), within each family, using $\Delta t(p = 1)$ and $\Delta t(p = 2)$, it is possible to account for more than 80% of SEC(KS) in wider AGNRs ($p = 3, 4$), with no appreciable increase in computational cost beyond computation of TB parameters for wider ribbons. Owing to the convergence of Δt beyond p=2 [Fig.3.1(g,j,k,l)], the match between SEC(TB) and SEC(KS) is more accurate with $\Delta t(p = 2)$ than with $\Delta t(p = 1)$. The scheme for assignment of Δt from narrower to wider AGNRs is shown in Fig.3.2(a-b) where the atoms of matching colors are assigned same corrections. Correction data is collected for each single atom of the reference system for all its neighbouring pairs within a cutoff radius chosen to include typically up to 4th or 5th nearest neighbour beyond which the corrections are practically negligible. The transfer is done on the basis of two considerations: (1) matching atoms between the reference and the target systems in terms of their neighbourhood not limited to nearest neighbours, and (2) by maximally matching distance between pair of atoms in the reference system to that the target system. In mapping atoms for the criteria (1) the similarity of average nearest-neighbour bond-lengths around atoms can be used as a reasonable criteria.

3.4.2   hBN nanoribbons

Next we demonstrate the scheme in hBNNR, chosen as an example of wide band gap insulator where the SEC(KS) is substantial. The difference of electro-negativities of B and N are reflected in the difference in on-site terms in Fig.3.3(b,c). Δt plotted in Fig.3.3(d,e) show mild positive and strong negative SEC for on-site terms for B and N respectively, implying enhanced polarity of the B-N π-bond and consolidation of the lone pair of N. Noticeably, unlike in GNRs, Δt in all B and N atoms are very
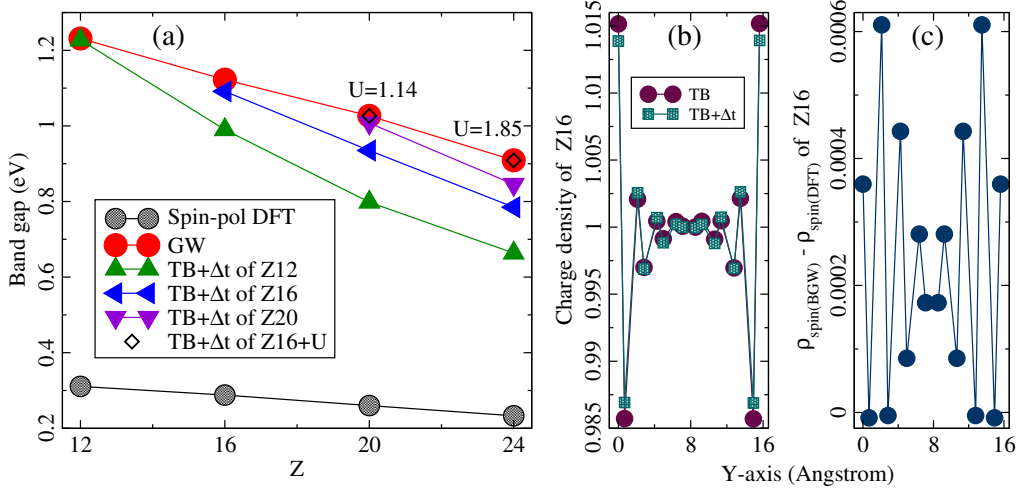
Figure 3.5: (a) Comparison of band-gaps rendered by DFT,DFT+G_0W_0, and TB+Δt(of Z12 & Z16) for ZGNRs of larger width (Z20,Z24); (b) charge density from TB and TB+Δt; (c) difference of absolute values of spin-densities($\rho_{spin} = n_\sigma - n_{\sigma'}$).

similar among their own kind irrespective of their proximity to edges, except the ones exactly at the edges. This is expected to enhance the degree of transferability of Δt across hBN ribbons systems. Fig.3.3(f) indeed suggests SEC(TB) to cover more than 90% of SEC(KS) in wider ZBNNRs with Δt calculated in the narrowest of the hBNNRs considered.

3.4.3 Zigzag edged graphene nano-ribbon

We next demonstrate the scheme in ZGNRs as an example of narrow band-gap magnetic materials where Coulomb correlation plays a central role in determining the electronic structure. The difference in on-site energies [Fig.3.4(b-i)] of the two spins at the zigzag edges, owes to spin separation between the two sub-lattices, which leads to localization of $2p_z$ electrons of opposite spins at the two edges characteristic of ZGNRs. Accordingly, although the C atoms in AGNRs and ZGNRs have the same local neighbourhood, their TB parameters and their SEC are expected to be fundamentally different since such spin-separation is completely absent in the former. Notably, for the C atoms at the ZGNR edges, the SEC of the on-site terms Fig.3.4(j-m) shows higher negative correction for the local majority spins, compared to those of the C atoms at the interior. This implies enhanced presence of $2p_z$
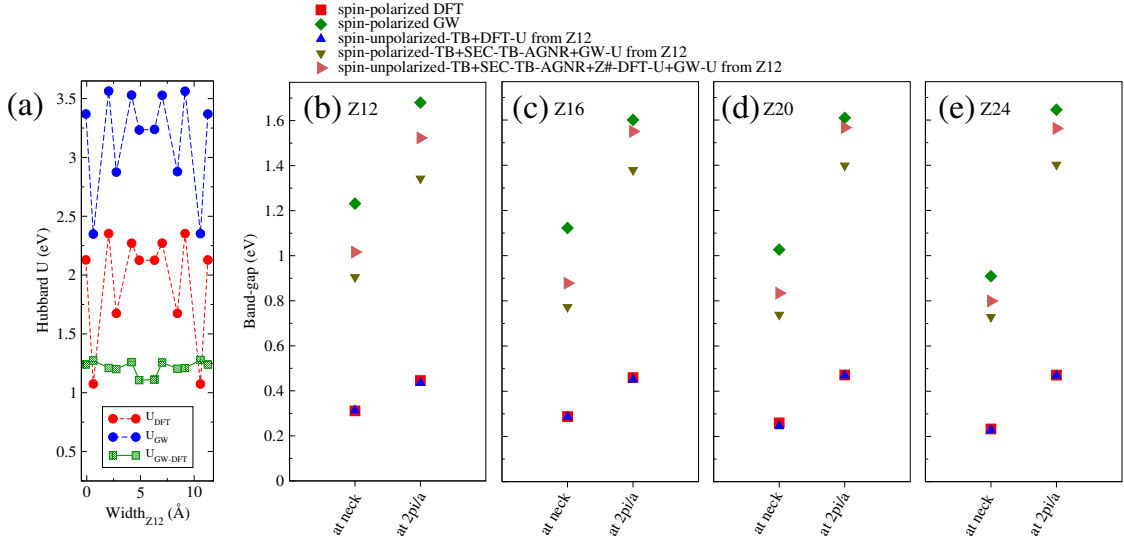
Figure 3.6: Band-gaps reproduction with the help of calculated Hubbard U of ZGNRs (a) DFT and G_0W_0 Hubbard U of Z12, (b), (c), (d) and (e) band-gaps reproduction of Z12, Z16, Z20 and Z24 respectively.

electron of one of the spins at an edge and removal of electron of the other spin from that edge, as a result of SEC. This enhancement in spin separation across the width of ZGNRs is evident in Fig.3.5(c), while Fig.3.5(b) implies withdrawal of charge from edge to bulk, as seen in AGNRs as well, due to SEC. Notably, while variation in n-n hopping itself [Fig.3.4(b-i)] is small among all inequivalent C atoms in each ZGNR and similar for all ZGNRs, the magnitude of Δt for n-n hopping reduces from Z12 to Z16 and converged thereafter[Fig.3.4(j-q)] for both spins. Accordingly, Fig.3.5(b) suggests a better accounting of SEC(KS) of wider ZGNRs(Z20,Z24) using Δt of Z16 than that using Δt of Z12.

Pertinently, transfer of charge from edge to bulk as seen in Fig.3.5(b), accompanied by enhancement of localization of opposite spins near the edges seen in Fig.3.5(c), is also observed within the Hubbard model with increasing strength of the on-site Coulomb repulsion U, although it is clear from the contribution of off-diagonal terms of Δt in reproducing SEC(KS), that DFT+U alone will not be sufficient to account for SEC. However, unlike AGNRs, ZGNRs being magnetic systems, it is reasonable to anticipate that SEC of KS single particle states will also have impact on the on-site Coulomb repulsion term U in addition to TB parameters.
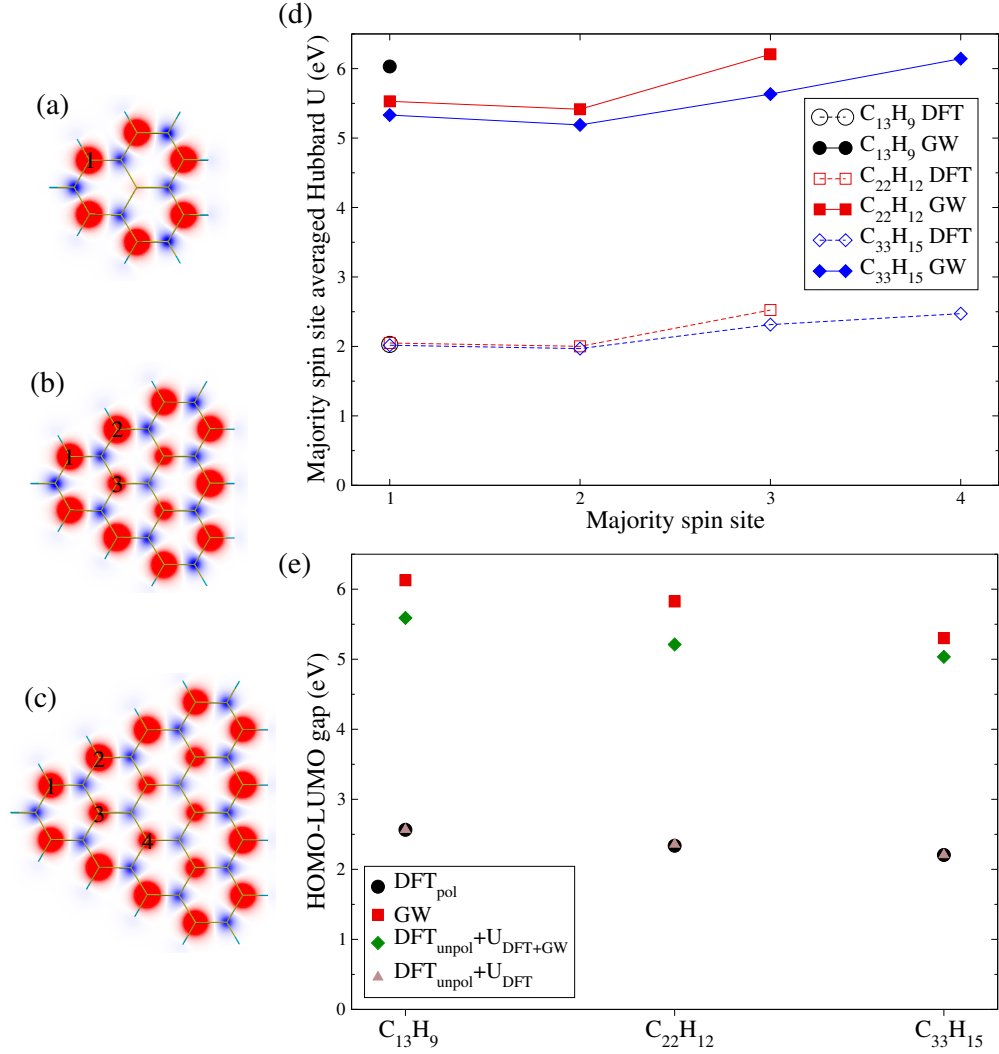
Figure 3.7: Spin density of (a) $C_{13}H_9$; (b) $C_{22}H_{12}$; (c) $C_{33}H_{15}$. (d) Calculated Hubbard U DFT as well as G_0W_0 and (e) HOMO-LUMO gap reproduction using Hubbard U.

Therefore while substituting Δt of wider ZGNRs by that of Z12 or Z16, we need to account for a possible underestimation of U. We therefore take recourse to the mean field approximation of the Hubbard model and self-consistently introduce ΔU along with Δt, as

$$H = \sum_{i,j,\sigma}(t_{ij} + \Delta t_{ij})c_{i\sigma}^{\dagger}c_{j\sigma} + \sum_{i,\sigma}\Delta U n_{i\sigma}\langle n_{i\sigma'}\rangle, \qquad (3.10)$$

where $\{t_{ij}\}$ are computed from KS eigen-states of the wider ZGNRs(Z20,Z24), and $\{\Delta t_{ij}\}$ from Z16. ΔU is tuned to match SEC(TB) to SEC(KS) in Z20 and Z24. As evident in Fig.3.5(a), indeed with application of a small U in addition to the

$\Delta t(Z16)$, it is possible to match the SE corrected KS band-gap of the wider ribbons with modest increase in spin density near the edges, implying enhanced inter-sublattice spin separation due to SEC, which is already hinted in Fig.3.5(c) which is with U=0. Indeed the ground state charge density does not change due the self-energy corrections within the diagonal approximation of GW. However, when we use the self-energy corrected hopping parameters within the mean field Hubbard model(MFHM) with an appropriate U needed to match the band-gap, we see the reported change in the charge density which appears to transfer charge from edge towards bulk, leading to marginal reduction in the inhomogeneity of charge distribution. We can possibly attribute it to the near uniform strengthening of the hopping parameter across the width of the ribbons due to self-energy correction, which should thus reduce the degree of relative variation of hopping parameters from bulk to edge, besides undermining the impact of Coulomb correlation.

3.4.4 Self-energy corrected Hubbard U

As mentioned above that ZGNRs are magnetic in nature and to reproduce the band-gaps for such systems accurately we additionally need Hubbard U along with the SEC-TB paramters which can be seen in Fig.3.5(a). Therefore, We exemplify and calculate the Hubbard U for magnetic ZGNR systems and also for hydrogen passivated finite graphene segments. We consider segments with unequal sub-lattice coverage, which is essential to have net magnetic moment given the bipartite nature of graphene. Hubbard U is calculated for both KS and GW levels within the mean-field approximation of Hubbard model[78] using the formula

$$U_i = \frac{E_{i\sigma} - E_{i\sigma'}}{n_{i\sigma} - n_{i\sigma'}} \tag{3.11}$$

where, i is the site index, σ's are the spins, E is the onsite energy and n is the spin density. We calculated the Hubbard U for ZGNRs as shown for Z12 nano-ribbon in Fig.3.6(a), where red and blue plots represent the DFT and GW Hubbard U

respectively for each site across the witdh of the ribbon and green plot represents difference of them (GW-DFT).

Applying the calculated Hubbard U of Z12 in Eqn.3.10 we tried to reproduce the band-gaps of all the ZGNRs. Band-gaps as well as the gaps at Brillouin zone edge are shown in Fig.3.6(b-e). Spin polarized DFT band-gaps are expectedly reproduced using the DFT Hubbard U with the spin un-polarized TB parameters. Next we used the GW Hubbard U of Z12 and spin polarized DFT-TB parameters along with the self-energy correction Δt of TB parameters taken from AGNR $3p + 1$ family with $p = 3$ to reproduce the GW band-gaps of ZGNRs, as shown by down triangle of each plots in Fig.3.6(b-e). We can see from the plots that the band-gaps are underestimated by a margin of 40% . Next we tried to reproduce the band-gaps with spin un-polarized TB parameters and DFT Hubbard U of the respective ZGNR along with the GW Hubbard U of Z12 and the SEC-TB parameters of the mentioned AGNR system. Reproduced band-gaps are shown by right triangle for each ZGNR in Fig.3.6(b-e). We can clearly see the improvement of band-gaps matching and particularly as we go from narrower to wider ZNGRs. We note that if we reproduce the band-gaps with only with Hubbard U then we need a higher U value which will thus not represent the correct scenario.

Next we consider three finite graphene chunks as described above. Spin densities along with the unit cells of all the three systems $C_{13}H_9$, (b) $C_{22}H_{12}$ and (c) $C_{33}H_{15}$ are shown in Fig.3.7(a-c) respectively. To calculate the Hubbard U we only consider the inequivalent majority spin sites as shown in Fig.3.7(a-c) with red color. $C_{13}H_9$ has two inequivalent majority spin site but the intensity of the majority spin is weak at the interior site which is hence not considered. $C_{22}H_{12}$ and $C_{33}H_{15}$ have three and four majority spin sites respectively, which are are marked as $1, 2, ..$ in Fig.3.7(a-c) for each systems. We calculated the DFT and GW Hubbard U for inequivalent majority spin sites using Eqn.(3.11) and then took the average within each set of inequivalent sites, as shown in Fig.3.7(d). We see that the DFT Hubbard U's are almost same for similar inequivalent site of all the systems but deviate substantially at the GW level. Next we first reproduced the HOMO-LUMO gaps for spin polarized DFT from spin

un-polarized TB parameters with DFT Hubbard U, and then reproduced HOMO-LUMO gaps in GW level using spin un-polarized TB parameters with combined DFT and GW Hubbard U, as shown in Fig.3.7(e). We also see here same trend of better matching of HOMO-LUMO gaps as systems size increases like we saw in case of ZGNRs. The range of values of the GW corrected Hubbard U stresses the need of correlation corrected computational frameworks beyond mean-field for estimation of electronic structures of the finite magnetics system even with p electrons.

3.5   Conclusions

In conclusion, we have presented a computationally inexpensive scheme for estimation of self-energy correction(SEC) of band-gap within a tight-binding(TB) framework in the basis of atomic Wannier orbitals (AWO) constructed from KS energy eigen-states. Within the scheme, SEC of TB parameters are first computed for a smaller reference system from SEC of KS single particle levels estimated using the GW approximation of MBPT, and then applied to TB parameters derived for a larger system of similar morphology, in order to estimate SEC of KS band-gap of the larger system, without needing to explicitly compute it. The efficacy of the approach, demonstrated in semiconducting and insulating as well as magnetic and non-magnetic nano-ribbons of graphene and hexagonal boron-nitride, is found to account for about 90% or more of the SE corrected band-gap for 50% to 100% increase in system size as assessed in this work, with nominal increase in computational cost. Notably, the degree of agreement[Fig.(3.2)(c-e),Fig.(3.3)(f)] between band-gaps estimated with mapped SEC in TB basis, and those directly computed (DFT+G_0W_0), clearly suggests that the scope of transferability should easily cover further increase in system size compared to that of the reference systems, particularly with increasing band gap, whereas, the only major computation beyond DFT for the larger systems in our approach is the computation of overlap matrices required for Löwding symmetrization and calculation of TB parameters, which should scale as $\mathcal{O}(N^2)$, compared to overall $\mathcal{O}(N^4)$ scaling of GW approximation. In gen-

eral, the SEC corrected TB framework opens the scope for in-depth analysis of SEC without having to explicitly generate SE corrected KS states. The results presented here pave the way for building up a repository of self-energy corrected TB parameters of different atoms at different chemical environment for their seamless use in estimation of SEC within a multi-orbital TB framework. The high values the GW corrected Hubbard U found in the magnetic graphene segments point to the need of strongly correlated description of electronic structures of such systems even though it is the p electrons which drive magnetism in such systems.

Chapter 4

Hybrid atomic orbital basis from first principles: Bottom-up mapping of self-energy correction to large covalent systems

In this chapter the key outcome is a numerical scheme to construct hybrid atomic Wannier orbital basis from first principles which are naturally oriented towards direction of coordination, and strategies to transfer of tight-binding parameters calculated in basis of the constructed orbitals in reference systems to larger isomorphic target systems through mapping of neighborhoods and projected Wannier charge centres. The proposed Wannier orbitals constitute a directed multi-orbital orthonormal basis which is demonstrated here to be promising of facilitating transfer of self-energy correction from smaller covalent systems to their larger variants with thousands of atoms.

4.0.1 Introduction

Setting a minimal TB basis for a given systems of atoms calls for appropriate orientation of orbitals at each atomic site in accordance with their immediate atomic neighbourhood, so that the nearest neighbour interactions can be represented by the least number of orbitals. In this direction, hybrid atomic orbitals have been used by quantum chemists since their introduction[79,80] almost a century ago. Rational approaches for their construction[9,81,82,83,84] over the last several decades have been primarily focussed on partitioning systems into substructures which are spanned by groups of hybrid orbitals, leading to unambiguous partitioning of electrons into bonding orbitals and lone-pairs, and further into atomic orbitals. For such partitioning, notionally similar several approaches[9,83,85,86,87,88] have been proposed grossly based on the maximum overlap condition which in effect leads to localization of orbitals within the chosen subspace of molecular orbitals. In these approaches, either the overlap matrix[9,83] or the first-order density matrices,[87,89] both of which are calculated typically in the basis of either the Slater type orbitals(STO)[90] or the Gaussian type orbitals(GTO),[91,92] are generally transformed into block diagonal forms each spanned by orbitals centered on nearest neighbour atoms. The resultant hybrid orbitals involving atomic orbitals centred on more than one atoms[84,93] render unambiguous bonding orbitals and bond-orders, while the ones like the *natural hybrid orbitals*(NHO)[89] or the *effective atomic orbital*(EAO),[88] which involve atomic orbitals of a single atom, describe the state of the orbitals of the atoms as they participate in bonds. Hybird orbitals in the line of NHOs have been popularly constructed ab-initio at the HF level.[94,95]

A more explicit approach[96,97] has been to construct the *generalized hybrid orbitals*(GHO) as combinations of STO with common Slater exponent and fixed position of nodes along bonds to assign their orientation. Expedient to clarify that in this paper we refer to bonds simply as the linear connectivity between atoms which are primarily nearest neighbours if not mentioned specifically. Much of these efforts were undertaken in aid to molecular mechanics calculation[98,99] where the description

of interactions between sub-structures eases with use of orbitals which are directed along bonds. Effective analytical models for such interactions have also been developed[100] recently for inexpensive deductive computation of properties of bulk as well as clusters of sp^x hybridized covalent systems. Notably unlike the GHOs, the NHOs or the EAOs by construction may not be oriented exactly along the bonds. In general for all such hybrid orbitals, their directed nature, maximal localization and orthonormality are not guaranteed simultaneously by construction. In a part of this work we explore simultaneity of these conditions in construction of hybrid atomic orbitals from first-principles proposed in this work.

Instead of overlap or density matrices, in this work we take recourse to the first moment matrices (FMM) due to their direct correspondence to localization. FMMs are known not to commute among each other in more than one dimension if projected on to a finite subspace of orthonormal states. We propose construction of hybrid atomic orbitals(HAO) as approximate eigen states of the FMMs within a finite subspace of Kohn-Sham (KS) states of isolated atoms. Orientation and hybridization of the proposed orbitals can be a-priori naturalized as per their anticipated neighbourhood. This substantially eases the effort of orientating them appropriately while transferring them from isolated atoms to the real systems, which eventually eases the interpretation of elements of the Hamiltonian. An orthonormal set of localized Wannier orbitals resembling the HAOs is further constructed in the basis of KS single particle states of the given system. These Wannier orbitals, which we refer in this paper as the *hybrid atomic Wannier orbitals* (HAWO), constitute a multi-orbital tight-binding (TB) basis locked to their immediate atomic neighbourhood by construction, and render hopping parameters involving effectively only two orbitals per bond. HAWOs thus offer easy transfer of the corresponding TB parameters to other iso-structural systems exclusively through mapping of neighbourhoods and projection of charge centres learned from HAOs. Effective transfer of TB parameters is demonstrated in nano-ribbons of graphene and hexagonal boron-nitride, C_{60}, and nano-diamonds and their silicon based counterparts. In particular, we show in the HAWO basis that it is possible to effectively transfer self-energy(SE) correc-

66

Hybrid atomic orbital basis from first principles: Bottom-up mapping of self-energy correction to large covalent systems

tion(SEC) of single particle levels from smaller reference systems to much larger iso-structural systems through TB parameters with minimal additional computational expense through the proposed mapping of multi-orbital TB parameters beyond the nearest neighbourhood.

4.1 Methodological details

4.1.1 Construction of hybrid orbitals

In a given direction, for example along $\hat{x}$, the most localized orbtials $\{\phi\}$ would diagonalize the corresponding FMM:

$$X_{ij} = \langle \phi_i \mid x \mid \phi_j \rangle. \tag{4.1}$$

This becomes clear by noting that the total spread of a finite set of N number of orbitals along $\hat{x}$ is given by:

$$\Omega_x = \sum_{i=1,N} \left[\langle \phi_i | x^2 | \phi_i \rangle - |\langle \phi_i | x | \phi_i \rangle|^2 \right], \tag{4.2}$$

which can be expressed as:

$$
\begin{aligned}
\Omega_x &= \sum_{i=1,N} \left(\sum_{j=1}^{\infty} X_{ij} X_{ji} - X_{ii} X_{ii} \right) \\
&= \sum_{i=1,N} \sum_{j \neq i}^{\infty} |X_{ij}|^2 \\
&= \sum_{i=1,N} \left(\sum_{j \neq i}^{N} |X_{ij}|^2 + \sum_{j=N+1}^{\infty} |X_{ij}|^2 \right).
\end{aligned} \tag{4.3}
$$

Diagonalization of X in the $N \times N$ subspace would therefore sets the first term in Eqn.(4.3) to zero, leading to minimization of total spread. Notably, X can be calculated directly as in Eqn.(4.1) only for isolated systems well separated from

their periodic images. For periodic system with non-zero crystal momentum, computation of X would essentially involve evaluation of geometric phases[101] of Bloch electrons evolved across the Brillouin Zone.[102,103] Nevertheless, there exists therefore a unique set of orbitals which completely diagonalize X, and would also thereby have maximum localization along $\hat{x}$. Similar unique sets exist for $\hat{y}$ and $\hat{z}$ directions as well. However, the matrices X, Y and Z, when projected into a finite subspace of orthonormal states, do not commute with each other in general unless mandated by symmetries. This implies that a unique set of orbitals with maximum localization simultaneously in all three orthogonal directions would not exist in general. The same is true for Wannier functions (WF) in case of periodic systems with non-zero wave-vectors. Numerically localized Wannier functions[47,104] therefore are not be unique and the choice of gauge used for their construction depends on the chosen criteria of localization.

We chose to look for the possibility to construct a set of localized orbitals which will be a reasonable compromise between the three unique sets of orbitals having maximum localization along the three orthogonal directions. We thus resorted to the condition of simultaneous approximate joint diagonalization[105] of the three FMMs: X, Y and Z. To compute such an approximate eigen sub-space of the three FMMs, we adopted an iterative scheme based on generalization of the Jacobi method of matrix diagonalization,[106] wherein, off-diagonal elements are iteratively minimized by applying rotation of coordinates by an optimally chosen angle. The extension of the method to more than one square matrices irrespective of whether they are commuting or not, is based on a proposed[105] choice of angle of rotation leading to complex rotation matrix U which has been proven[105] to minimize the composite objective function defined as :

$$\text{off}(UXU^\dagger) + \text{off}(UYU^\dagger) + \text{off}(UZU^\dagger) \tag{4.4}$$

where $\text{off}(A) = \sum_{1 \leq i \neq j \geq N} |A_{ij}|^2$ for an $N \times N$ matrix A. N being the number of orthonormal states used to compute X, Y and Z. U is a product of all the

$N(N-1)/2$ complex plane rotations, one each for each pairs of (ij) for $i \neq j$. For a given (ij) the plane rotation $R(i,j)$ is an $N \times N$ identity matrix except for:

$$\begin{pmatrix} r_{ii} & r_{ij} \\ r_{ji} & r_{jj} \end{pmatrix} = \begin{pmatrix} c & \bar{s} \\ -s & \bar{c} \end{pmatrix} \tag{4.5}$$

where $c, s \in C, |c|^2 + |s|^2 = 1$.

It has been shown[105] that the objective function defined in Eqn.(4.4) is minimized if U is a product of $R(i,j)$ matrices as shown in Eqn.(4.5) whose elements are given as:

$$c = \sqrt{\frac{x+r}{2r}}; s = \frac{y - iz}{\sqrt{2r(x+r)}} \tag{4.6}$$

where

$$r = \sqrt{x^2 + y^2 + z^2}$$

and $[x, y, z]^\dagger$ being the eigen-vector corresponding to the highest eigen-value of a 3×3 matrix:

$$
\begin{aligned}
G(i,j) = \quad & \text{Real}\left(h^\dagger(X, i, j) h(X, i, j) \right) \\
+ \quad & \text{Real}\left(h^\dagger(Y, i, j) h(Y, i, j) \right) \\
+ \quad & \text{Real}\left(h^\dagger(Z, i, j) h(Z, i, j) \right)
\end{aligned}
$$

with:

$$h(A, i, j) = [a_{ii} - a_{jj}, a_{ij} + a_{ji}, i(a_{ji} - a_{ij})]. \tag{4.7}$$

Notably, given the form of $R(i,j)$, for a rotated matrix $A' = R(i,j)AR^\dagger(i,j)$ corresponding to plane rotation for the (ij)-th pair of elements of A, it is easily seen that $a'_{kk} = a_{kk}$ for $k \neq i$ and $k \neq j$, leading to the invariance:

$$\text{off}(A') + |a'_{ii}|^2 + |a'_{jj}|^2 = \text{off}(A) + |a_{ii}|^2 + |a_{jj}|^2.$$

owing to preservation of norm in similarity transformation. Therefore, minimiz-

ing off(A') would naturally imply maximising $|a'_{ii}|^2 + |a'_{jj}|^2$, which further implies maximising $|a'_{ii} - a'_{jj}|^2$ since:

$$2\left(|a'_{ii}|^2 + |a'_{jj}|^2\right) = |a'_{ii} + a'_{jj}|^2 + |a'_{ii} - a'_{jj}|^2 \tag{4.8}$$

and

$$a'_{ii} + a'_{jj} = a_{ii} + a_{jj} \tag{4.9}$$

owing to invariance of trace under similarity transformation. Therefore in our case the minimization of the objective function[Eqn.(4.4)] implies maximizing the separation between the charge centres of the i-th and the j-th orbitals, which is thus similar to the principle of the Foster and Boys[107] scheme of orbital localization. This becomes clear by rewriting the total spread [Eqn.(4.3)] for N orbital $\{\phi_i, i = 1, N\}$ as:

$$\Omega = \sum_{k=1,3} \sum_{i=1,N} \left(\sum_{\substack{j=1 \\ j\neq i}}^{N} |a_{ij}^k|^2 + \sum_{j=N+1}^{\infty} |a_{ij}^k|^2 \right) \tag{4.10}$$

where $A^{k=1,2,3} = X, Y, Z$. Eqn.(4.10) clearly suggests that minimization of the objective function in Eqn.(4.4) would minimizes the first term in Eqn.(4.10), leading to minimization of the total spread. Eqn.4.10 also suggests that the total spread will reduce with increasing number of states (N) in the basis of which the first moment matrices are constructed.

We test the proposed approach first with FMMs computed in the basis of GTOs constructed for Ti with parameters from Ref..[108] In Fig.4.1 we plot the charge centres($\langle\phi|\vec{r}|\phi\rangle$) of the approximate eigen states of the first moment matrices. Evidently, the charge centres constitute coordination polyhedra around isolated atoms which are consistent in shape with those tabulated in Figs.6-8 in Ref..[109] This agreement confirms the identity of the resultant orbitals as the hybrid orbitals and numerically establishes the connection between maximal localization and hybridization. Such a connection between sp^3 hybridization and minimization of total quadratic spread of s and the three p orbitals has been analytically proven.[110] In this work however we do not use GTOs further and rather resort to KS states of isolated atoms.

(a) $sp^3, d_{x^2-y^2}, d_{z^2}$ (b) $sp^3, d_{x^2-y^2}, d_{xy}$ (c) sp^3, d_{xy}, d_{xz} (d) sp^3, d_{z^2}, d_{xz}

(e) $sp^3, d_{x^2-y^2}, d_{z^2}, d_{xy}$ (f) $sp^3, d_{z^2}, d_{xy}, d_{zx}$ (g) $sp^3, d_{z^2}, d_{yz}, d_{zx}$

(h) $sp^3, d_{x^2-y^2}, d_{xy}, d_{yz}, d_{zx}$ (i) $sp^3, d_{z^2}, d_{xy}, d_{yz}, d_{zx}$ (j) $sp^3 d^5$
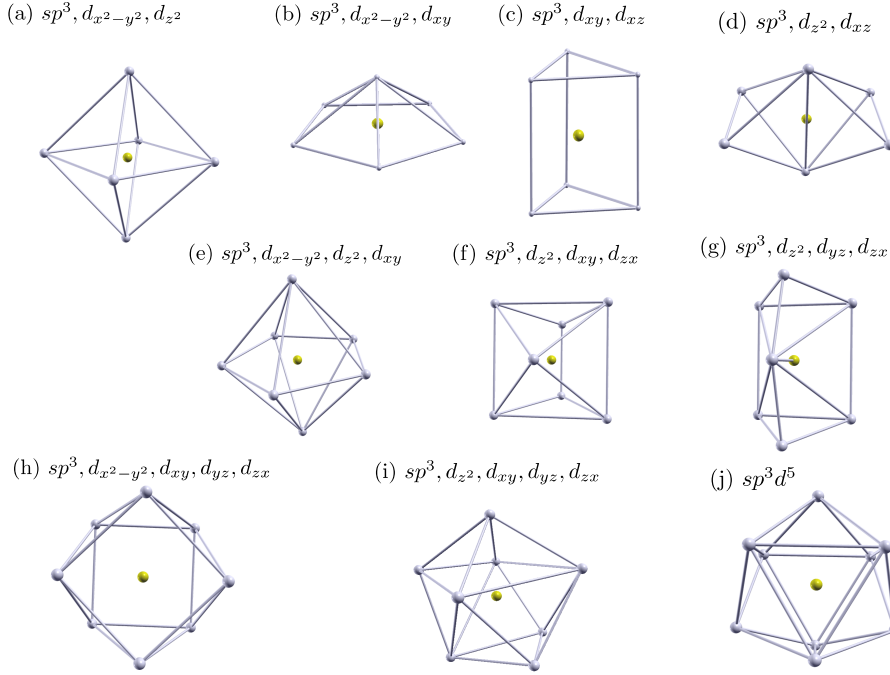
Figure 4.1: Plots of charge centres (shown in gray) of the hybrid orbitals formed by the group of GTOs representing $3s, 3p$ and $3d$ orbitals of Ti (shown in yellow) constructed as per Ref..[108]

For example, for atoms of the p block, such as boron, carbon, nitrogen and silicon dealt with in this work, if the first moment matrices are constructed in the basis of three(four) KS states with lowest energies, namely, the one s like non-degenerate having the lowest energy and two (three) of the three p like degenerate states above the s like state, the approximate eigen subspace would render three(four) $2sp^2(2sp^3)$ hybridized orbitals. Notably, for isolated systems like molecules, clusters and nanostructures, the approximate common eigen spectrum of the FMMs computed within the manifold of occupied KS states results into partitioning[111,112,113] of the ground state charge density into bonding and localized orbitals.

4.1.1.1 Orientation and transfer of orbitals

Although as evident above that construction of HAOs for an isolated atom as such do not require any pre-defined directionality, the orientation of the HAOs associated with an atom can be nevertheless locked to their anticipated neighbourhood by

placing the isolated atom within an external potential which represents the generic or exact atomic neighbourhood of the given atom in the actual system in which the HAOs are to be used. We construct such externals potentials by placing weakly confining spheres with small constant negative potentials inside the spheres in place of exact or generic locations of neighbouring atoms as present in the actual system. For example, to lock sp^3 HAOs to a four coordinated tetrahedral neighbourhood, a tetrahedra of confining spheres is placed around the host C atom, leading to orientation of the sp^3 orbitals maximally in the direction of the confining spheres as seen in Fig.4.5(a). Typically we find confining potential amplitudes in the order of 0.01 eV and radius 0.5Å to be sufficient for the purpose. Such weak confinement in the vicinity causes change of KS energy eigen-values of isolated atoms in the order of 0.001 eV, and retains the shape of the lowest KS states which are used for construction of the HAOs, effectively unaltered. For sp^3 HAOs, the tetrahedra of the confining spheres can be an exact tetrahedra, as in case of bulk Si, or a strained tetrahedra, as in case of cyclopropane. As evident in Fig.4.2(a) for cyclopropane, and in Fig.4.2(b-e) for planar molecules C_nH_n, the projected charge center of the HAOs (shown in gray) symmetrically deviate away from the C-C bonds with decreasing C-C-C angle as we go from C_6H_6 to C_3H_3. For all of these molecules the HAOs were constructed with the weakly confining spheres placed around the host C atom exactly as per their nearest neighbours in the molecules, resulting into HAOs largely retaining their pure sp^3 nature but oriented symmetrically about the directions of the confining spheres from the host atoms. The placement of confining potential spheres thus provide a gross directional reference for orientation of the full set of

(a)   (b)   (c)   (d)   (e)
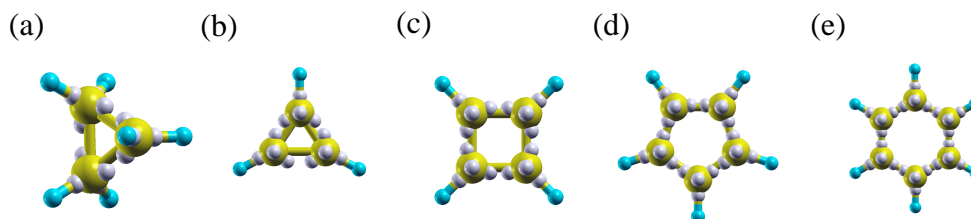
Figure 4.2: Projected charge centres of HAOs are shown by gray spheres depicting their orientations around their host C atom shown in yellow.
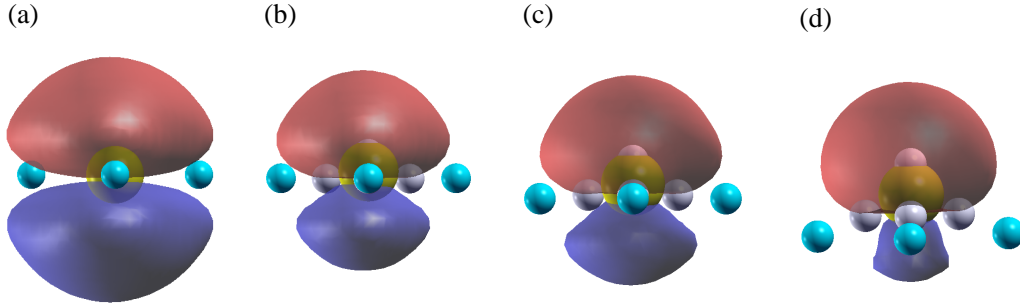
Figure 4.3: (a-d): Evolution of a pure $2p_z$ orbital[(a)] from sp^2 hybridization background, to an sp^3 hybridized orbital due to increased deviation of the centres (cyan spheres) of the three confining potential spheres from co-planarity with the host atom (yellow sphere). Centres of HAOs are shown by gray spheres.

the HAOs.

Position of charge centres of the HAOs are learned in terms of the directions of the confining spheres from the isolated host atom. Such learnings are subsequently used in projecting centres of HAOs around the corresponding atom in a given system, as seen for the molecules in Fig.4.2, and nano-diamonds in Fig.4.4. While transferring HAOs from their nursery of isolated host atoms, to their matching host atoms in a given system, HAOs are rotated such that their actual charge centres align along the direction of their projected centers from the matching host atoms.

In addition to providing reference for orientation, the confining spheres can have an important role in deciding the level of hybridization of the HAOs. This becomes evident by noting that if we use four KS states and three confining sphere coplanar with the host atom, then instead of forming four sp^3 orbitals, the HAOs separate into three $2sp^2$ orbitals and one $2p_z$ orbital, as evident from the unhybridized shape of the $2p_z$ orbital in Fig.4.3(a). Fig.4.3(a-d) shows evolution of the $2p_z$ HAO from a pure orbital perpendicular to the plane of sp^2 hybridization, towards a $2sp^3$ hybridized orbital, with increasing non-coplanarity of the confining spheres with the host atom. HAOs with such intermediate hybridization ($2sp^{2+} + 2p_z^+$) has been used for C_{60}. However, stronger confining potentials are found necessary to influence hybridization of KS states, typically in the order of 1eV for C atoms, such that the orbitals align along the confining spheres. The confining potentials in this case therefore does lead

(a) C_3H_8

(c) $C_{26}H_{32}$

(d) $C_{84}H_{64}$

(b) $C_{10}H_{16}$
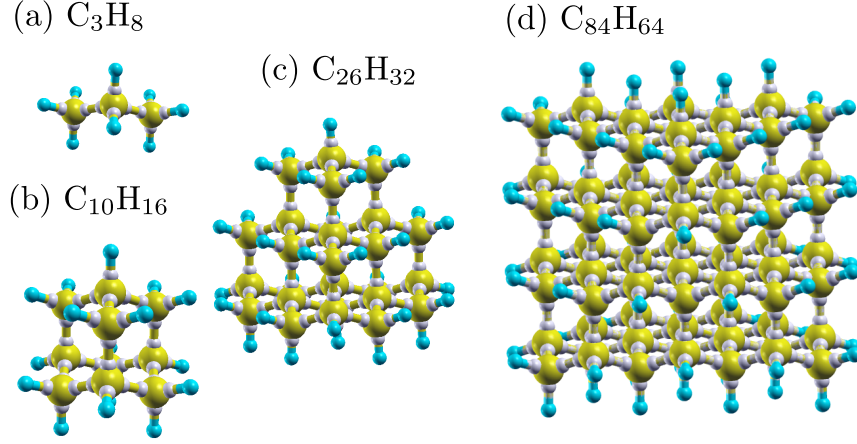
Figure 4.4: C_nH_m systems with projected charge centre of HAOs shown as gray spheres, used in this work as example of sp^3 hybridized covalent systems.

to minor modification of shape of the KS states, and thereby of the HAOs as well, although not quite obvious at the iso-surfaces plotted in Fig.4.3(a-d). However the values of TB parameters calculated in the basis of their Wannierized counterparts in C_{60} suggests that the overall shape of those orbitals are largely retained close to the sp^2 orbitals. Notably, we could have used stronger confinement to align the HAOs in C_3H_6, C_3H_3 or C_4H_4 as well like we did for C_{60}, but the degree of confinement would have to be much high than that used for C_{60}, which would have substantially altered the shape of the HAOs themselves, since it is obvious that with pure s, p_x, p_y, p_z orbitals it is impossible to form any set of hybrid orbitals in which two orbitals can have relative orientation less than $90°$.

The next step is to construct orthonormalized Wannier functions from the KS states following the HAOs transferred to a given system. The transferred HAOs constitute a non-orthogonal basis of hybridized atomic orbitals. In the general framework of periodic systems with non-zero wave-vectors ($\vec{k}$) we begin with constructing a non-orthogonal set of quasi-Bloch states from the non-orthogonal basis of transferred HAOs from the isolated atoms. In the method described in Section 3.2 we obtain the orthonormal Wannier function counterparts of the transfered HAOs.

Notably the elements of O in Eqn.(3.2) record the representation of the HAOs

74

Hybrid atomic orbital basis from first principles: Bottom-up mapping of self-energy correction to large covalent systems

(a)   (b)   (c)
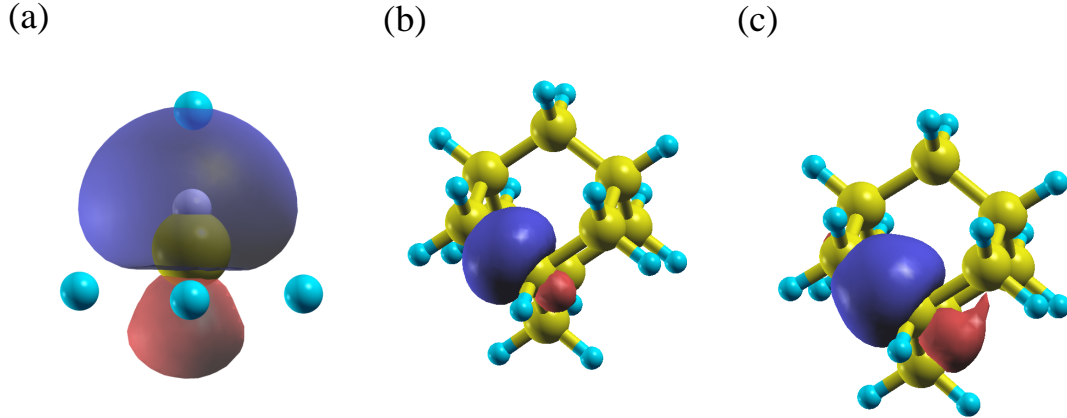
Figure 4.5: (a): HAO representing a sp^3 orbital of an isolated C atom (yellow sphere) used in this work. Charge centre of the orbital is shown in gray. Centres of the confining spheres used to determine gross orientation are shown in cyan. (b): HAO shown in (a) transfered to a C atom an adamantane($C_{10}H_{16}$) molecule, (c): the corresponding HAWO.

within the manifold of KS bands considered. Overlaps between the non-orthogonal quasi-Bloch states within the manifold of the considered KS states are recorded in S as in Eqn.(3.3). The degree of representability of HAO ϕ_n, within the set of KS states considered, is guaranteed by setting a lower cutoff on individual $S_{\vec{k},n,n}$ values to be typically more than 0.85. For all the system studied in this work, the above criteria is found to be satisfied by the lower bound on the number KS states, which is set by the total number of valence orbitals of all atoms of a given system. A new set of orthonormal Bloch states from the KS single particle states are subsequently constructed using the Löwdin symmetric orthogonalization[76] scheme as shown in Eqn.(3.4). Subsequently, a localized set of orthonormal Wannier functions are constructed as given in Eqn.(3.5). In this process the Löwdin symmetric orthogonalization clearly provides a choice of gauge for linear combination of KS states such that the resultant Wannier functions [Eqn.(3.5)] resemble the corresponding HAOs as much possible within the manifold of KS states considered. Hence we refer to these Wannier functions as the hybrid atomic Wannier orbitals ("HAWO"). In Fig.4.5 we show an HAO before and after transfer to adamantane and the corresponding HAWO constructed from the KS states of adamantane. HAWOs can thus be considered as analogue of NHOs constructed from a given set of KS states
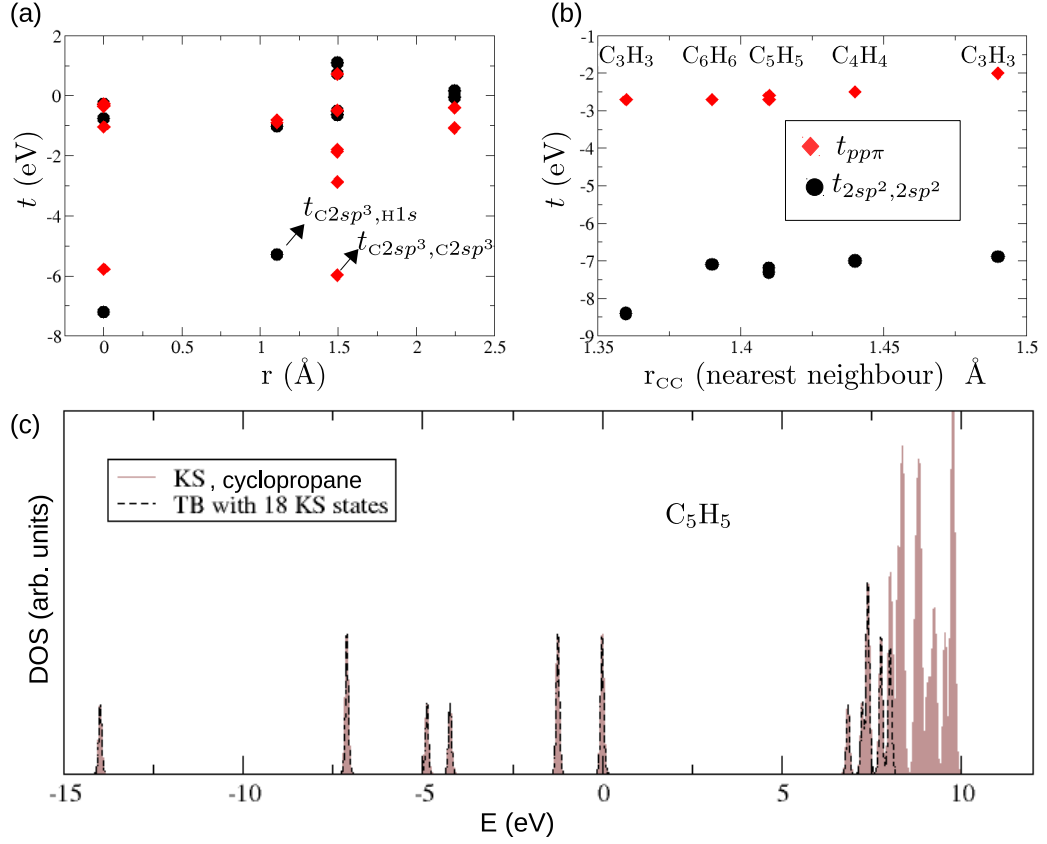
Figure 4.6: (a): TB parameter calculated for cyclopropane; (b): Nearest neighbour TB parameters between in-plane and out of plane orbitals in C_3H_3, C_4H_4, C_5H_5 and C_6H_6 molecules (shown in Fig.4.2) arranged as a function of C-C bond lengths available in the molecules. (c) DOS calcaulated from 50 lowest KS eigen-values, compared with DOS from eigen-values of TB hamiltonian constructed from 18 lowest KS states, 18 being the total number of valence orbitals of cyclopropane.

with acceptable representability. TB parameters in the HAWO basis are computed from energetics of KS single particle states as given in Eqn.(3.6). Notably, similar TB parameters have been derived in the last two decade from first principles based on the either the maximally localized Wannier function[50,52,53,54,114,115] or atomic orbitals[49,116] constructed from KS states. Much effort has been reported in deriving TB parameters through projection of KS states on pseudo-atomic orbitals[117,118] as well. However, attempts to calculate TB parameters in hybrid atomic orbital basis constructed from first-principles, as proposed in this work, has been limited so far primarily to analytical models.[119,120]
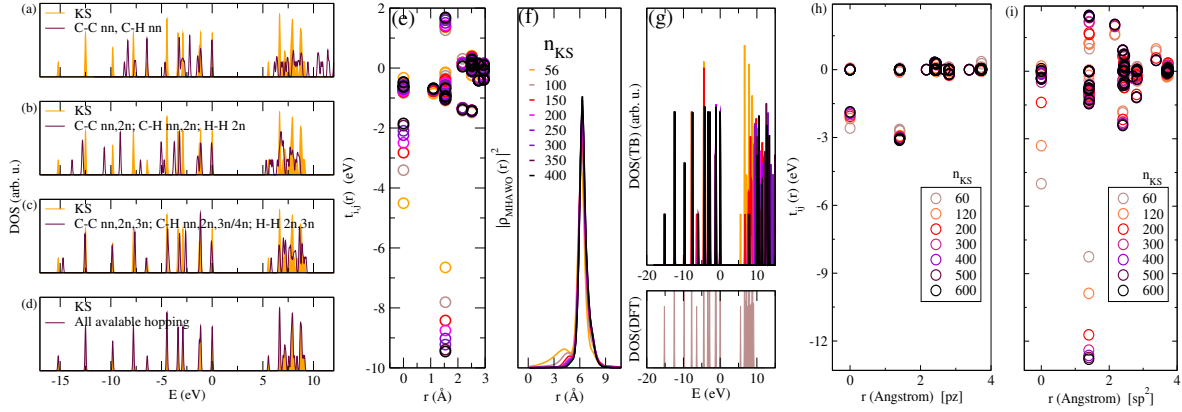
Figure 4.7: For $C_{10}H_{16}$, (a-d): Evolution of density of states(DOS) with increase in range of hopping starting from (a): the nearest neighbour (nn) to (d): all avaliable hopping graduating through hopping between second (2n) and third (3n) nearest neighbours and beyond. Convergence of (e): TB parameters and (f): spatial localization of $2sp^3$ orbitals, and (g): TB DOS, in terms of the number of KS states used in construction of HAWOs as mentioned in the legend of (f). KS DOS is shown below (g). Similar convergence of TB parameters for (h): $2p_z$ and (i): $2sp^2$ orbitals in AGNR (3p+1, p=2).

In principle to construct hybridized atomic orbitals as the tight-binding basis for a given system, we can indeed start with a template of pure analytic atomic orbitals and then Wannierize them in the basis of the KS states of the given system. To construct the basis directed towards coordination, we then need to hybridize the Wannierized atomic orbitals for every atom individually as per the orientation of the local neighbourhood. In principle, we can start with a standard hybridization matrix and add extra rotation to orient the hybridized orbitals according to the orientation of the local neighbourhood. However, with higher orbitals like d beyond s and p, the hybridization matrices for different combination of orbitals (as considered in Fig.4.1) are not readily available.

Alternately, in our work we construct the Wannier orbitals starting from a template which is already hybridized and oriented as per the local neighbourhood of each atom. Instead of hybridizing analytic atomic orbitals explicitly for each atom to build the template, we populate the template by numerically computed hybrid orbitals which are directly obtained from the KS states of the isolated atoms as the approximate eigenstates which maximally joint diagonalize the non-commuting first

moment matrices calculated in the basis of KS states. The KS states of the isolated atoms are obtained using the same pseudo-potential which is used in the real system where the orbitals are to be used. This step ensures good representability(typically more than 90%) of the template in the basis of KS states, which is crucial for localization. To populate the template, the resultant hybrid orbitals are re-oriented as per the orientation of the neighbourhood of each atom. In the thesis work we used weak confining potential spheres around the isolated atoms to mimic its local neighbourhood in the real system. With confining potentials weak enough to impacted the KS eigenvalues of the isolated atom below the second place of decimal in eV, the resultant KS states render hybrid orbitals which align symmetrically with respect to the location of the confining potentials, if not exactly along them, as is the case for sp^3 orbitals with tetrahedrally oriented confining spheres for example. In general for bonding as well as non-bonding orbitals, the angle made by the direction of the hybrid orbitals and the direction of the confining spheres are recorded and used in the real system to align the orbitals as per the neighbourhood of each atoms. The rigour in this part is equivalent to that of finding the correct rotation matrix if we had to do with the Wannierized atomic orbitals. In the thesis work, ad-hoc confining potentials with modest potential have been also used to influence hybridization itself. For example in C_{60}, where the relative directions of coordinations deviate substantially from that of the sp^3 orbitals, we used a stronger confining potential than that mentioned above, to alter hybridization in order to align the orbitals along the exact direction of coordinations.

However, in a work completed post submission the thesis we have discarded the use of confining potential to alter hybridization, and have rather used hybridization matrices of appropriate symmetries to allowed customization of hybridization to orient the hybrid orbitals in relative directions which deviate from that of the fully degenerate hybrid orbitals (such as sp^2, sp^3, sp^3d^5), and have shown that the optimal set of hybrid orbitals for a given neighbourhood may not be the exactly aligned along the direction of coordination.

Finally, the reason why we prefer the direct construction of the fully degenerate

orbitals over the explicit hybridization of the Wannierized pure atomic orbitals is that the former are obtained through a mathematically exact framework of maximal joint diagonalization which ensures maximal localization, whereas the Wannierization procedure is not unique and the process of numerical minimization of spread is known to be sensitive to the shape of orbitals in the template. Furthermore, with d and higher orbitals along with s and p orbitals, the direct construction of the degenerate sets of hybrid orbitals from KS states of isolated atoms, as demonstrated in Fig.4.1, can be accomplished without needing to derive the exact hybridization matrix.

In Fig.4.6(a) for cyclopropane, we plot the TB parameters calculated as per Eqn.(3.6) for two HAOs participating dominantly in a C-C bond and a C-H bond. The t_{sp^3,sp^3} is comparable to the that in adamantane $(C_{10}H_{16})$[Fig.4.12] despite the substantial misalignment[Fig.4.2] of HAO and the C-C bond in cyclopropane while perfect alignment of the two in $C_{10}H_{16}$. The hopping parameters are obtained with 18 KS states which is same as the total number of valence orbitals of all the atoms, resulting thereby into density of states in exact agreement with that obtained from DFT [Fig.4.6(c)] as discussed above in the next paragraph. In Fig.4.6(b) we plot hopping parameters for π and σ bonds as a function of C-C bond lengths available in planar C_3H_3 to C_6H_6 molecules. As evident in Fig.4.2, the best alignment of the HAOs along the C-C bond is possible for C_6H_6 and the worst is obviously for the shorter bond of C_3H_3 and similarly for C_3H_6. Yet, the highest in-plane hopping parameter in terms of magnitude is found for the shorter bond of C_3H_3, which is about 20 % more than that of the C-C in-plane bond of benzene, whereas the C-C bond length in benzene only about 2.2 % more than the shorter bond of C_3H_3. Similarly, the C-C nearest neighbour hoping parameter as well as the bond length in C_3H_8, both are within 1 % of those of C_3H_6, whereas in C_3H_8 the HAOs are almost perfectly aligned along the C-C bond [Fig.4.4] while in C_3H_6 they are misaligned by more than 20°. These results can possibly be explained by the inherent bent nature the bonds[121] in C_3H_6 and C_3H_3, reflected by the symmetric misalignment of the HAOs along the two C-C bonds while maintaining perfect alignment along the

C-H bonds. We plan to examine this aspect for bent bonds in details in future.

As evident in Fig.4.7(a) for $C_{10}H_{16}$ the edge of the valence band is already well described if we consider only the nearest neighbour hopping in the HAWO basis. However, as shown in Fig.4.7(b) onwards, the match of DOS from TB and DFT improves drastically with increasing extent of hopping considered up to the second nearest neigbour. This is immediately understood by noting the non-nominal positive valued of the second nearest hopping element plotted in figure Fig.4.7(e), arising due to proximity of lobes of different signs of the two HAOs. In Fig.4.7(e-g), we demonstrate evolution of the TB parameters, HAWOs, and DOS from TB, as function of number of KS states considered for construction of HAWOs. The rationale for this analysis is the possibility that the anti-bonding subspace may not be adequately represented by the unoccupied KS states if we restrict the total number of KS states to be same as the total number of HAOs associated with all the atoms, which is same as the total number of valence orbitals of all the atoms. Indeed we see clear convergence of shape of HAWO [Fig.4.7(f)] as well as the corresponding TB parameters[Fig.4.7(e)] if we consider KS states in excess of the total number of HAOs. Fig.4.7(h,i) suggests that the convergence can be much quicker for un-hybridized orbitals like $2p_z$, compared to hybridized orbitals like sp^2 and sp^3, since the un-hybridized orbitals primarily constitutes the edges of the valence and conduction bands. However, the TB DOS expectedly starts deviating from the DFT DOS more in the conduction band [Fig.Fig.4.7(g)] if we include more KS states beyond the total number of HAOs, owing to the semi-unitary nature of the net transformation matrix ($OS^{\frac{1}{2}}$) implied in Eqn.(3.4) which will be rectangular in such scenarios. It is thus important to decide on the number of KS states to be considered depending on the purpose. If the aim is to represent only the valence bands through well localized HAWOs, then it may be prudent to look for convergence of HAWOs in terms of KS states. But if band-gap needs to be represented accurately by the TB parameters then the number of KS states should be kept same as the total number of valence orbitals.

4.1.2   Bottom-up mapping of TB parameters

The HAWO basis derived from the KS states offer a multi-orbital TB basis which
are by construction locked to the local coordination as per the atomic neighbour-
hood of each atom. The TB parameters derive in such a basis should therefore
be transferable from one system to another with matching atomic environment. A
key aim of this work is to demonstrate such transferability for effective transfer of
multi-orbital TB parameters in the HAWO basis from smaller reference systems to
larger target systems. The mapping of TB parameters is done in two steps.

(1) Pairs of atoms of the target system, not limited to nearest neighbours, are
mapped on to pairs of atoms in the reference system based on a collection of crite-
ria.

(2) Among the mapped pair of atoms, pair of system orbitals are mapped to pair of
reference orbitals through mapping of their respective projected charge centres. In
step (1) the criteria to map pairs of atoms include matching structural parameters
such as their spatial separation and their individual nearest neighbourhoods char-
acterised in terms of the type of neighbouring atoms and angles made by nearest
neighbours on the atoms. In particular, we use a parameter calculated as:

$$\zeta_i = \sum_j^{N_i} Z_j w(r_{i,j}) \tag{4.11}$$

where N_i is the number of neighbours of the i-th atom within a suitably chosen
cutoff radius, w being a weight factor which is a function of the distance $r_{i,j}$ of the
j-th neighbour of the i-th atom, and Z_i a characteristic number to be associated
with each type of atom. Z_i can be chosen to be the atomic weight, as we mostly
used in this work, or a similar number which can facilitate identification of a type
of neighbourhood or a region of the system through values of ζ. In this work we
chose the weight factor w to be 1.0 within half of the cutoff radius beyond which
the factor is smoothly reduced to zero using a cosine function. The choice of cutoff
radius depends on the size of the reference system. It should neither be too large

for variations to average out, nor should it be too small to become insensitive to morphological variations in the reference system itself. ζ allows us to map atom pairs effectively through prudent choice of values of $\{Z_i\}$ since it would allow assessment of proximity of atoms to edges, interfaces or any kind of structural inhomogeneity without any exhaustive structural relaxation.

In step 1, the minimum of the deviation:

$$|\zeta_1^{\text{target}} - \zeta_1^{\text{reference}}| + |\zeta_2^{\text{target}} - \zeta_2^{\text{reference}}|$$

obtained within a range of allowed deviation of structural parameters, is used as the criteria to choose matching pairs of atoms between target and reference systems.

Like in step 1, in step 2 as well, the mapping of one or a pair of HAOs from the reference to target systems is done based on matching structural parameters, as well as a parameter calculated as:

$$\xi_i = \sum_{j}^{N_i} \zeta_j w^{WC}(r_{i,j}) \tag{4.12}$$

where ζ_j corresponds of the j-th atom in the neighbourhood defined by w^{WC} around of the projected charge centre of the i-the HAO. Angle made by the directions of the projected charge centres of the HAOs from their respective host atoms is a key matching parameter in step 2. Additionally, if the HAOs belong to different atoms then the dihedral angle made by the centres of the HAOs through the axis connecting their host atoms, is also a key parameter. Thus in step 2, the minimum of the deviation

$$|\xi_1^{\text{target}} - \xi_1^{\text{reference}}| + |\xi_2^{\text{target}} - \xi_2^{\text{reference}}|$$

within acceptable deviations of structural parameters, defines matching pairs of HAOs.

As an example we show mapping from a small curved finite patch[Fig.4.8(a)]

to C_{60}. Since C_{60} constitutes a curved surface without any edge, mapping should be done from the inner most neighbourhood of the chunk. Since in C_{60}, the angles made by nearest neighbours at a given atom differ distinctly depending on whether an angle opens inside a pentagon or a hexagon, the matching parameters for mapping are mostly structural, primarily the direct and dihedral angles. The reference patch is cropped from C_{60} and passivated by H. We fix ζ tolerance to zero which implies that C_{60} is getting mapped from only six C atoms of the patch [Fig.4.8(a)] having all C neighbours. Given the curvature of C_{60}, we chose to use confining spheres to influence the hybridization of sp^2 HAOs in order to break their coplanarity and align them along nearest neighbour C-C bonds, as shown in Fig.4.3(c) where the placement of confining potential spheres are as per the nearest neighbourhood in C_{60}. The projected charge centres of HAOs with intermediate hybridization ($2sp^{2+}+2p_z^+$) between (sp^2+p_z) and sp^3 shown in Fig.4.8(c), is used to map from that of the reference shown in Fig.4.8(b). TB parameters $t_{2sp^{2+},2sp^{2+}}$ for the shorter and longer C-C bonds are about -6.9 eV and -6.5 eV, whereas $t_{2p_z^+,2p_z^+}$ are about -2.36 eV and -2.0eV. The match of the DFT DOS with the DOS from TB parameters mapped from the reference system is shown in Fig.4.8(d), which can be further improved beyond the valence bond by considering HAOs for exautocited states, which will be taken up in a subsequent work on optical properties.

4.1.3   Self-energy correction of TB parameters

Self-energy corrected TB parameters $\left\{ t^{QP}_{\vec{R}',\vec{R},i,j} \right\}$ in the HAWO basis are calculated by substituting $E^{KS}_{\vec{k},n}$ in Eqn.(3.6) by quasiparticle energies $E^{QP}_{\vec{k},n}$ obtained at the G_0W_0 level which is the first order non-self-consistent GW approximation[6,41] of MBPT.[4,5,122,123,124] Within the GW approximation, the quasi-particle energies are approximated as[Eqn.(3.8)]:

$$E^{QP}_{\vec{k},n} = E^{KS}_{\vec{k},n} + \langle \psi^{KS}_{\vec{k},n} \mid \Sigma - V^{KS}_{xc} \mid \psi^{KS}_{\vec{k},n} \rangle, \qquad (4.13)$$
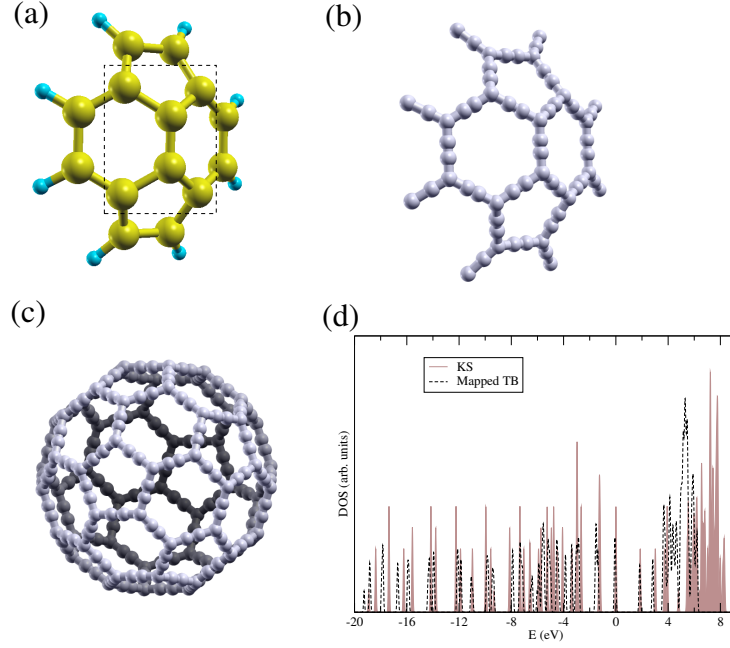
Figure 4.8: (a): Structure of reference system, and (b): the corresponding charge centres of HAOs with intermediate hybridization ($2sp^{2+}+2p_z^+$) between sp^2 and sp^3. (c): Projected charge centre with similar hybridization for C_{60}. (d): Corresponding matches of DFT DOS with TB DOS with parameters mapped from the reference system.

where V_{xc}^{KS} is the mean-field exchange-correlation potential and Σ^6 is the self-energy operator derived by considering the many-electron effects as perturbation treated within a self-consistent framework of Dyson's equation formulated in terms of the one-particle dynamic non-local Green's function constructed from the KS states. Similar efforts have been reported in recent years on incorporating SEC in TB parameters computed in terms of the MLWFs.[72,73,125] Incorporation of SEC in TB parameters has also been attempted through matching specific bands of the QP structure.[71,74,126]

4.2   Computational Details

Electronic structures of the ground states of all the systems considered in this work are calculated using the Quantum Espresso (QE) code[77] which is a plane wave based implementation of DFT. We have used norm conserving pseudo-potentials with the
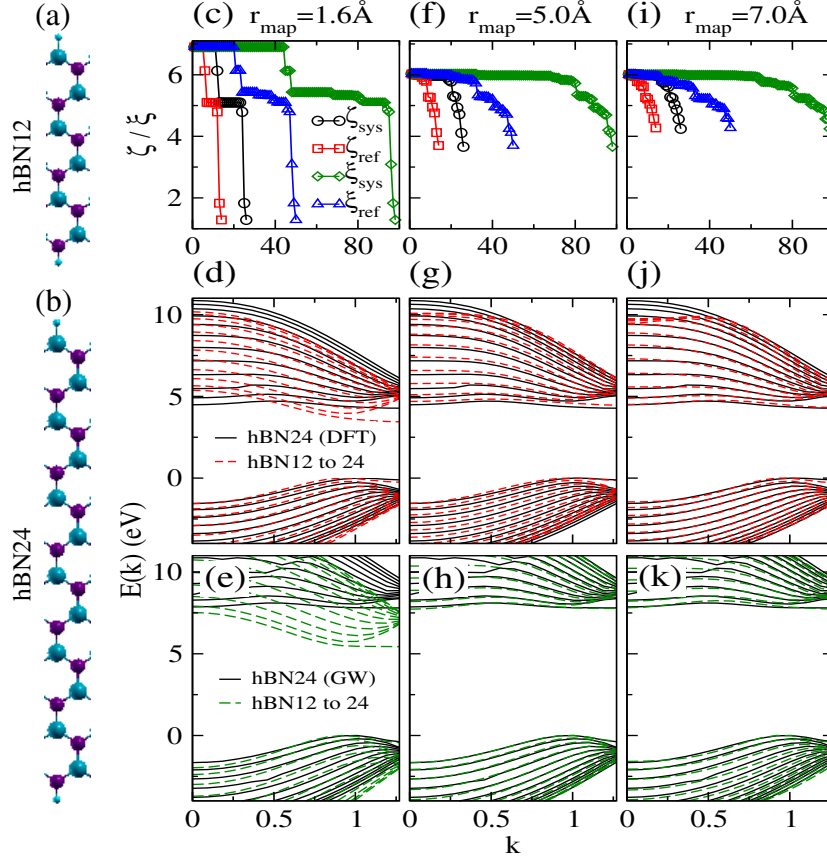
Figure 4.9: (a,b) Hexagonal zigzag boron nitride nanoribbons(hZBNNR: hBN), hBN12 and hBN24 respectively. (c,f,i) Plot of ζ and ξ values "ref"(reference hBN12) and "sys"(target hBN24) for different spatial ranges of neighbourhood considered for mapping. (d,g,j) Matching of DFT band-structure and mapped TB band-structure for increasing r_{map}. (e,h,k) Matching of DFT+G_0W_0 band-structure and mapped self-energy corrected TB band-structure for increasing r_{map}.

Perdew-Zunger (LDA) exchange-correlation[56] functional and a plane wave cutoff of 60 Rydberg for wave-functions and commensurately more for charge density and potential. Variable cell structural relaxation has been carried out for all periodic systems using the BFGS scheme. To avoid the spurious interactions between the periodic images we used more than 10 Å separation as a vaccum. We used a 1x1x15 Monkhorst-Pack grid of k-point for AGNRs and 1x1x29 for ZGNRs as well as for ZBNNRs. Self-energy correction to single particle levels have been estimated at the non-self-consistent G_0W_0 level of GW approximation implemented in the Berke-leyGW code.[42] To calculate the static dielectric matrix required for computation of the self-energy operator, the generalized plasmon-pole model[6] is used to extend
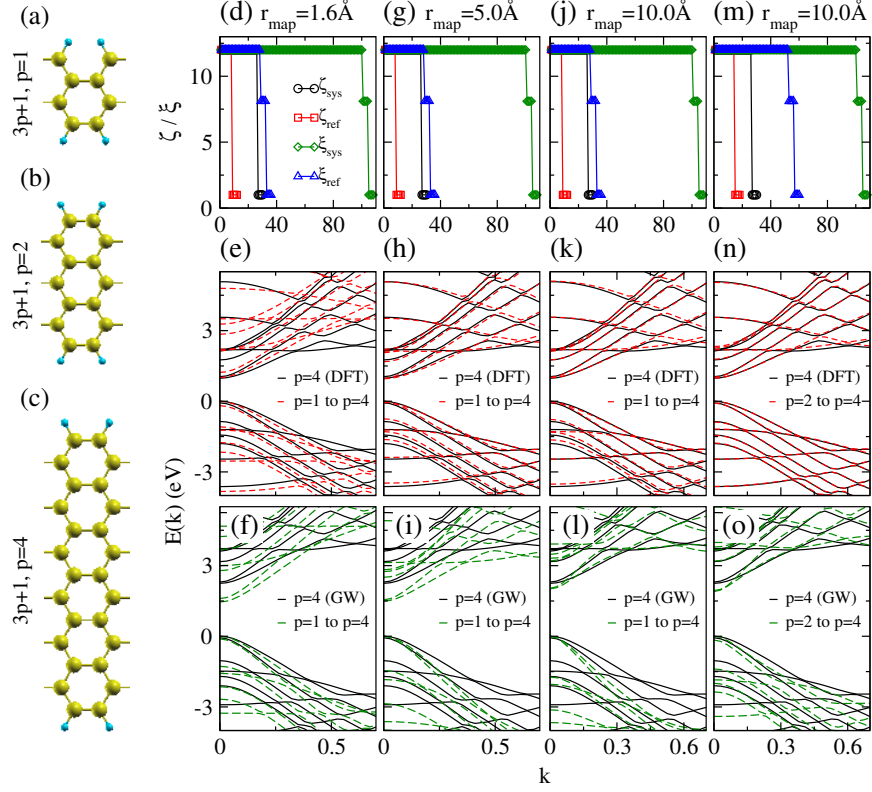
Figure 4.10: (a,b,c) Armchair graphene nanoribbons (AGNR) of family n=3p+1 with p=1, p=2 and p=4 respectively. (d,g,j,m) Plot of ζ and ξ values "ref"(reference p=1 (in d,g,j) and p=2 (in m)) and "sys"(target p=4) for different spatial ranges (r_{map}) of neighbourhood considered for mapping. (e,h,k,n) Matching of DFT band-structure and mapped TB band-structure for increasing r_{map}. (f,i,l,o) Matching of DFT+G_0W_0 band-structure and mapped self-energy corrected TB band-structure for increasing r_{map}.

the static dielectric matrix in the finite frequencies. Energy cutoff of 10 Rydberg is used for the dielectric matrix and Coulomb truncation is according to the systems dimension. To convergence the dielectric function and the self-energy term we used 250(5000) bands for extended(nano-diamonds) systems. For all the nanoribbons parameters are chosen from Ref..[75] In house implementation interfaced with the QE code is used for generation of HAOs, HAWOs from KS states, calculation of TB parameters in the HAWO basis, and mapping of TB parameters from reference to target systems.

86

Hybrid atomic orbital basis from first principles: Bottom-up mapping of self-energy correction to large covalent systems
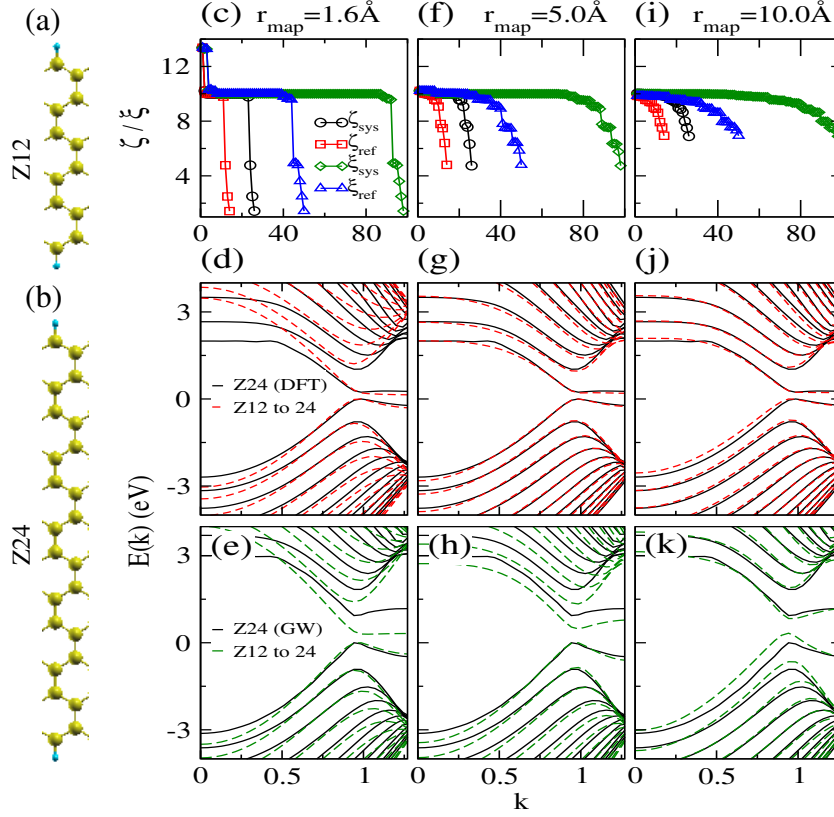
Figure 4.11: (a,b) Zigzag graphene nanoribbons (ZGNR: Z), Z12 and Z24 respectively. (c,f,i) Plot of ζ and ξ values "ref"(reference Z12) and "sys"(target Z24) for different spatial ranges of neighbourhood considered for mapping. (d,g,j) Matching of DFT band-structure and mapped TB band-structure for increasing r_{map}. (e,h,k) Matching of DFT+G_0W_0 band-structure and mapped self-energy corrected TB band-structure for increasing r_{map}.

4.2.1 Mapping self-energy corrected TB parameters in HAWO basis

4.2.1.1 Nanoribbons

In previous Chapter 3 we shown estimation of quasi-particle(QP) band-gap for graphene and hBN nano-ribbons based on SE correction to TB parameters mapped from narrower ribbons in the basis of a single $2p_z$ electron per atom. The transfer was made explicitly by identifying equivalent atoms based on proximity to the ribbon edges as shown in Fig.[3.2](c-e), Fig.[3.3](f) and Fig.[3.5](a) in Chapter 3. In this section we begin by systematizing the process of identifying the equivalent
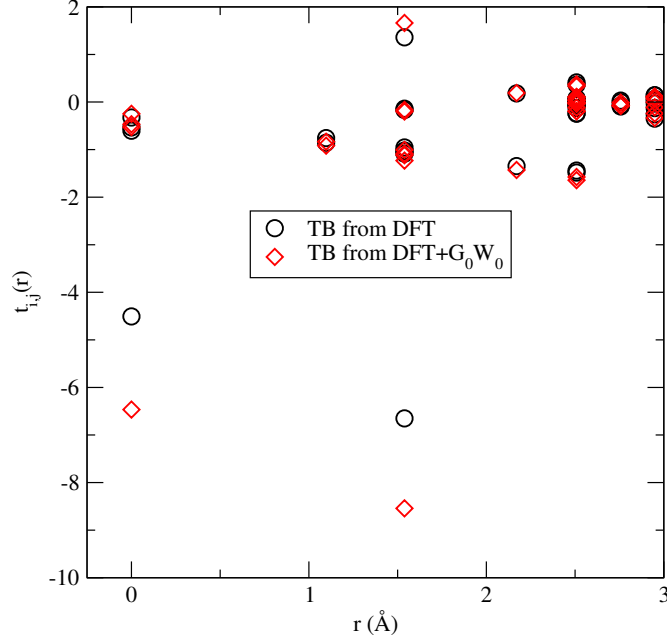
Figure 4.12: TB parameters involving a C atom in $C_{10}H_{16}$ with three C neighbours, computed using 56 KS states with and without SEC at the G_0W_0 level, and plotted as a function of distance from the atom. TB parameters from DFT are same as those plotted in Fig.4.7(e).

atoms through the mapping mechanism proposed in Sec.4.1.2. The identification is primarily based on ζ values for atoms and ξ values for HAO charge centres wherever sufficient variations of ζ and ξ are available in the reference systems, as demonstrated in Fig.4.9(c,f,i) and Fig.4.11(c,f,i) for hBN and ZGNR respectively. Whereas, mapping of AGNR from p=1 to p=4, as shown in Fig.4.10(d,g,j,m), calls for matching of structural parameters as the key strategy for mapping, since the width of reference AGNR with p=1 of the 3p+1 family, is narrow enough and have only two types of C atoms per unit-cell.

For hBN, acceptable match[Fig.4.9(g,j and h,k)] between explicitly computed band-structure, and the same computed from TB parameters with only $2p_z$ orbitals mapped from a narrower ribbon [Fig.4.9(a)], is achieved simultaneously at the DFT and DFT+G_0W_0 levels, with hopping considered within the range no less than 5Å. Whereas a higher spatial range of mapping of self-energy corrected TB parameters is required for matching of band-structure at the DFT+G_0W_0 level for AGNR [Fig.4.10(l)], and more so for ZGNRs [Fig.4.11(k)] with smaller band-gaps. Notable

Figure 4.13: Distribution of distance between pairs of atoms in (a): reference (C_3H_8) and (b): target ($C_{10}H_{16}$) systems. (c-d) Match between DFT DOS and mapped TB DOS as demonstrated of efficacy of mapping of TB parameters from C_3H_8 to $C_{10}H_{16}$ with increasing spatial range of neighbourhood considered for mapping. (e) Match between DFT+G_0W_0 DOS and mapped self-energy corrected TB DOS.

for AGNR, the match of self-energy corrected band edges for p=4 naturally improve with mapping from p=2 [Fig.4.10(o)]. These trends simply relate to the degree of localization of the states at the band edges - the more they are delocalized the larger is the spatial range within which the self-energy correction to TB parameters are to be considered.

4.2.1.2 Nano-diamonds

Fig.4.12 suggests that the extent of SEC to TB parameters are spatially limited mostly within the third nearest neighbourhood, implying possible transferability of SE corrected TB parameters to large covalent systems from smaller reference systems of which are large enough to accommodate the full spatial range of non-nominal SEC to TB parameters. Accordingly, mapping in nano-diamonds is demonstrated with C_3H_8 and $C_{10}H_{16}$ (adamatane) as reference systems to map to nano-diamonds $C_{26}H_{32}$ (pentamantane) and $C_{84}H_{64}$.
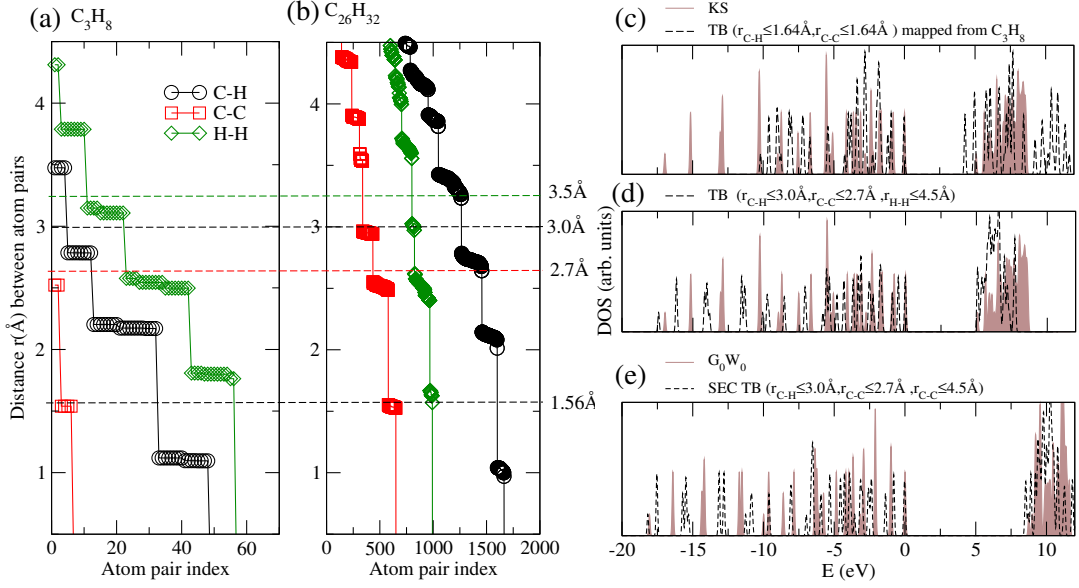
Figure 4.14: Distribution of distance between pairs of atoms in (a): reference (C_3H_8) and (b): target ($C_{26}H_{32}$) systems. (c-d): Match between DFT DOS and mapped TB DOS as with an increasing spatial range of neighbourhood considered for mapping. (e): Match between DFT+G_0W_0 DOS and mapped self-energy corrected TB DOS.

We start with attempts to map $C_{10}H_{16}$, $C_{26}H_{32}$ and $C_{84}H_{64}$ targets from C_3H_8 reference in sp^3 HAO basis. The mapping process starts with plotting the distance of atom pairs (C-H, C-C, H-H) for target and reference systems. As seen in Fig.4.13(a) there is one-to-one correspondence of C-C bonds between C_3H_8 and all targets up to approximately 2.5Å, which is the second nearest C-C distance. For C-H and H-H pairs, such correspondence exists up to about 3Å and 3.75Å respectively. These correspondences decide the range of hopping parameters to be mapped. Notably, C_3H_8 has two varieties of C atoms - one with two(two) C(H) neighbours, and the other with one(three) C(H) nearest neighbours, whereas, $C_{10}H_{16}$ has C atoms with three(one) C(H) neighbours and two(two) C(H) neighbours. Additionally, $C_{26}H_{32}$ and $C_{84}H_{64}$ have C atoms with all C nearest neighbours(nn). Exact match of ζ between all atoms of reference and target systems is thus impossible in these examples. Matching ζ and ξ will therefore be less effective in mapping from C_3H_8. Also, since there is only one C atom with two(two) C(H) neighbours in C_3H_8, matching ζ can be restrictive in terms the variety of orientations. We thus opt for matching structural parameters within a tolerance for ζ set to the minimum difference of ζ

values between similar type of atoms in reference and target systems to ensure maximal matching of ζ besides finer matching of structural parameters. As obvious, a better choice of reference system than C_3H_8 with C atoms having all varieties of neighbourhood can be easily made. However, we deliberately chose to test mapping from C_3H_8 which is the smallest possible reference system with just one C atom with two(two) C(H) neighbours, since such C atoms dominates the surfaces of the nano diamonds and are thereby expected to host the states at the edges of the valence and conduction bands. Surprisingly, as evident in Fig.4.13(c), with mapping of only the nn-hopping terms from C_3H_8 to $C_{10}H_{16}$, the mapped TB DOS already matches reasonable well with DFT DOS of $C_{10}H_{16}$ in terms of the band-gap and DOS around band edges. With increase in range of hopping to 2.7Å(nn,2n), 3Å(nn,2n,3n) and 4Å(2n,3n,4n)) for C-C, C-H and H-H pairs based on availability of one-to-one mapping[Fig.4.13(a,b)] the match of mapped TB DOS and DFT DOS[Fig.4.13(d)] extends deeper into the valence band. The quality of match improves further with additional mapping of C-H and H-H atom pairs up to 4.5Å [Fig.4.13(e)] without compromising on tolerance factors. Notably, the range of hopping of C-H and H-H, although are more than that of C-C, are actually consistent with the range of C-C hopping, since the farthest H atoms considered are associated with two second nearest C atoms. The same mapping parameters are then used to map self-energy corrected TB (SEC-TB) parameters of C_3H_8 to $C_{10}H_{16}$ leading to a good match of not only the SEC-TB mapped band-gap and the QP band-gap calculated at the G_0W_0 level, but also the SE corrected DOS of the valence band[Fig.4.13(f)].

Next we attempt mapping $C_{26}H_{32}$ from smaller references, starting with mapping from C_3H_8 to $C_{26}H_{32}$, which is about five times increase in system size.Mapping of only nearest neighbour C-C and C-H hopping underestimates band-gap by about 15%[Fig.4.14(c)]. Mapping all hopping parameters up to upto 4.5Å which is the maximum range of hopping available in the reference, drastically improves overall match of not only mapped TB DOS and DFT DOS[Fig.4.14(d,e)] but also mapped SEC-TB DOS and DFT+G_0W_0 DOS[Fig.4.14(f)], as is seen in case of mapping $C_{10}H_{16}$ from C_3H_8.
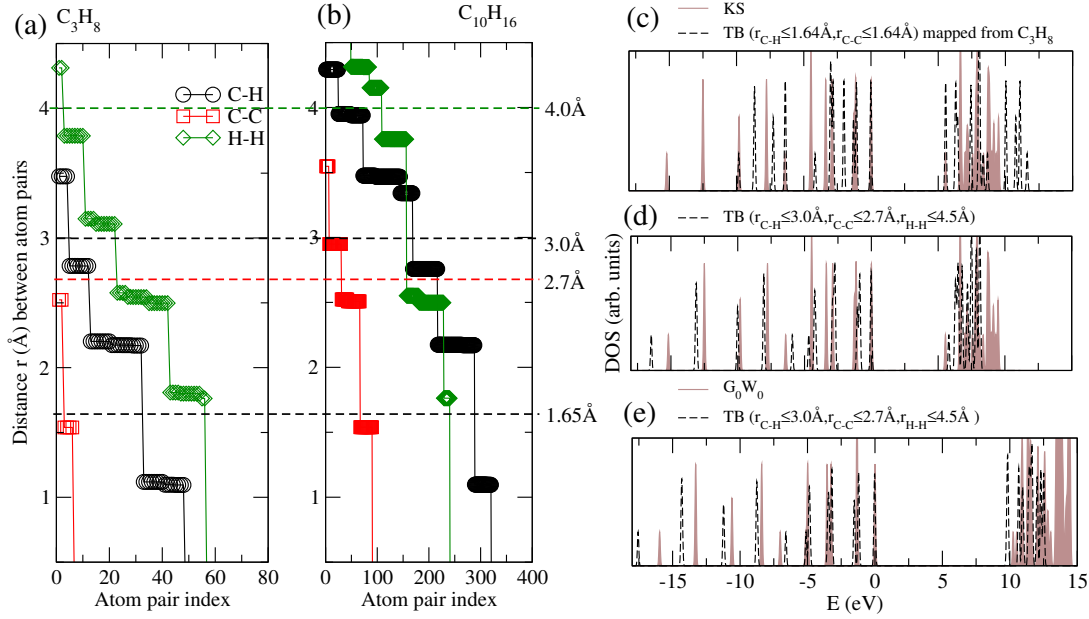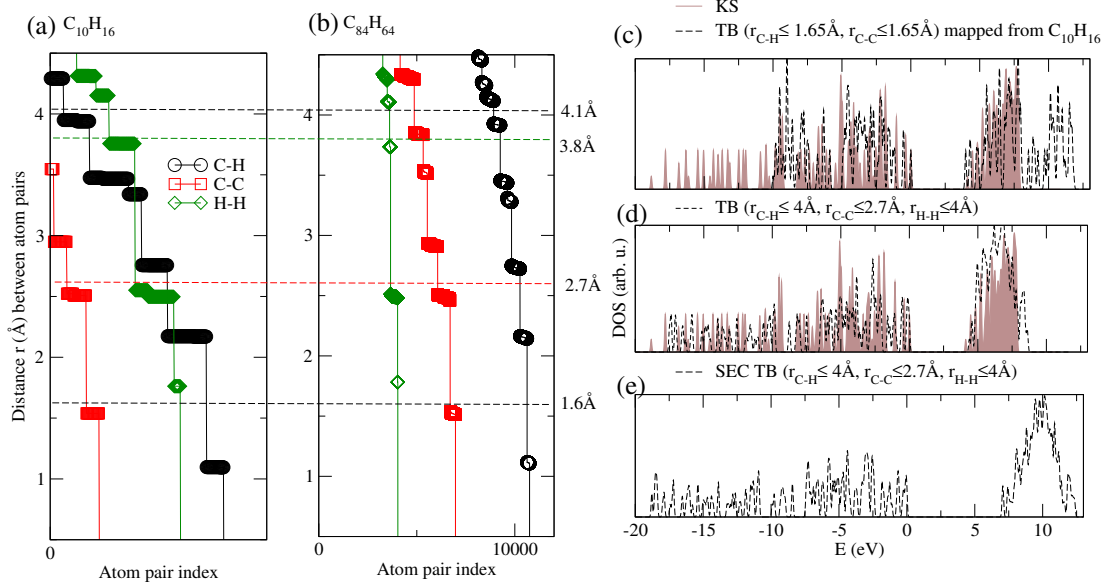
Figure 4.15: Distribution of distance between pairs of atoms in (a): reference ($C_{10}H_{16}$) and (b): target ($C_{84}H_{64}$) systems. (c-d): Match between DFT DOS and mapped TB DOS as with an increasing spatial range of neighbourhood considered for mapping. (e): Match between DFT+G_0W_0 DOS and mapped self-energy corrected TB DOS.

Finally we demonstrate mapping to $C_{84}H_{64}$ from $C_{10}H_{16}$, which is about six time enhancement in system size. Mapping of only the nearest neighbour C-C and C-H bonds results into good match of the mapped TB band-gap[Fig.4.15(c)] with the DFT band-gap. With further mapping of hopping parameters upto 2.75Å(nn,2n), 4Å (nn,2n+) and 4Å (2n,3n+)[Fig.4.15(a,b)] for C-C, C-H and H-H pairs, satisfactory match of the entire valence band and a good match[Fig.4.15(d)] of the band-gap is achieved. Mapping of SEC of TB parameters from $C_{10}H_{16}$ to $C_{84}H_{64}$ results into a QP band-gap of about 7.2 eV which is within 5% deviation from the QP band-gap implied in literature.[15,127,128,129]

In Fig.4.16 we show similar mapping of TB parameters at the DFT and DFT+G_0W_0 levels for Si based nano-diamonds. Like in case of nano-diamonds, mapping of hopping up to second nearest Si neighbours and H atoms associated with them from Si_3H_8, renders good match of the SEC-TB band-gap with the explicitly estimated DFT+G_0W_0 band-gap almost up to six times escalation of system size. These results imply consistency in transferability of SEC corrected TB parameters with increasing
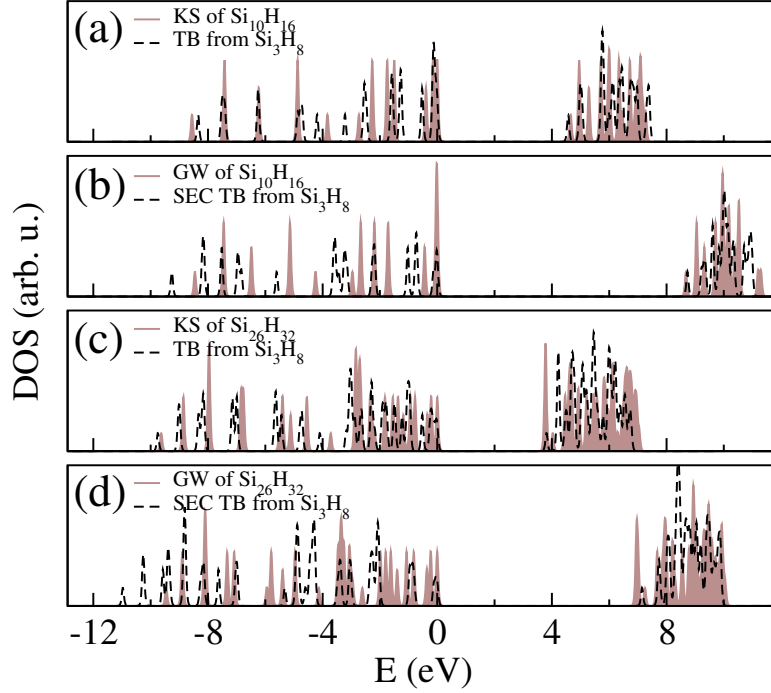
Figure 4.16: (a,c): Match between DFT DOS and TB DOS with parameters mapped from Si_3H_8. (b,d): Match between DFT+G_0W_0 DOS and SEC-TB DOS using mapped self-energy corrected TB parameters from Si_3H_8.

principal quantum number of valence orbitals.

4.3   Conclusion

In conclusion, construction of naturalized hybrid atomic orbitals(HAO) is proposed as the common eigen-states of the non-commuting set of finite first-moment matrices corresponding to the orthogonal directions. Hybridization and orientations of HAOs are numerically naturalized as per their anticipated immediate atomic neighbourhood. Choice of gauge based on the HAOs leads to the construction of the hybrid atomic Wannier orbitals (HAWO) from Kohn-Sham(KS) single particle states, rendering a multi-orbital orthonormal tight-binding(TB) basis locked to the nearest neighbourhood. HAWO basis allows calculation of single TB parameters per bond from first principles, and facilitate their easy transfer across iso-structural systems through mapping of immediate atomic neighbourhoods and projection of charge centres learned in the process of naturalization of the HAOs. The mapping

allow effective bottom-up transfer of self-energy corrected TB parameters estimated within the *GW* approximation of many-body perturbation theory in HAWO basis, from smaller reference systems to much larger target systems having similar covalent atomic neighbourhoods, suggesting a possible route towards computationally inexpensive estimation of quasi-particle structures of large covalent systems within acceptable range of accuracy, with extra computational cost scaling as N^2, beyond the explicit computation of self-energy correction for smaller reference systems which typically scale as N^4. Demonstrated in nano-ribbons and nano-diamond systems, the transferability of self-energy corrected multi-orbital TB parameters in HAWO basis, is rooted at the spatial localization of the extent of self-energy correction predominantly within the third nearest neighbourhood, which appears to be robust for σ bonds but lesser so with π bonds and unpaired electrons.

Chapter 5

Self-energy corrected tight binding parameters for few p-block semiconductors in the hybridized atomic orbital basis constructed from first principles

In this chapter we use our proposed methodologies to construct the self-energy corrected TB framework in the hybrid atomic Wannier orbital (HAWO) basis proposed in Chapter 4 to acces transferability of self-energy correction among the bulk structures as well as between bulk and finite structures made by elements within and across the $2p$, $3p$ and $4p$ blocks of the periodic table in group 13, 14 and 15.

5.1   Introduction

Starting with the advent of the quantum theory of solids,[130] tight-binding(TB) frameworks in the basis of spatially localized Wannier functions (WF),[12] have been

envisioned as a generic approach to compute electronic structure of materials. Slater-Koster (SK) parametrization[13,14] of elements of a TB Hamiltonian marked the beginning of reasonable band structure calculations of solids. With the advent of the Kohn-Sham(KS) density functional theory(DFT),[1,2] the mean field approximation of KS-DFT[56,57] and tight-binding parameters[46,131,132] determined by fitting the energy bands at the DFT level, have been the work horse for studies of ground states properties of materials with weak to modest localization of valence electrons for about three decades now.

With our increasing capability to fabricate devices with ever shrinking size - now well within double digits in nanometers, interest in accurate computation of physical and electronic structure of such systems, which typically consist of thousands of atoms, led to the evolution of tight-binding frameworks for finite systems with structural inhomogeneities. Efforts to derive TB parameters for large finite systems, particularly with sp^3hybridization of orbitals, have been reported not only in the orthogonal sp^3basis[133,134,135,136,137,138] but also more generalizably in the non-orthogonal basis as well[139,140,141] and used extensively in molecular dynamics simulation[136,142] and calculation of optical properties.[16,143,144,145,146] Evolution of computational techniques to construct spatially localized Wannier functions (WF),[47,48] opened up the scope for construction of realistic localized orbitals from KS single particle states,[147,148] leading to explicit computation of realistic TB parameters from first principles.

With improved spectroscopic measurements enhanced correlation due to spatial confinement near surfaces and interfaces of nano-structures became apparent which made it imperative to take the frameworks of computation of electronic structure beyond the mean field regime leading to formidable increase in computational complexity and cost. While much effort in this direction has been underway in terms of improving the exchange-correlation functionals[63] to include effects of many-electron interactions within the KS energy eigen-spectrum, the GW approximation[6] of the many body perturbation theory (MBPT)[4,5,122,123,124] is so far the most general abinitio framework to unmissably account for correlations starting from the KS single

particle states. However, both the approaches are computationally expensive and almost prohibitive for systems with thousands of atoms. These limitations have led to attempts to incorporate effects of correlations within the tight-binding(TB) frameworks. Efforts reported in recent years mostly improve TB parameters[71,72,73,74,126] by matching QP structure in specific systems and orbital subspaces.

In this work we calculate self-energy correction(SEC) to TB parameters from the SEC of the KS energy eigenstates at the DFT+G_0W_0 level. With tetrahedrally coordinated atoms exclusively considered in this work except the passivating H atoms at the surface of the nano-diamonds, TB parameters are calculated in the orthonormal basis of Wannier functions(WF) constructed following a realistic template of sp^3hybridized atomic orbitals(HAO) obtained from KS single particle states of isolated atoms. The resultant WFs resemble hybrid atomic orbitals and orient towards directions of coordination by construction, and thereby locked to the immediate neighbourhoods of atoms. The aim of this work is to present a comparative analysis of TB parameters and their SEC in such directed hybrid orbital basis beyond the nearest neighbourhood for bulk and finite structures made of a representative variety of $2p$, $3p$ and $4p$ block elements which exists in diamond or zinc-blend structures in three dimensions. We also demonstrate that such TB parameters can be transferred from smaller nano-diamonds to their much larger iso-structural counterparts exclusively through mapping of neighbourhoods typically up to 2nd or third nearest neighbours, to render HOMO-LUMO gaps of the larger systems in good agreement with their explicitly calculated values at the DFT and DFT+G_0W_0 level.

5.2   Methodological details

5.2.1   Construction of hybrid atomic orbitals(HAO) and their transfer to system of atoms

Hybrid orbital basis (HAO) are constructed for isolated atoms as the approximate eigenstates of the non-commuting set of three first moment matrices (FMM) X, Y
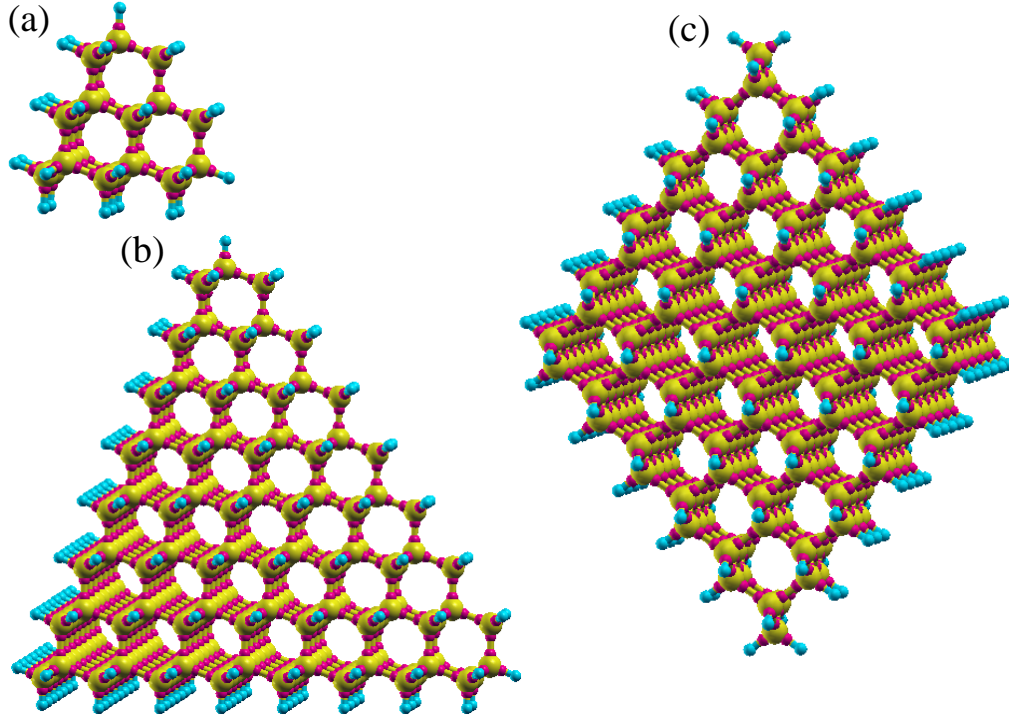
Figure 5.1: Nano-diamonds with projected charge centres of HAOs (pink spheres): (a) $C_{26}H_{32}$, (b) $C_{281}H_{172}$ and (c) $C_{322}H_{156}$. Charge centres of H coincides with H.

and Z projected in a finite subspace of orthonormal basis states. FMMs calculated as:

$$(X, Y, Z)_{ij} = \langle \phi_i \mid (x, y, z) \mid \phi_j \rangle. \qquad (5.1)$$

are maximally joint diagonalized using an iterative scheme based on the Jacobi method of matrix diagonalization where off-diagonal elements are minimized through rotation of coordinates by a specific analytic choice of angles as detailed in Chapter 3 HAOs are naturally oriented towards direction of coordinations around atom as per the set of basis states considered for construction of the HAOs. The charge centres of HAOs thus render coordination polyhedra around an atom for a given sub-shell. For construction of the sp^3HAOs used in this work, the lowest four KS states of a single atom are used as basis. Although in principle, any localized atomic orbitals like the pseudo-atomic orbitals or the Slater or Gaussian type orbitals parametrized for the given atoms can also be used for the purpose, it is important to have appropriate length-scale of localization of the HAOs for their correct representation within the
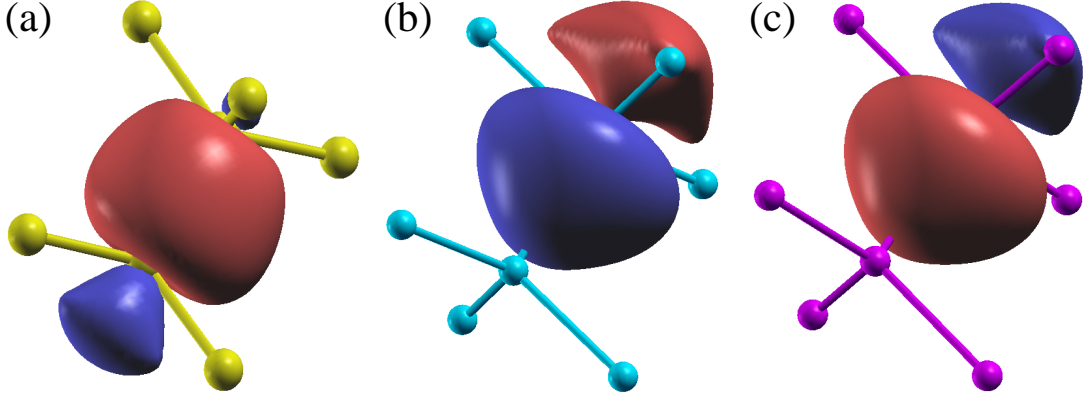
Figure 5.2: HAWOs in bulk (a)C (b)Si and (c)Ge.

KS states of the given system of atoms where the HAOs are to be used as template to construct WFs. Same pseudo-potential thus preferably be used for generation of HAOs and also for calculation of electronic structure of the given system.

Separate sets of HAOs are constructed for each types of atoms, and transfered to the corresponding atoms in the given system through mapping of directions of coordination from the atoms to their nearest neighbours on to the directions of charge centres of HAOs from the isolated atom for which they are explicitly constructed. Through such mapping a distribution of projected charge centres of HAOs are generated for the entire system prior to the transfer of HAOs, as seen in Fig.5.1. For perfect tetrahedral coordination, as seen in the bulk diamond and zinc blende structures, the transfered HAOs would thus retain intra-atomic orthonormality, whereas for the nano-diamonds such intra-atomic orthogonality will be marginally compromised owing to deviations of perfect tetrahedral coordination more towards the surface. However this is not a problem as such not only because the deviations are minimal but because all transfered HAOs are symmetrically orthonormalized during the construction of the WFs.

Orthonormalized Wannier functions from the KS states following the HAOs transferred from the isolated atoms are constructed as decribed in section-3.2 in Chapter 4. Representability of HAO ϕ_n within the set of KS states considered, is ensured by setting a cutoff on each individual $S_{\vec{k},n,n}$ values to be more than 0.85, which is found to be satisfied by the lower bound of the number of KS states as per
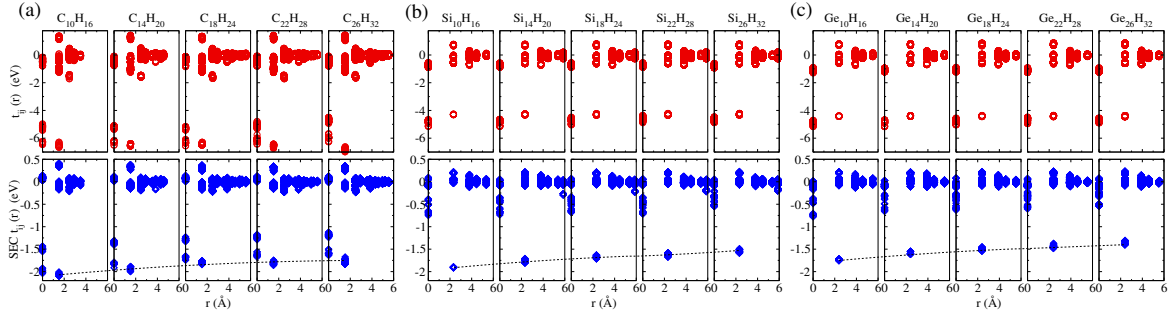
Figure 5.3: TB and self-energy correction to TB parameters in (a) carbon, (b) silicon and (c) germanium nano-diamonds from adamantane to pentamantane (black dashed curve for guide to the eye).

the total number of orbitals considered.

Using the Löwdin symmetric orthogonalization[76] a new set of orthonormal Bloch states from the KS single particle states are subsequently constructed as per Eqn.(3.2) to Eqn.(3.4). Finally, a localized set of orthonormal hybrid atomic Wannier orbitals (HAWO) similar to their corresponding HAOs are constructed as per Eqn.(3.5). TB parameters at the DFT level and DFT+G_0W_0 level are computed in the HAWO basis from energetics of KS single particle states and their self-energy correction as per Eqn.(3.6).

5.2.2 Bottom-up mapping of TB parameters

As already discussed in Chapter 4 the orientation of HAWOs being locked to the local atomic neighbourhood of each atom, the multi-orbital TB parameters derive in HAWO basis are easily mappable from one system to another with matching atomic neighbourhoods. Transferability of the TB parameters in terms of reproducibility of band-gaps and band-width within acceptable ranges of deviation from their direct estimates from first principles, is demonstrate by transferring TB parameters from smaller reference systems to structurally similar larger target systems. Transfer of TB parameters is done in two steps.

First all individual pairs of atoms of the target system beyond the nearest neighbourhood, are mapped on to matching pairs of atoms in the reference system through comparison of a collection of structural parameters like spatial separation, angles and
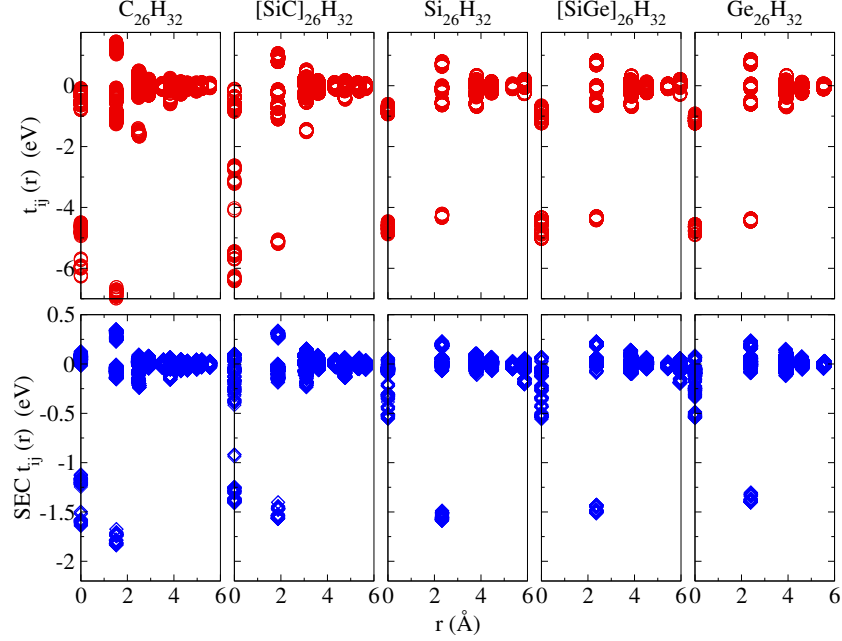
Figure 5.4: TB and self-energy correction to TB parameters of hybrid SiC and SiGe nano-diamonds(pentamantane) along with those of C, Si and Ge nano-diamonds(pentamantane).

dihedral angles subtended by the nearest neighbours and a measure (ζ) of proximity of atoms with respect to surfaces, interfaces and inhomogeneities defined as:

$$\zeta_i = \sum_{j}^{N_i} Z_j w(r_{i,j}) \tag{5.2}$$

N_i being the number of neighbours of the i-th atom within a chosen cutoff radius, and w being a weight factor which is a function of the distance $r_{i,j}$ of the j-th neighbour of the i-th atom, and Z_i being a characteristic number to be associated with each type of atom, for example, the atomic weight.

For mapping of orbital pairs from reference to target, a projected map [Fig.5.1(b-c)] of locations of charge centres of HAOs for the target system is generated first and then among the mapped pair of atoms, pair of HAOs of system are mapped to pair of HAOs of the reference through mapping of their respective charge centres much like the mapping of atom pairs. The weight factor w is typically chosen to be 1.0 within half of the cutoff radius and smoothly reduced to zero at the cutoff radius using a
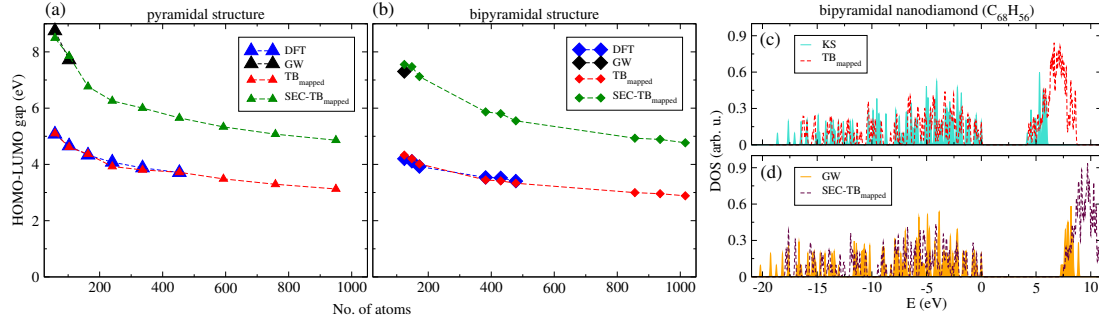
Figure 5.5: Variation of HOMO-LUMO gap computed with TB and SEC-TB parameters mapped to un-relaxed structures from relaxed pentamantane structure, and the same computed from first principles at the DFT and DFT+G_0W_0 level with relaxed structure, as function of size of carbon nano-diamonds increasing in (a) pyramidal and (b) bi-pyramidal structures. Comparison of DOS of $C_{68}H_{56}$ calculated from (c) TB mapped to un-relaxed structures and DFT of relaxed structure, and (d) SEC-TB mapped to un-relaxed structure and DFT+G_0W_0 of relaxed structure .

cosine function. Cutoff radius is chosen based on the size of the reference system, since it should neither be too large for variations in Z_i to average out, nor should it be too small such that ζ varies abruptly only at the structural inhomogeneities. Cutoff radius and Z_i values should thus be so chosen that ζ values can effectively differentiate between atoms at the interior of a finite system from those at the surfaces in both reference and target systems such that relaxed structures of target systems are not required to adequately transfer effects of variation in bond lengths near the surfaces from reference to target systems.

5.3 Computational details

All the ground state geometries as well as ground state electronic structures are calculated using the QUANTUM ESPRESSO (QE) code[77] which is a plane wave based implementation of density functional theory (DFT). BFGS scheme has been used to obtain the relaxed structures. For bulk systems variable cell relaxation has been performed to optimize lattice parameters and ionic positions. A separation of at least 10 Å between periodic images has been ensured for all the finite systems. The KS ground state properties are calculated within the Perdew-Zunger approximation
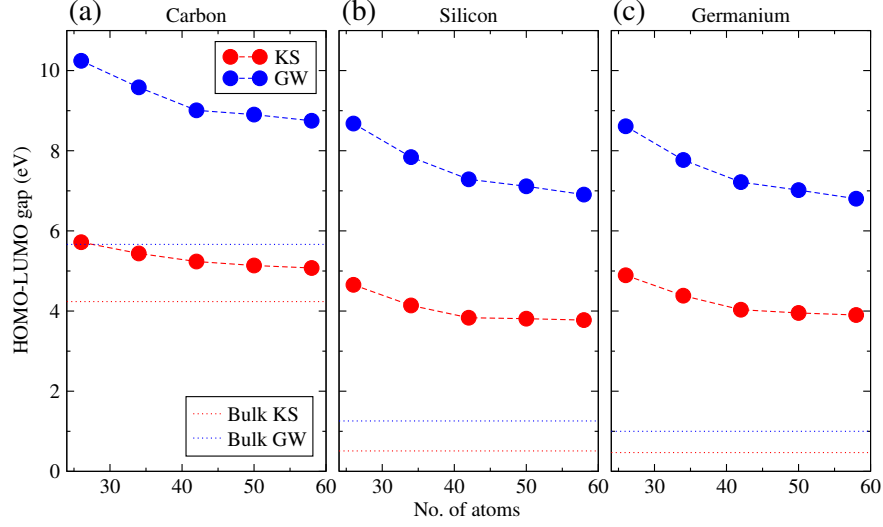
Figure 5.6: Variation of HOMO-LUMO gap of nanodiamonds from adamantane to pentamantane made of (a) carbon, (b) silicon and (c) germanium. Bulk band gaps are shown in dotted lines.

of the exchange-correlation functional implemented in a norm-conserving pseudo-potential. Plane wave basis with kinetic energy cutoff in excess of 60 Rydberg along with a 15x15x15 Monkhorst-Pack grid of k-points have been used for all the bulk systems. The self-energy correction to KS energy eigenvalues are calculated at the G_0W_0 level of GW approximation of the many-body perturbation theory (MBPT) implemented in the BerkeleyGW (BGW) code.[42] To calculate the static dielectric matrix and extend to the finite frequencies the generalized plasmon-pole model[6] is used. We have used a energy cutoff of 10 Rydberg for the dielectric matrix and Coulomb truncation is according to the systems dimension. For convergence of dielectric function as well as the self-energy term we used 250(5000) bands for bulks(nano-diamonds). To get a well converged band-gap for bulk structures we used a finner k-mesh of 30x30x30 grid through the interpolation based on the AWOs. Finally, in-house implementation interfaced with the QE code is used for generation of HAOs, HAWOs from KS states, calculation of TB parameters in the HAWO basis, and mapping of TB parameters from smaller reference systems to larger target systems.
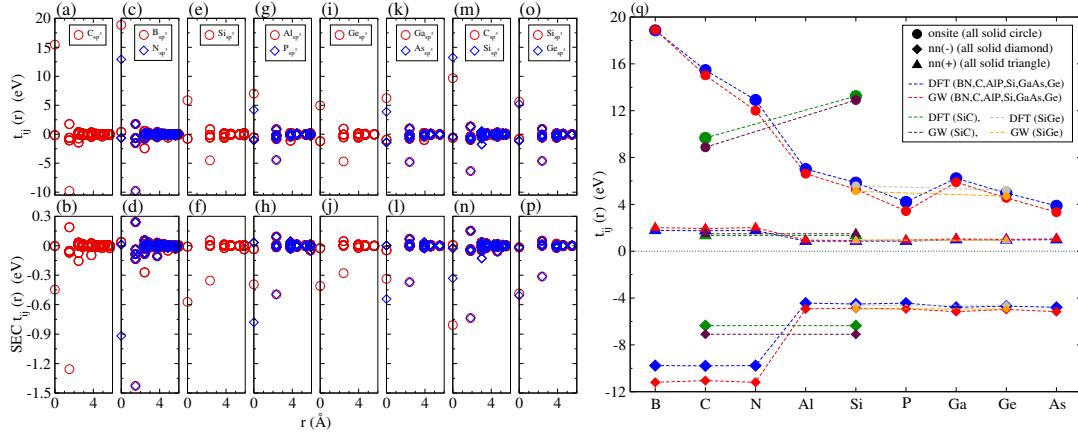
Figure 5.7: (a-p) TB parameters and their self-energy corrections, and (q) summary of onsite and dominant inter-atomic terms, for 2*p*, 3*p* and 4*p* block elements in diamond and zinc blende structures.

5.4 Results and discussion

Nano-diamonds starting with adamantane followed by diamantane, triamantane, tetramantane with increasing number of atoms up to pentamantane have been considered for explicit calculation of TB parameters at the DFT level and their further refinement due to SEC of KS energy eigenvalues at the G_0W_0 level. As evident in Fig.5.3 the dominant nearest neighbour(nn) TB parameters as well as those beyond the nearest neighbourhood, remains effectively invariant with respect to system size, implying transferability of TB parameters across length-scales of nano-diamonds at the DFT level as we demonstrate in this paper. Magnitudes of TB parameters in Si and Ge are similar but vary significantly from that of C, which is consistent with variation in their inter-atomic separations. Notably however, the SEC to the dominant TB parameters reduces slowly with increasing system size in a similar rate for C, Si and Ge based nano-diamonds, although the magnitude of correction itself reduces significantly with increasing principal quantum number owing to increased de-localization. The slow variation of SEC across system size also suggests possibility of SEC corrected TB parameters to be transferable as well to a workable degree.

Fig.5.4 clearly suggests that TB parameters of either Si or Ge can be used for
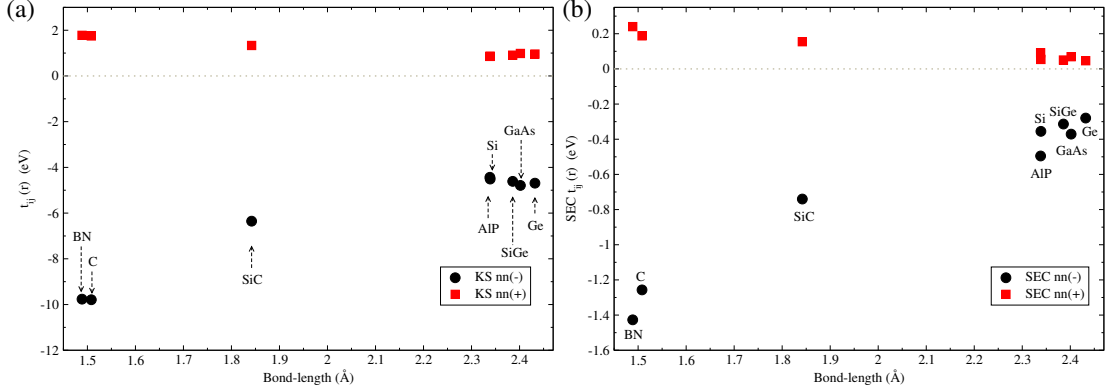
Figure 5.8: (a) TB and (b) Self-energy corrected nearest neighbor TB parameters (bonding and anti-bonding) for 2*p*, 3*p* and 4*p* block elements.

SiGe nano-diamond as well, whereas for the SiC nano-diamonds the dominant interatomic TB parameters are effectively the average of that of the C and Si based nano-diamonds. These observations hint at increased transferability of SEC across elements in a block with increasing quantum number of frontier orbitals. The reorganization of the on-site terms of SiC nano-diamond compared to those made of Si or C can be attributed to the hetero-polarity of the Si-C nn bond due to difference of electro-negativities of Si and C, whereas electro-negativities of Si and Ge are similar and less than that of C.

To study transferability of TB parameters from smaller nano-diamonds to their larger counterparts we have mapped TB parameters from pentamentane to larger pyramidal and bi-pyramidal carbon based nano-diamonds with close to 1000 atoms. We have considered un-relaxed coordinates of the larger nano-diamonds and mapped the TB parameters calculated for relaxed structure of pentamentane, using ζ values calculated with a cutoff radius considered up to the next nearest neighbour. As evident in Fig.5.5(a,b), the match of the DFT HOMO-LUMO gap with that calculated from the transferred TB parameters from pentamentane is found to be quite exact for both pyramidal as well as bi-pyramidal nano-diamonds up to about 500 atoms, which is almost about ten times escalation of size of the target system compared to that of the reference system. Notably, for all the larger nano-diamonds the DFT HOMO-LUMO gaps were calculated explicitly with well relaxed structures, whereas
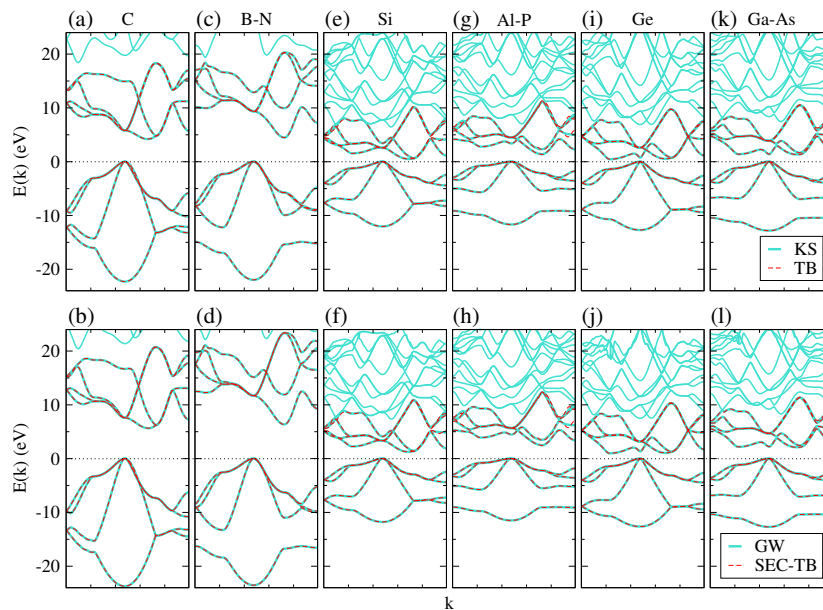
Figure 5.9: Comparison of band-structures computed from first principles with that obtained with TB parameters derived from first principles at the DFT (upper panel) and DFT+G_0W_0(lower panel) levels for $2p$, $3p$ and $4p$ block elements.

the structures used to transfer TB parameters from pentamentane were completely un-relaxed. Therefore the match of the exact DFT HOMO-LUMO gaps with that evaluated with TB parameters transferred to an un-relaxed structure point to the efficacy of ζ in differentiating atoms as per their proximity to the surface in both reference and target systems so that the transferred TB parameters have the correct variation from surface to interior. The match of the quasi-particle (QP) HOMO-LUMO gap is also found quite satisfactory up to more than two time escalation of system size beyond pentamentane, till which G_0W_0 calculations could be reliably performed with computational facilities at our end. QP HOMO-LUMO gap data available in the literature[15,127,128,129] allows us to compare for a bit further. These results thus confirms transferability of TB parameters with and without SEC over substantial escalation of system size.

Interatomic TB parameters for bulk Si and Ge in diamond structures are consistent with those in nano-diamonds notwithstanding the substantial drop of band-gap in bulk to about 0.5 eV(1 eV) from HOMO-LUMO gap around 4 eV(7 eV) in nano-diamonds at the DFT(DFT+G_0W_0) level as shown in Fig.5.6(b,c). However for

bulk C in diamond structure the dominant nn hopping term strengthens substantially to -10 eV (Fig.5.7(a)) from -6.5 eV (Fig.5.3(a) red plots) in nano-diamonds, although the band-gap in bulk is comparable to that of HOMO-LUMO gap of nano-diamonds, which are about 4.2 eV and 5 eV respectively at the DFT level. The reason of this contrasting trend for C compared to those for Si and Ge can be traced to one obvious fact that sp^3HAWOs in Si and Ge are more de-localized than that of C owing to increase in principal quantum number, but in addition to that, the C-C nn separation clearly decreases in bulk from nano-diamonds by about 2% to 3 %, as has also been reported[149] earlier, whereas the Si-Si and Ge-Ge nn separations remain largely same in bulk and nano-diamonds. Furthermore, as evident in Fig.5.2, the major lobe (positive one in this case) of the sp^3HAWOs of C is stretched towards the nearest C compared to the HAWOs of Si and Ge. Overlap of such sp^3HAWOs of C would thus increase appreciably with reduction in C-C nn separation from nano-diamonds to bulk, leading to the increase in magnitude of nn hopping term. Thus the TB parameters are not transferable from bulk to nano-diamond for C even at the DFT level. However it may still be feasible for Si and Ge.

Consistent with the localized nature of HAWOs, SEC is higher for C based bulk and nano-diamonds compared to their Si and Ge based counterparts. However the relative variation of localization of HAWOs of C, Si and Ge are much dominated over by the localization imposed by the finiteness of nano-diamonds, leading to comparable values of SEC of band-gap of C, Si and Ge based nano-diamonds ranging from about 4 eV to 3 eV leading to comparable SEC correction to nn hopping term ranging from -1.75 eV to -1.3 eV. From nano-diamonds to bulk the SEC to band gap and thereby to the nn hopping term reduces consistently on account of de-localization. Thus the self-energy corrected TB parameters are not transferable from bulk to nano-diamonds even for Si and Ge.

As evident in Fig.5.7(a,c,e,g,i,k), the nn hopping parameter is almost exactly same for diamond structures of group 14 (C,Si,Ge) and zinc blende structures made of groups 13 and 15 (BN,AlP,GaAs) within each block, whereas the SEC to the nn (Fig.5.7(b,d,f,h,j,l)) hopping are consistently more for zinc blend structures than the

diamond structures in each block owing likely to the enhanced localization of the bonding orbitals in the heteropolar B-N, Al-P and Ga-As nn bonds than in the C-C, Si-Si, and Ge-Ge bonds. Fig.5.7(q) summarizes the variation of the onsite terms and the major inter-atomic hopping parameters at the DFT and DFT+G_0W_0 level. As evident in Fig.5.7(m,o,n,p,q), for zinc blend structure of SiC(SiGe) the nn hopping and it's SEC both are average of their counterparts in diamond structures of Si and C(Ge). Fig.5.7(q) clearly suggests the stepped evolution of TB parameters and SEC from $2p$ to $3p$ and $4p$ blocks and the similarity in the later two. In Fig.5.8(a) and (b) we ploted the dominant TB parameters(t) and their self-energy correction(Δt) respectively. Fig.5.8 shows a slow but systematic reduction of both t and Δt as a function of bond-length which can be particularly useful in determining self-energy correction to bulk covalent systems with sp^3 hybridized orbitals. Band structures obtained with TB parameters shown in Fig.5.9 are plotted along with DFT band structure. Notably, for the exact reproduction of band structure the TB parameters have to be obtained not only in a dense enough grid of $\vec{k}$ but also using a KS band subspace of size exactly same as the number of HAOs transfered for the entire unit-cell in order to maintain the unitary nature of the matrix ($OS^{-\frac{1}{2}}$). If we use a larger KS subspace then the reproduction energy bands will become increasingly inexact with increasing energy.

5.5   Conclusions

For a representative variety of p block elements, we have presented TB parameters calculated at the level of DFT and DFT+G_0W_0 in the orthonormal hybridized atomic Wannier orbitals(HAWO) basis constituted of the KS single particles and are directed towards coordination by construction. We present TB parameters for nano-diamonds made of C, Si, Ge, SiC and SiGe and their bulks in diamond or zinc blende structures, and also of bulk BN, AlP and GaAs in the three consecutive p blocks. Transferability of inter-atomic TB parameters between bulk structures to nano-diamonds is generally poor and worsens with self-energy correction(SEC). However

among nano-diamonds, the inter-atomic TB parameters at the DFT level are found to remains effectively unaltered with increasing size, implying robust transferability of the TB parameters from smaller to larger nano-diamonds as demonstrated. Slow reduction of SEC to TB parameters with increasing system size also implies good transferability of self-energy corrected TB parameters across nano-diamonds. Transfer of TB parameters are performed exclusively by mapping up to second or third nearest neighbourhoods between the reference and the target systems, and thus does not necessitates relaxed geometries of the target systems as long as all neighbourhoods could be mapped. Similarity of TB parameters and their self-energy corrections across $3p$ and $4p$ blocks compared to that in the $2p$ block hints at the possible transferability of SEC across blocks with increasing principal quantum number.

Chapter 6

Planar heterostructure of BC and CN embedded in graphene and hexagonal BN for super-capacitor electrode applications

In this chapter we describe our effort to propose new materials for electrodes of capacitors partly as an application of the tight-binding framework in the basis of the hybrid atomic Wannier orbitals and their bottom up transfer described in Chapters 3 and 4.

6.1   Introduction

Developing new materials for efficient and inexpensive energy storage devices[150] has become a key direction of research in the materials science community. While the primary focus is still on batteries, a significant amount of interest has shifted in recent years to supercapacitors as well, owing to their quick charging, long life cycle and good reversibility[151,152,153,154,155] .But supercapacitors lag behind the conven-

tional batteries in terms of energy density which restrain their applications in contemporary power infrastructures,[156] leading to increased efforts towards improving their capacitance value[156,157]

Two dimensional graphene and graphene based materials have received much attention as supercapacitor electrodes due to their robust yet light weight structure, high specific surface area and good electrical conductivity[158,159,160,161,162,163,164,165] However, the specific capacitance of graphene based materials is low compared to popular capacitor electrodes due to low density of states near the Fermi energy rooted at the semi-metallic nature of graphene[166,167,168,169,170,171,172] . Much effort has been undertaken in last few years towards improvement of the specific capacitance for graphene based materials through chemical functionalizations, adsorption of metal atoms, creation of vacancies, dopings and tailoring of shapes and sizes of segments[166,173,174,175,176,177] .While these results suggests that it is possible to induce appreciable capacitance at low bias through appropriate micro-engineering of layered assemblies of $2p$-block elements, it is imperative to build on these results new proposals for robust layered structures made of p-block elements which can be synthesised at a large scale for mass use.

As a possible candidates, in this work we consider super-cells of planar two dimensional hybrid structures of graphene and hexagonal boron nitride, boron-carbide and carbon-nitride. From the computational point of view, the key challenge in exploring new materials for electrodes, is to get the DOS near the Fermi energy realistically correct. First principles calculations performed at the density functional theory (DFT) level are known to underestimate band-gap and can potentially lead to wrong prediction unless the overlap of the valence and conduction bands are substantial. We therefore performed first principle calculations to estimate the quantum capacitance both at the DFT level as well as at the G_0W_0 level of the GW approximation of self-energy correction beyond DFT, using the transfer of self-energy corrected TB parameters described in Chapters 3, 4 and 5.
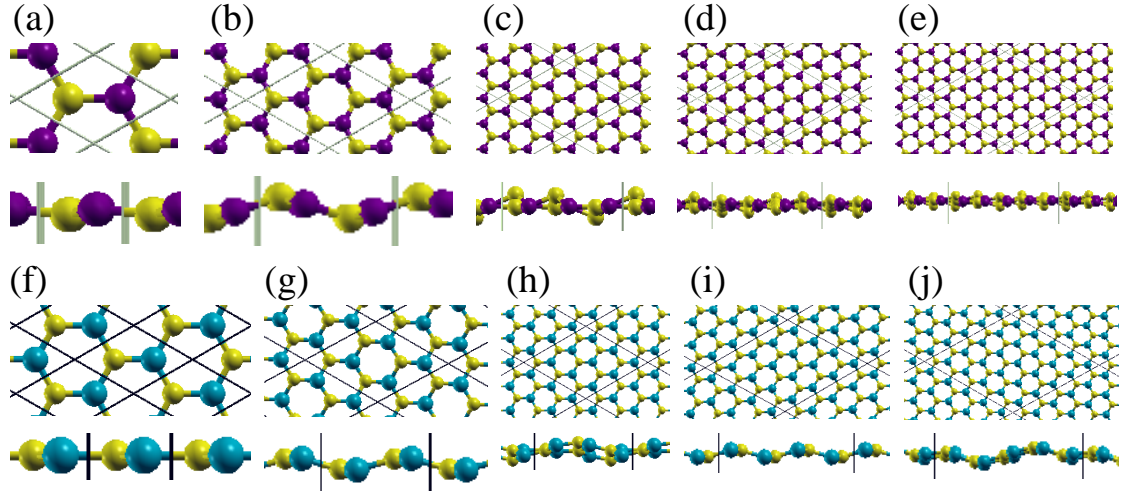
Figure 6.1: Variable cell relaxed structures of carbon-nitride (a) 1x1, (b) 2x2, (c) 3x3, (d) 4x4 and (e) 5x5 supercells. Boron-carbide variable cell relaxed structures (f) 1x1, (g) 2x2, (h) 3x3, (i) 4x4 and (j) 5x5 supercells.

6.2   Quantum Capacitance

In a generic capacitor there are primarily two types of capacitive contributions, one from the electrodes themselves and the other is from the electric double layers (EDL) which are the layers of electrolyte with induced charges adjacent to the electrodes. With these two contributions in series the total capacitance is found as:

$$\frac{1}{C_{tot}} = \frac{1}{C_Q} + \frac{1}{C_{EDL}} \tag{6.1}$$

where C_Q is the capacitance of the electrode and C_{EDL} is that of the electric double-layer. In our work we focus on possibilities of improving C_Q of layered network of three coordinated boron, carbon and nitrogen.

The capacitance C_Q is essentially the quantum capacitance, also known as the chemical capacitance, which is defined as the ratio of the variation of charge density dq due to variation in applied potential dV_G, as:

$$C_Q = \frac{\delta q}{\delta V_G}. \tag{6.2}$$
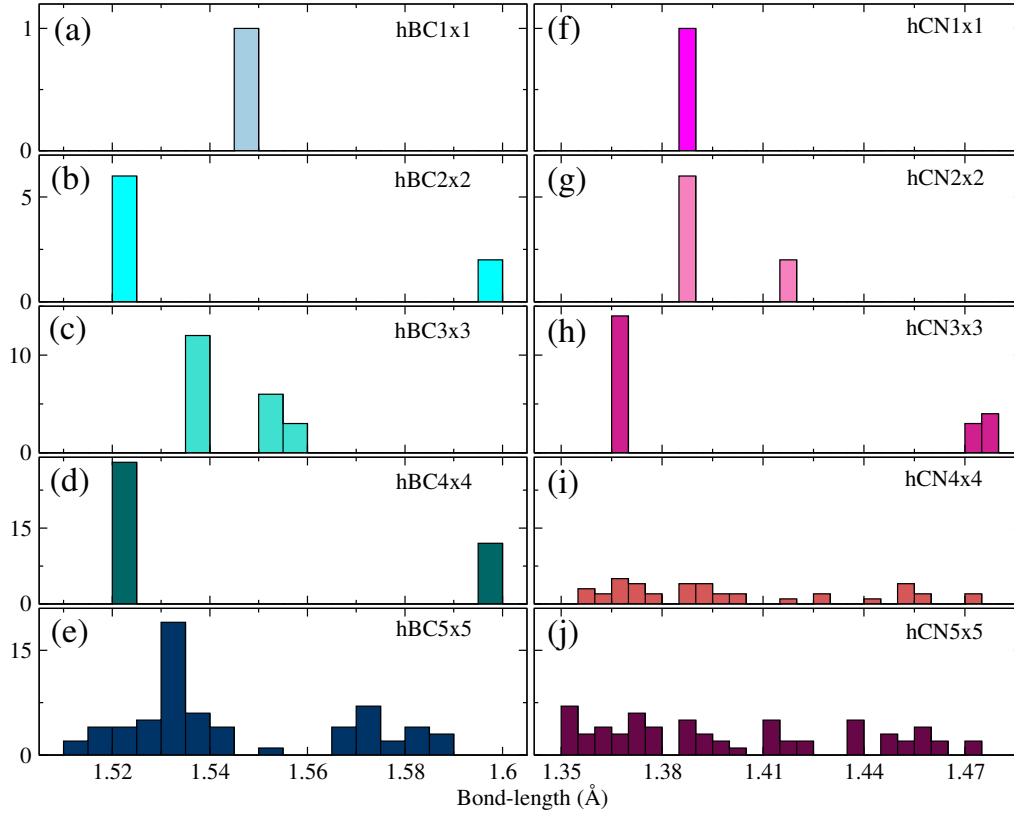
Figure 6.2: Bond-lengths distribution of hBC and hCN systems of VC relaxed structures from 1x1 to 5x5.

where "G" stands for gate implying V_G to be an applied gate bias. Number of electrons at the electrode at bias V_G can be computed as:

$$q_0 = (-e) \int_{-\infty}^{\infty} D(E) f(E, \mu(T) - eV_G) dE. \tag{6.3}$$

where $D(E)$ is the density of states (DOS) of the electrode and $f(E, \mu(T))$ is the Fermi-Dirac distribution function:

$$f(E, \mu(T)) = \frac{1}{e^{(E-\mu(T))/k_B T} + 1} \tag{6.4}$$

corresponding to chemical potential $\mu(T)$ at a given temperature T.

Change in number electron due to change in bias by δV_G can therefore be calculated as:

$$\delta q = (-e) \int_{-\infty}^{\infty} D(E)[f(E, \mu(T) - e(V_G + \delta V_G)) - f(E, \mu(T) - eV_G)]dE \quad (6.5)$$

which yields quantum capacitance C_Q, as:

$$C_Q = \frac{\delta q}{\delta V_G} = e^2 \int_{-\infty}^{\infty} D(E) \frac{\partial f(E, T, \mu)}{\partial \mu} \big|_{\mu = \mu(T) - eV_G} dE \quad (6.6)$$

where:

$$\frac{\partial f(E, T, \mu)}{\partial \mu} = \frac{1}{4k_B T} \text{Sech}^2 \left(\frac{E - \mu}{2k_B T} \right) = F_T(E - \mu) \quad (6.7)$$

$F_T(E - E_0)$ being the thermal broadening function peaked at E_0.

More generally therefore we have:

$$C_Q(V_G, T) = e^2 \int_{-\infty}^{\infty} D(E) F_T(E - \mu(T) + eV_G)dE \quad (6.8)$$

6.3 Computational Details

Density functional theory (DFT)[1,2] is used to calculate all the ground state electronic properties along with the ground state geometry optimizations. All the DFT based calculations are carried out using the QUANTUM ESPRESSO (QE) package[77] which is a plane wave based implementation of DFT. All the structures presented in this work are well optimized with the variable cell(VC) relaxation which optimizes the lattice parameters as well as ionic positions using the BFGS scheme. A separation of at least 10 Å vaccum is used between periodic images of planar structures. We used LDA as well as GGA pseudo-potentials implemented using the Perdew-Zunger (PZ)[56] and the Perdew−Burke−Ernzerhof (PBE)[57] approximations of the exchange-correlation functional respectively for optimization of structures. To calculate the DFT ground state properties we used primarily the Perdew-Zunger (PZ) approximation of the exchange-correlation functional implementation in a norm-conserving pseudo-potential. A plane wave basis with kinetic energy cutoff of 80 Rydberg is used for all the calculations. We used 64x64, 32x32, 21x21,
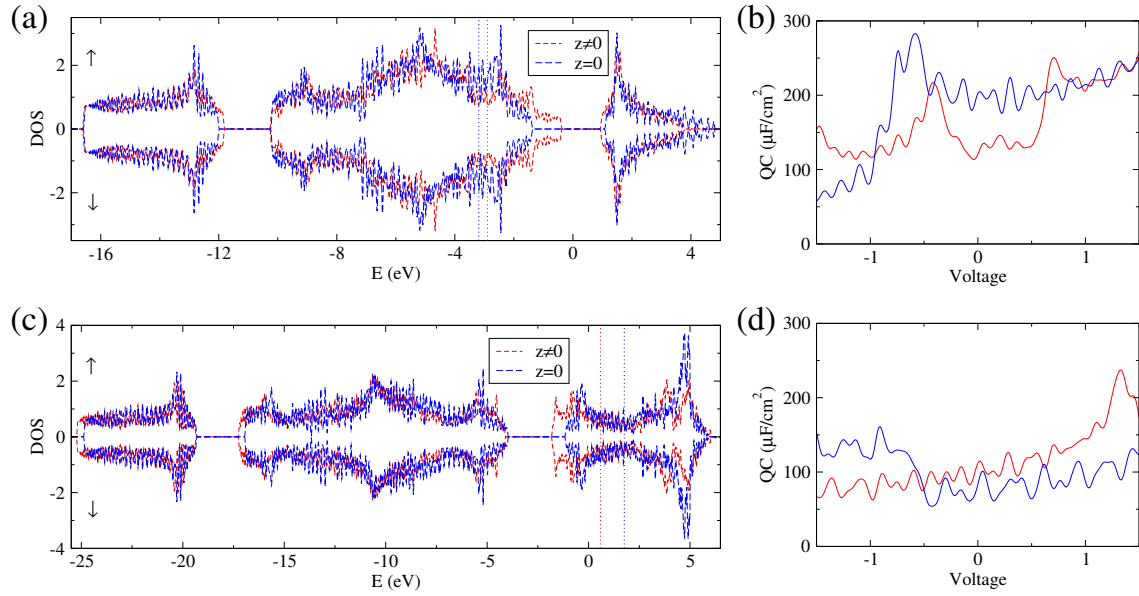
Figure 6.3: Density of states (DOS) of $z \neq 0$ and $z = 0$ of 2x2 (a) hBC supercell
with corresponding (b) quantum capacitance and (c) DOS of $z \neq 0$ and $z = 0$ of 2x2
hCN supercell with corresponding (d) quantum capacitance. Vertical dotted lines
in the DOS plots represent the Fermi level.

16x16... Monkhorst-Pack grid of k-points for 1x1, 2x2, 3x3, 4x4... two dimensional
super-cells.

For large planar unit-cells we have used our in-house implementation based on
methods introduced in Chapter 3 to transfer tight-binding parameters from smaller
reference systems where they are calculated in the basis of the hybrid atomic Wan-
nier orbitals introduced in Chapter 4. It is known that Wannierization fails in metals
in general due to truncation and entanglement of bands at the Fermi level, leading
to lack of localization. However in our work we construct Wannier function over
a larger subspace, which is typically double of that of the occupied subspace, and
includes both the bonding and the anti-bonding subspaces, in order to construct
Wannier function counterparts of atomic orbitals with intra-atomic hybridization.
Thus the problem of truncation and entanglement of bands does persist in gen-
eral at the edge of the subspace considered. However in all the covalent systems
considered in my thesis, the near complete (more than 90%) representation of the
template of hybrid orbitals within the subspace of Kohn-Sham states considered,
appears to ensure substantial localization of the resultant orbitals. leading to al-

most exact reproduction of the DFT band-structure and density of states by the tight-binding Hamiltoian derived from the resultant orbtials. We therefore have not considered implementing any disentanglement or down-folding procedure so far in our work, although it is true that such an implementation may further improve the localization of the Wannierized orbitals, which may further improve transferrability. Self-energy corrected TB parameters are obtained from self-energy correction of the KS single particle levels calculated using the BerkeleyGW (BGW) code[42] which is a implementation of the GW approximation[4,5,6,41] of the many-body perturbation theory (MBPT).[122,123,124] We calculate the quasi-particle electronic properties only upto the G_0W_0 level which is a one shot GW approximation. To calculate the static dielectric matrix and extend to the finite frequencies the generalized plasmon-pole model[6] is used. To calculate the screened Coulomb interaction a kinetic energy cut-off of 60 Rydberg is used for all the reference systems. For convergence of dielectric function and the self-energy operator we used in excess of 1200 bands.

6.4   Results and Discussions

Pristine graphene being a semi-metal, the DOS around the Fermi level is low, leading to weak quantum capacitance at low bias voltages. High DOS near Fermi energy is a result of localization of unpaired electrons. Electrons in graphene based materials can be localized either by hindering π-conjugation of $2p_z$ electrons which can happen at an edge, vacancy or substitution by an atom which does not have or can not spare a p_z electron to form π bonds with those of the neighbouring C atoms which thus tends to localize.

Structurally similar hexagonal boron nitride(hBN) is wide band-gap semiconductor owing to the large electronegativity difference of B and N, N being more electronegative due to higher nuclear charge. Due to the same reason, substituting an N(B) atoms by a C atom renders DOS of unpaired $2p_z$ electrons within the band-gap but near valence(conduction) band edge[178,179] , leading to reduction band-gap with increasing concentration of C atoms[178,180,181,182] . In fact, it is simple to
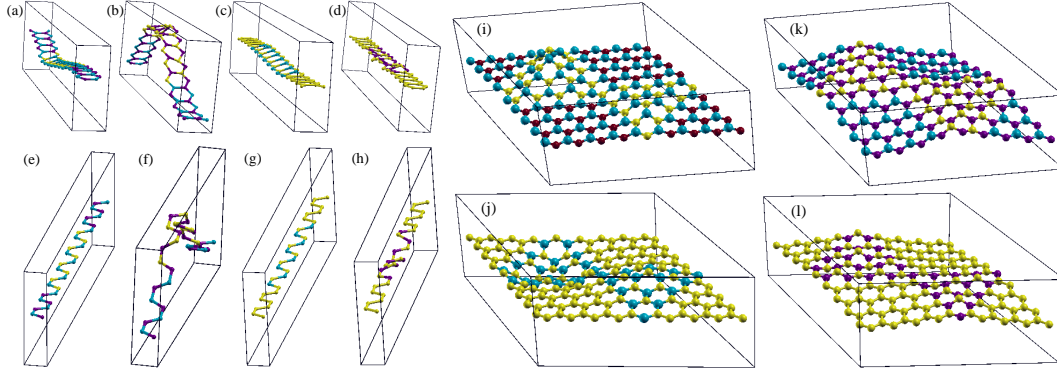
Figure 6.4: Supercells of AC interfaced (a) hBN-hBC, (b) hBN-hCN, (c) Gr-hBC
and (d) Gr-hCN. ZZ interfaced supercells (e) hBN-hBC, (f) hBN-hCN, (g) Gr-hBC
and (h) Gr-hCN. Interconnected triangular (i) hBN-hBC, (j) Gr-hBC, (k) hBN-hCN
and (l) Gr-hCN supercells.
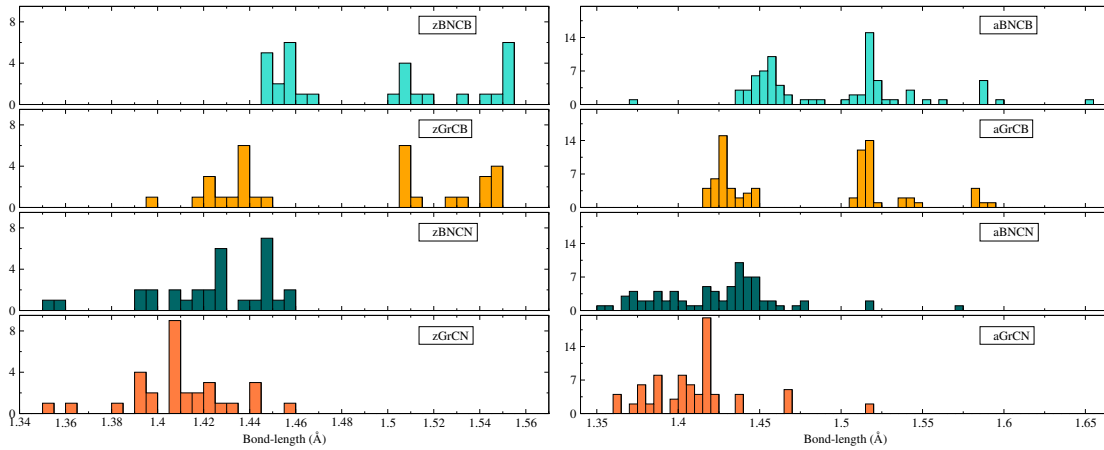
Figure 6.5: Bond-lengths distribution of armchair (left panels) and zigzag (right
panels) interfaced hetero-structures.

understand that with increasing substitution by C at B(N) sites the DOS peak of
the $2p_z$ electrons of C near the conduction(valence) band edge of hBN will broaden
with the Fermi level located in the middle of the broadened DOS peaks. Finally,
with substitution of all B(N) in hBN the broadened DOS peaks of the $2p_z$ electrons
of C merges with the conduction(valence) bands of hBN, thus rendering both as
metals. Understandably thus, planer unit-cells of hexagonal boron-carbide(hBC)
and carbon-nitride(hCN) are both metallic, and should in principle be ideal for elec-
trodes. However, planar structure of neither hCB nor hCN are stable, which at the
outset can be ascribed to the lack of sub-shell filling of C atoms in both the systems.
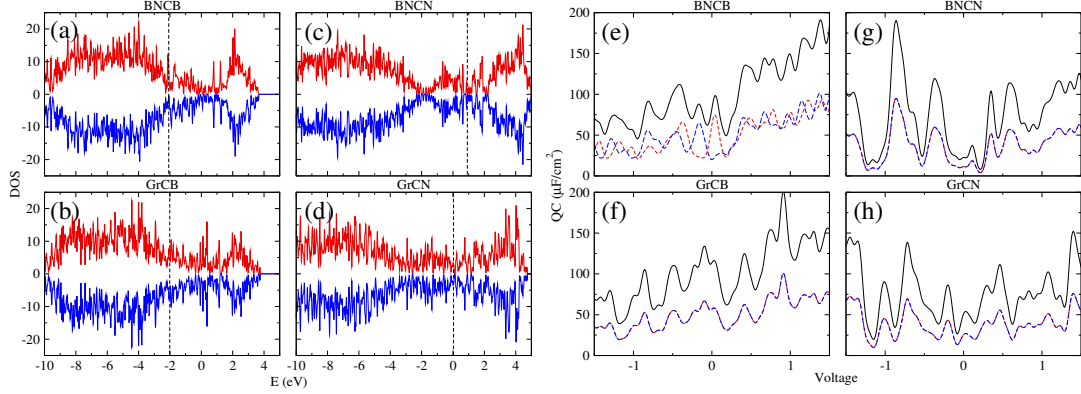
Figure 6.6: DOS of AC interfaced structures (a) hBN-hBC (b) Gr-hBC, (c) hBN-hCN and (d) Gr-hCN. (e), (f), (g) and (h) quantum capacitance of the corresponding systems respectively. Vertical dotted lines in the DOS plots represent the Fermi level.

Instability should be more in hCN, since in attempt to complete sub-shell filling of C atoms using lone pair of N atoms, the sub-shell of N atoms will tend to become overcomplete. On the other hand in hBC, B atoms have no spare electron using which the C atoms could attempt to complete their sub-shell filling.

We have performed VC optimization in two modes: (1) unrestricted VC where we giving freedom to move in all the components of coordinates which we will call as $z \neq 0$, and (2) restricted VC where we fix $z = 0$ for structures where we freeze the Z-component. In Fig.6.1(a-e) we show unrestricted VC relaxed structures of hCN with forces on atoms below 10^{-5} Ry/Bohr in 1x1 to 5x5 supercells. Distribution of bond-lengths in the corresponding 1x1 to 5x5 supercell is shown in Fig.6.2(f-j). Both the figures clearly suggest inherent structural instability in hCN which will grow further with size of super-cell considered. Similarly Fig.6.1(f-j) and Fig6.2(a-e) for hBC suggests structural instability, although of lesser degree than the hCN, which is evident from the fact that unlike in case of hCN the bond-length distribution in case of hBC tends to separate out in two groups of narrower width hinting at a somewhat systematic distortion. In fact, a recent report[183,184] claims planar structure of hBC to be stable based on only the two atom unitcell, which is indeed planar, but as we just discussed, does not represent the actual scenario. Our results thus indicate that hBC and hCN do not have planar stable structures, and stresses the need to look for reproducibility of structural stability of supercells to allow detection of unstable
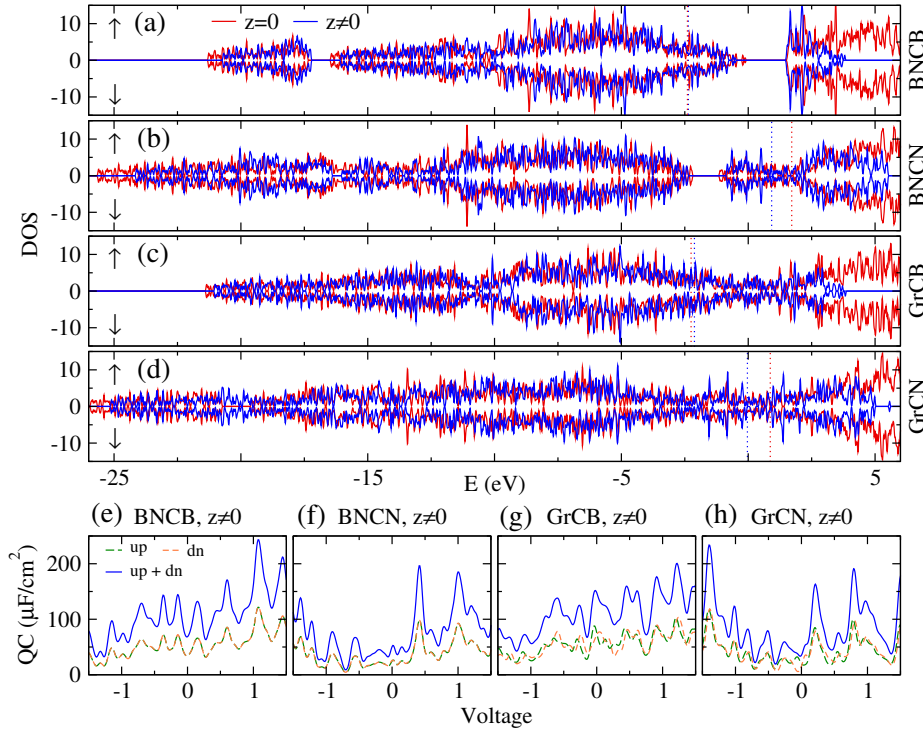
Figure 6.7: DOS of ZZ interfaced hetero-structures with both $z \neq 0$ and $z = 0$ configurations (a) hBN-hBC, (b) hBN-hCN, (c) Gr-hBC and (d) Gr-hCN and quantum capacitance of $z \neq 0$ (e) hBN-hBC, (f) hBN-hCN, (g) Gr-hBC and (h) Gr-hCN hetero-structures. Vertical dotted lines in the DOS plots represent the Fermi level.

equilibriums, as also can be done through calculation of phonon modes for smaller unit-cells.

In Fig.6.3(a) we show the DOS of 2x2 hBC supercell optimised with unrestricted and restricted VC relaxation using LDA pseudo-potentials. As argued above we find hBC to be metallic with a gap within the conduction band. We next plot quantum capacitance as a function of V_G in Fig.6.3(b), implying reasonably high values. Like hBC, hCN is also metallic [Fig.6.3(c)] as argued above but with a gap within the valence band. In Fig.6.3(d) we ploted the quantum capacitance which has relatively low value comparision to hCB. However as discussed above, hBC and hCN unit-cells with equal number of B(or N) and C atoms, do not have stable planar structure.

Aiming at enforcing planarity, we considered hBC and hCN segments embedded in graphene and hBN. We consider two geometries: (1) Gr/hBN - hBC/hCN parallel stripes, and (2) triangular islands of hBC/hCN embedded in Gr/hBN, as shown in
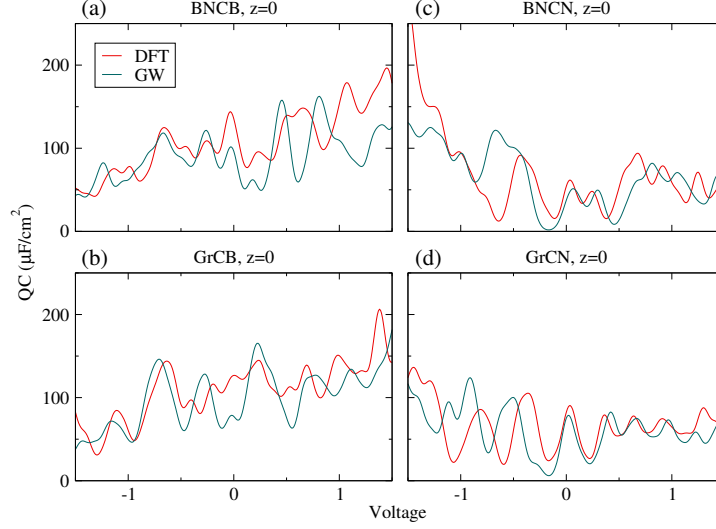
Figure 6.8: DFT and G_0W_0 quantum capacitance of planar $z = 0$ configurations of ZZ interfaced (a) hBN-hBC, (b) Gr-hBC, (c) hBN-hCN and (d) Gr-hCN heterostructures.

Fig.6.4(a-h) and Fig.6.4(i-l) respectively.

In type 1, we consider armchair(AC) [Fig.6.4(a-d)] and zigzag (ZZ) [Fig.6.4(e-h)] interface between the two regions. We find that stripes with hBC/hBN embedded in Gr tends to be more planar than those embedded in hBN. This is likely due to more effective accommodation of strain propagated from the hCB/hCN regions by Gr than by a more rigid hBN, as evident in the narrower distribution of bond-length for Gr/hBN-hBC in Fig.6.5. In particular, Gr-hBC as well as hBN-hBC are almost completely planar with ZZ interface, as shown in Fig.6.4(e,g). The bond-length distribution in these two stripes mentioned in Fig.6.5 marked as zBNCB and zGrCB suggest possibility of stable planar structure.

We calculated DOS [Fig.6.6(a-d)] and quantum capacitance [Fig.6.6(e-h)] for all AC interfaced systems and found that hBC embedded systems have higher capacitance value than hCN embedded systems. Additionally we also found that the hBN-hCB system is magnetic with AC interface, as can be seen clearly from the spin separation of capacitance across Fermi energy in Fig.6.6(e). Next in Fig.6.7(a-d) we calculate DOS for ZZ interfaced stripes for both $z \neq 0$ as well as $z = 0$ configurations and expectedly find them similar owing to inherent planarity of the stripes with ZZ
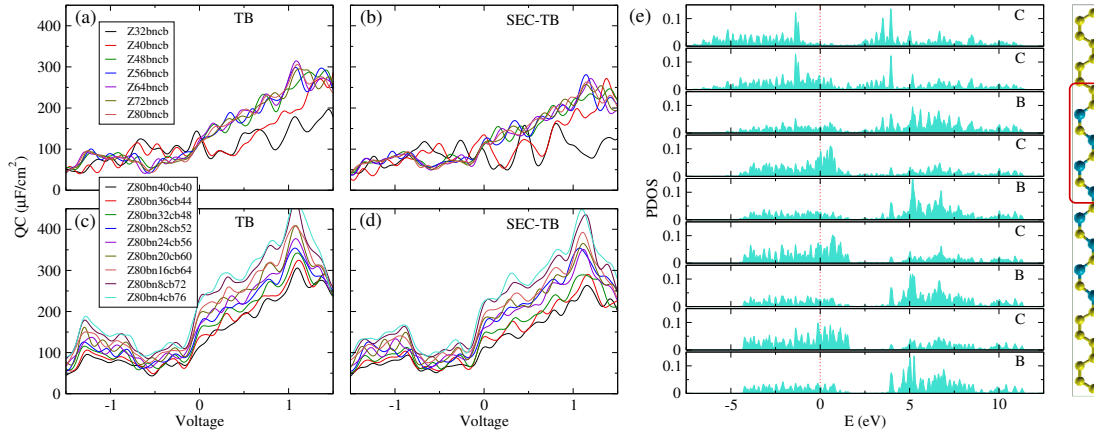
Figure 6.9: Quantum capacitance of ZZ interfaced hBN-hBC planar $z = 0$ configuration with increasing width but keeping hBC/hCN and hBN/Gr ration same using transfer (a) TB and (b) SEC-TB parameters. Fixing a total width but increasing hBC/hCN and decreasing hBN/Gr widths (c) TB and (d) SEC-TB quantum capacitances. (e) PDOS of a Gr-hBC ZZ interfaced planar $z = 0$ structure.

interface as seen in Fig.6.4(e,g). Quantum capacitance is computed for $z \neq 0$ configurations and shown in Fig.6.7(e-h). With ZZ interface, we found that Gr-hBC and Gr-hCN both are magnetic in nature but hBN-hCB and hBN-hCN are not. We also calculated the quantum capacitance for $z = 0$ configurations which are shown in Fig.6.8(a-d) for both DFT and G_0W_0 levels and as expected hBC embedded systems have higher capacitance value than hCN embedded systems. As evident from Fig.6.8(a,b) the self-energy correction for the inherently planar Gr-hBC and hBN-hBC superlattices leads to increased variation in values of capacitance but retains the overall high value.

We next calculated TB parameters at the DFT as well as DEF+G_0W_0 level for the smallest planar ($z = 0$) unitcells considered as shown in Fig.6.4(e-h). We subsequently mapped TB and SEC-TB parameters from ZGNR reference systems to larger ZGNR target systems. We consider two different types of ZZ interfaced target systems (i) wider stripes with equal hBC/hCN and hBN/Gr width and (ii) stripes with fixed total width with increasing hBC/hCN width and decreasing BN/Gr width. We calculted quantum capacitance for both types of systems in TB as well as in SEC-TB levels which are shown in Fig.6.9(a-d). We note that for former category
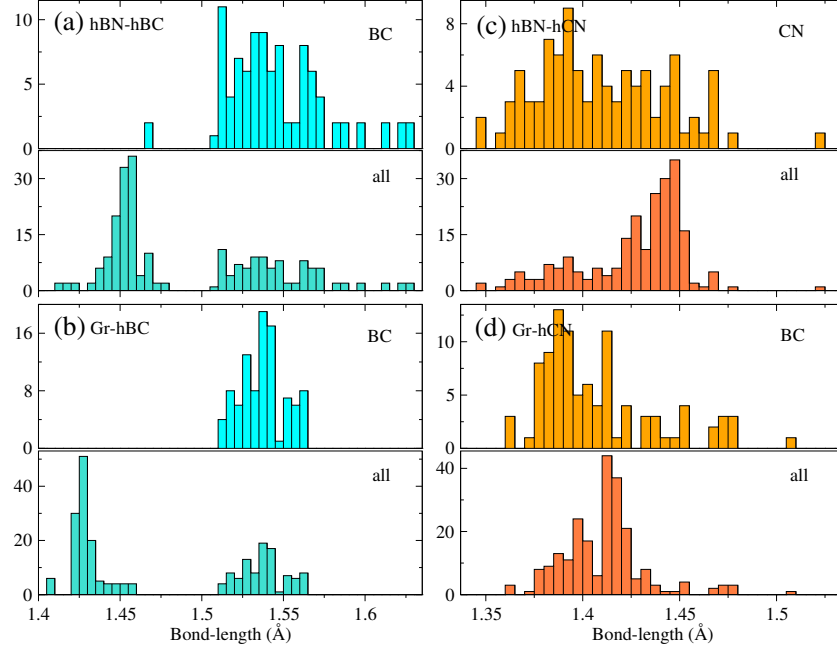
Figure 6.10: Bond-length distribution (all bonds along with BC or CN bonds) of (a) hBN-hBC, (b) Gr-hBC, (c) hBN-hCN and (d) Gr-hCN triangular 9x9 supercells presented in Fig.6.4(i-l).

after a critical width the quantum capacitance value does not increase with increasing width which can be seen in Fig.6.9(a,b), but the quantum capacitance value increases for later case where we increase hBC/hCN width and decrease hBN/Gr width shown in Fig.6.9(c,d). These results suggests that the qunatum capacitance of the stripes are simply proportional to the width of the hBC/hCN region. To understand the source of quantum capacitance we perform PDOS calculations for GrCB system as an example. We see in Fig.6.9(e) that the major contribution to DOS at Fermi energy is rendered from the $2p_z$ electrons of the C atom in the hCB region. These results suggests that stripe super-lattices can indeed be viable layered structures for effective utilization of the metallic paradigm offered by hBC in particular.

Among type 2 systems, we consider interconnected triangular hCB/hCN islands embedded in Gr/hBC forming honeycomb super-lattice as evident in Fig.6.4(i-l). The distribution of bond-length ploted in Fig.6.10 indicates that the Gr-hBC super-lattice is likely to be structurally the most stable among the super-lattices consid-
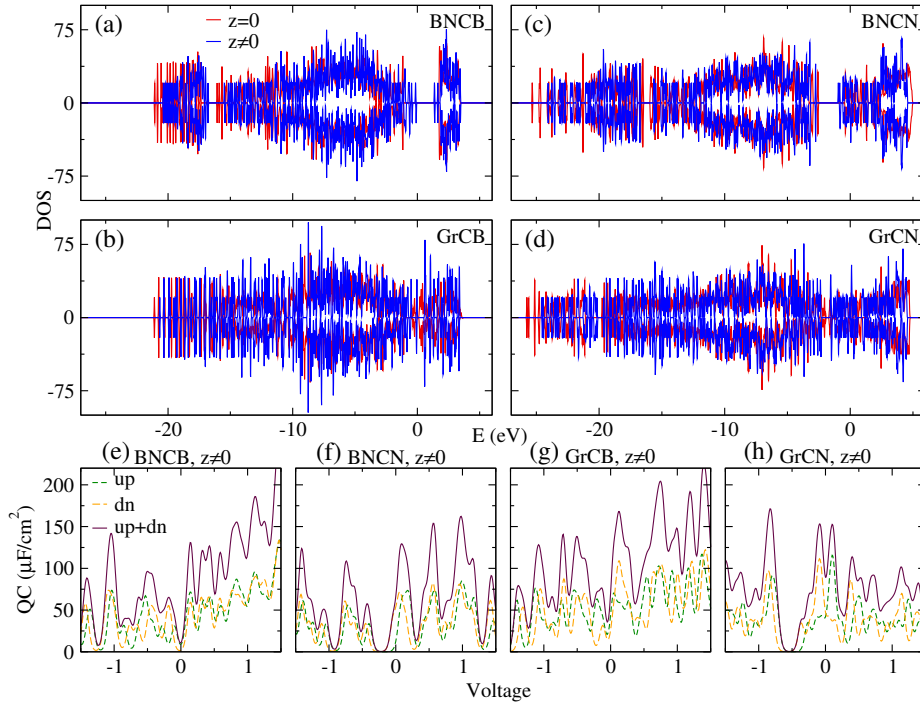
Figure 6.11: DOS of 9x9 hetero-structures with both $z \neq 0$ and $z = 0$ configurations
(a) hBN-hBC, (b) hBN-hCN, (c) Gr-hBC and (d) Gr-hCN and quantum capacitance
of $z \neq 0$ (e) hBN-hBC, (f) hBN-hCN, (g) Gr-hBC and (h) Gr-hCN systems.

ered. We calculated the DOS of such systems for both $z \neq 0$ as well as $z = 0$
and found that the nature of DOS largely remains unaltered for both the cases, as
seen in Fig.6.11(a-d). Quantum capacitance for $z \neq 0$ case for all the super-lattices
are shown in Fig.6.11(e-h). We consistently found that the capacitance values are
higher for super-lattices embedding hBC triangles than those embedding hCN tri-
angles. We also found that all the systems are magnetic in nature and a clear spin
separation exists for quantum capacitance across the Fermi energy.

Having calculated quantum capacitance at the DFT level it was computationally
impossibly expensive to calculate self-energy correction to KS single particle levels of
the super-lattices within the GW approximation. Motivated by the similarity in the
DOS with $z \neq 0$ as well as $z = 0$, we considered planar (i.e., $z = 0$ configurations)
9x9 supercell hBC and hCN embedded in hBN/Gr like shown in Fig.6.4(i-l) and used
our WC based mapping scheme described in Chapters 4 and 5 to transfer self-energy
corrected TB parameters computed in the HAWO basis (described in Chapters 3
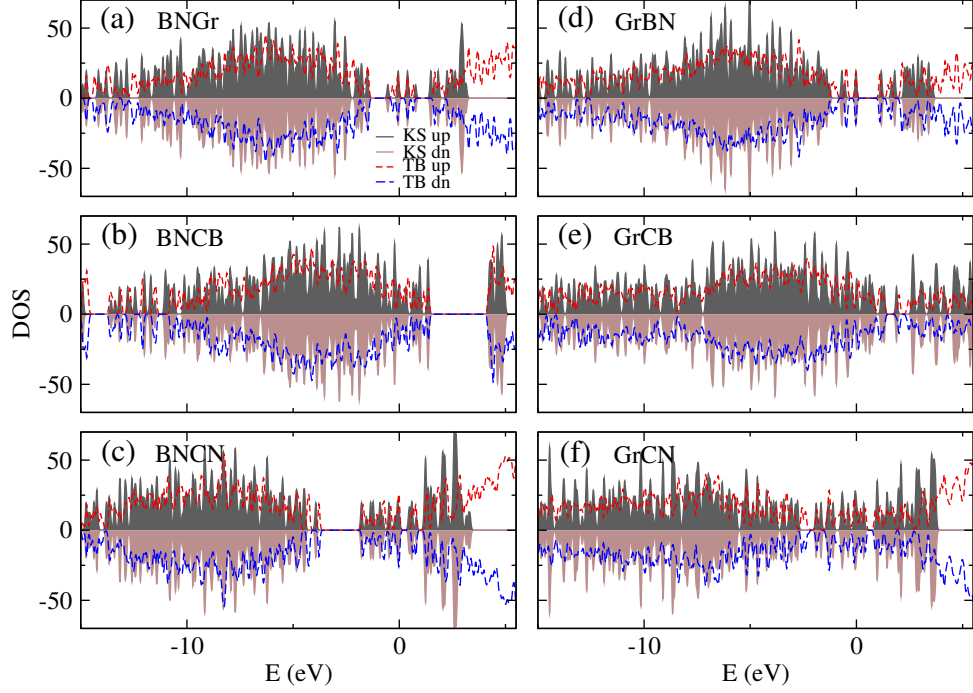
Figure 6.12: Comparision of DFT DOS and DOS calculated with transferring the TB parameters from ZZ interfaced systems of 9x9 planar (a)hBN-Gr, (b) hBN-hBC, (c) hBN-hCN, (d) Gr-hBN, (e) Gr-hBC and (f) Gr-hCN $z = 0$ hybrids.

and 4) in the planar stripe super-lattices (type 1) where the unitcell is considerably smaller to allow explicit computation of self-energy correction at the G_0W_0 level. We also explicitely calculate the DFT DOS for the same and found that the DOS match with transfered TB parameters at the DFT level to be reasonable as shown in Fig.6.12. In Fig.6.13(a,b) we ploted DOS and quantum capacitance calculated from the electronic structure computed with the transferred self-energy corrected TB parameters respectively. Following the reasonable match of DFT DOS and DOS calculated from transfer the TB parameters to the 9x9 super-cells we further considered a 19x19 supercell and calculated DOS and quantum capacitance using the transfered TB parameters, rendering an effectively gap-less regime of constant quantum capacitance across Fermi energy for super-lattices with embedded hCB, as shown in Fig.6.13(c,d).
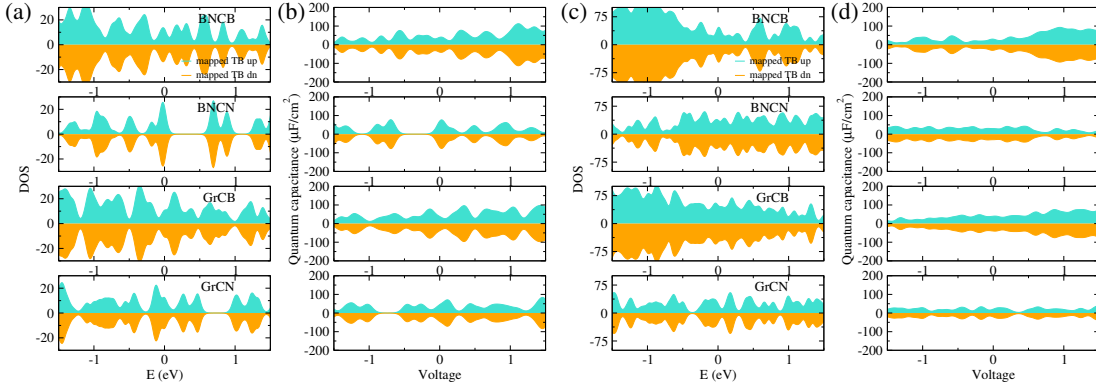
Figure 6.13: (a) DOS and corresponding (b) quantum capacitance of 9x9 planar $z = 0$ hybrids by transferring the SEC-TB parameters from ZZ interfaced systems. Similar (c) DOS and corresponding (d) quantum capacitance of 19x19 planar $z = 0$ hybrids.

6.5 Conclusions

In this chapter we have presented a survey of the prospect of Gr/hBN-hBC/hCN hybrids super-lattices as possible candidates for capacitor electrodes. Specifically we find the Gr-hBC super-lattices to be the most promising candidate which offer quantum capacitance values above 100 $\mu F/cm^2$ at room temperature. Results presented in this chapter also indicates the general possibility of stable planar heterostructures incorporating hBC for electrode applications in devices. This chapter also demonstrate the efficacy of the proposed scheme of bottom up transfer of TB parameters to systems of experimentally realizable length-scales.

Chapter 7

Self-energy correction through model the Coulomb hole term

7.1 Introduction

In this concluding chapter I present a work in progress. The content of the work
presented here merits a separate chapter because the approach to computionally
ease computation of self-energy correction proposed here is thematically different
than that presented in earlier chapters.

From the results presented in previous chapters, it is clear that for covalent sys-
tems the sptatial range of self-energy correction to tight-binding(TB) parameters
largely spans upto the third nearest neighbour. This prompts us to think whether
we can spatially account for self-energy correction in a localized basis which can be
computationally less expensive than that in terms of periodic wave-functions. In
this direction we have started with deriving a simple model for the Coulomb hole
term based on analytics wave-functions. We have accomplished the objective par-
tially so far only in one dimension. However we feel that our limited findings bear
the promise of feasibility of our approach in real system of atoms in three dimensions.

The GW approximation describe in Chapter 2 naturally incorporates the complicated many-electron effects through a self-energy operator. The GW approximation is systematically formulated from the MBPT[122,123,124] first by Hedin in 1965[4] then a detailed review is done by Hedin along with Lundqvist in 1969.[5] However, due to the computational difficulties it took almost two decades for numerical simulations to be done following their prescription for real materials by Hybertsen and Louie in their two remarkable papers.[6,41] Almost at the same time, during the mid eighties, Godby et al.[185] also published similar results. However, the calculation of the matrices/kernels of the GW formalism is a computationally challenging task in terms of implementation as well as computation. As a result, prediction of the self-energy corrected electronic structures for real systems took a long time to come in general practise and a still a far cry for systems beyond few tens of atoms unless we have access to one of the largest super-computers of the day.

7.2   Methodological details

As described in Chapter 2, wave functions and energies of a quasi-particle in a inhomogeneous many-particle system can be obtained by solving the Dyson equation

$$(-\frac{1}{2}\nabla^2 + V_{ext} + V_H)\psi_n(x) + \int \Sigma(x, x', E_n)\psi_n(x')dx'$$
$$= E_n\psi_n(x) \tag{7.1}$$

where the first term is the kinetic energy operator, V_{ext} is the external potential to the system due to ions, V_H is the electron-electron repulsive Coulomb potential and Σ is the non-local, non-Harmitian and energy dependent self-energy operator which dynamically incorporate many-electron interactions beyond V_H.

To solve the quasi-particle equation(7.1) we need to first calculate the self-energy operator Σ and for that a set of equations (which are derived in Chapter 2) was

formulated by Hedin as:

$$\chi(1,2) = -i \int G(1,3)\Gamma(3,4,2)G(4,1^+)d(34) \tag{7.2}$$

$$\epsilon(1,2) = \delta(1,2) - \int v(1,3)\chi(3,2)d(3) \tag{7.3}$$

$$W(1,2) = \int \epsilon^{-1}(1,3)v(3,2)d(3) \tag{7.4}$$

$$\Sigma(1,2) = i \int G(1,3)\Gamma(3,2,4)W(4,1^+)d(34) \tag{7.5}$$

$$\Gamma(1,2,3) = \delta(1,2)\delta(1,3) + \int \frac{\delta\Sigma(1,2)}{\delta G(4,5)}$$
$$G(4,6)G(7,5)\Gamma(6,7,3)d(4567) \tag{7.6}$$

where, $1 \equiv (x_1, \sigma_1, t_1)$ and 1^+ indicates that $t_1 \to t_1 + \eta$.

As apparent, for interacting electrons where the bare Coulomb repulsion v is non-zero, these equations are in principle to be solved in a self-consistently, starting with the construction of single-particle Green's function G as:

$$G(x, x', E) = \sum_n \frac{\phi_n(x)\phi_n^*(x')}{E - E_n - i\eta} \tag{7.7}$$

where $\eta = 0^+$ for $E_n < \mu$ and $\eta = 0^-$ for $E_n > \mu$, μ being the chemical potential. Followed successively by calculation of the irreducible polarizability χ, the dielectric function ϵ, and the screened interaction W, leading finally to the self-energy operator Σ and the vertex function Γ. The self-energy operator Σ can be used again to construct the new Green's function as $G = G_0 + G_0\Sigma G$ which can start a new iteration. In GW approximation we use the zeroth order of W due to the truncation of the vertex function Γ up to its first term[equation(7.6)] implying:

$$\Gamma(1,2,3) = \delta(1,2)\delta(1,3) \tag{7.8}$$

With this approximation, Fourier transfrom of Hedin's equations simplify as:

$$\chi(x, x', E) = -\frac{i}{2\pi} \int G(x, x', E - E')G(x, x', E')dE' \tag{7.9}$$

$$\epsilon(x, x', E) = \delta(x - x') - \int v(x, x'')\chi(x'', x', E)dx'' \tag{7.10}$$

$$W(x, x', E) = \int \epsilon^{-1}(x, x'', E)v(x'', x')dx'' \tag{7.11}$$

$$\Sigma(x, x', E) = \frac{i}{2\pi} \int G(x, x', E - E')W(x, x', E')e^{-i\eta E'}dE' \tag{7.12}$$

where, $\eta = 0^+$.

Referring to Lehman representation reviewed in Chapter 2, we recall spectral weight function $A(x, x', E)$ as

$$A(x, x', E) = \frac{1}{\pi}|\text{Im}\, G(x, x'; E)| \tag{7.13}$$

implying:

$$G(x, x', E) = \int_C \frac{A(x, x', E')}{E - E' + i\eta}dE' \tag{7.14}$$

In a many-electron system, a pole at a complex energy in the Green's function gives a quasi-particle excitation which is equivalent to a peak in the spectral weight function $A(x, x', E)$. Solution of the quasi-particle equation(7.1) gives complex E_{nk} whose real and imaginary parts render energy and lifetime of the quasiparticle.

Similar to Green's function, another spectral weight function $B(x, x', E)$ can be defined for the screened interaction W as well:

$$W(x, x', E) = v(x, x') + \int_0^\infty \frac{2E'B(x, x', E')}{E^2 - (E' - i\eta)^2}dE' \tag{7.15}$$

The spectral weight functions $A(x, x', E)$ and $B(x, x', E)$ defined in equations (7.13) and (7.15) help to split the real part of the self-energy operator Σ so called the static COHSEX term into two different terms which can be interpreted as: (1) screened exchange Σ_{SEX} term dominated by the poles of the Green's function G and (2) Coulomb hole term Σ_{COH} term dominated by the screened interaction W,

given by:[6]

$$\Sigma_{SEX}\left(x,x',E\right) = -\int_{-\infty}^{\mu} A\left(x,x',E'\right) \times$$
$$\operatorname{Re} W\left(x,x',E-E'\right) dE' \tag{7.16}$$

$$\Sigma_{COH}\left(x,x'E\right) = -\int_{-\infty}^{\infty} A\left(x,x',E'\right) dE' \times$$
$$\operatorname{P}\int_{0}^{\infty} \frac{B\left(x,x',,E''\right)}{E-E'-E''} dE'' \tag{7.17}$$

where μ is the chemical potential of the system.

In the first iteration, it is justified to assume that the self-energy operator Σ is represented by an energy independent potential $V_{E=0}$, for example the V_{XC} in DFT. With one-particle Green's function [Eqn.(7.14)] constructed using single particle states obtained within such approximation, we can write:

$$A\left(x,x',E\right) = \sum_{n} \phi_{n}(x)\phi_{n}^{*}\left(x'\right)\delta\left(E-E_{n}\right) \tag{7.18}$$

which further simplifies both the screened exchange and the Coulomb hole parts as

$$\Sigma_{SEX}\left(x,x',E\right) = -\sum_{n}^{occ} \phi_{n}(x)\phi_{n}^{*}\left(x'\right) \times W\left(x,x',E-E_{n}\right) \tag{7.19}$$

$$\Sigma_{COH}\left(x,x',E\right) = \sum_{n} \phi_{n}(x)\phi_{n}^{*}\left(x'\right) \times \mathbf{P}\int_{0}^{\infty} dE' \frac{B\left(x,x',E'\right)}{E-E_{n}-E'} \tag{7.20}$$

If the peak frequency of collective oscillations (plasmons) leading to screening is large compared to the $E-E_{n}$ then we can approximate $E-E_{n} \rightarrow 0$ which further simplifies the screened interaction to it's static limit and screened exchange becomes:

$$\Sigma_{SEX}\left(x,x'\right) = -\sum_{n}^{\infty} \phi_{n}(x)\phi_{n}^{*}\left(x'\right) W\left(x,x',E=0\right) \tag{7.21}$$

and Coulomb hole part reduces to:

$$\Sigma_{COH}(x, x') = \frac{1}{2}\delta(x - x')[W(x, x', E = 0) - v(x, x')] \quad (7.22)$$

using Eqn(7.15) and completeness condition of single particle states.

Withing such a static limit, the screened interaction W can be calculated by approximating the non-local energy dependent dielectric screening up to it's static limit $\epsilon(x, x', E = 0)$ within the random phase approximation.

To calculate $\epsilon(x, x', E = 0)$ we consider a small perturbation to the external potential V_{ext} inducing a small variation in the local density n. The two are related by the polarizability χ as:

$$\delta n(x) = \int \chi(x, x')\delta V_{ext}(x')dx' \quad (7.23)$$

Similarly we can define independent particle polarizability χ_0 as

$$\delta n(x) = \int \chi_0(x, x')\delta V_{tot}(x')dx' \quad (7.24)$$

where, $\delta V_{tot}(x) = \delta V_{ext}(x) + \delta V_{scr}(x)$ in the interacting regime. The screening of $\delta V_{ext}(x)$ by $\delta V_{scr}(x)$ is a result of correlation, of which, only the static version is being considered here.

The screening potential v_{scr} has two components:

$$V_{scr}(x) = V_H + V_{xc} = e^2 \int \frac{n(x')}{|x - x'|}dx' + \frac{\delta E_{xc}}{\delta n(x)} \quad (7.25)$$

implying:

$$\delta V_{scr}(x) = e^2 \int \frac{\delta n(x')}{|x - x'|}dx' + \frac{\delta^2 E_{xc}}{\delta n(x)\delta n(x')}\delta n(x') \quad (7.26)$$

Substituting $\delta V_{scr}(x) + \delta V_{ext}(x)$ for $\delta V_{tot}(x)$ in (7.24) using (7.26) and (7.23) we can

write the χ in terms of χ_0 as:

$$\chi = (1 - \chi_0 V_c - \chi_0 K_{xc})^{-1}\chi_0 \tag{7.27}$$

In random-phase approximation (RPA)[41] the exchange-correlation kernel K_{xc} is set to zero.

The inverse of dielectric function within the RPA defined as:

$$\epsilon_{RPA}^{-1} = \frac{\delta V_{tot}}{\delta V_{ext}} = \frac{\delta V_{ext} + \delta V_{scr}}{\delta V_{ext}} = 1 + V_c \chi \tag{7.28}$$

or

$$\epsilon_{RPA}^{-1} = 1 + V_c(1 - \chi_0 V_c)\chi_0 \iff \epsilon_{RPA} = 1 - V_c \chi_0 \tag{7.29}$$

With the one-particle Green's function constructed from single particle states [see Eqn.(7.7)] we can calculate the independent particle polarizability following the Eqn.(7.9) as:

$$\chi_0(x, x', E) = -\frac{i}{2\pi} \int \left\{ \sum_n \frac{\phi_n(x)\phi_n^*(x')}{E' - E_n - i\eta} \times \right. \\ \left. \sum_{n'} \frac{\phi_{n'}(x)\phi_{n'}^*(x')}{E - E' - E_{n'} - i\eta} \right\} dE' \tag{7.30}$$

using contour integration and introducing the Fermi factor f_n, the above equation simplifies as:

$$\chi_0(x, x', E) = \sum_{n,n'} \frac{f_n(1 - f_{n'})}{E_n - E_{n'} - E} \left[\phi_n^*(x)\phi_{n'}(x)\phi_{n'}^*(x')\phi_n(x') + c.c \right] \tag{7.31}$$

In practice however mostly it is the static $\epsilon(x, x', E = 0)$ which is calculated explicitly extended to finite energies using a generalized plasmon-pole (GPP) model based on generic analytic properties of dielectric matrices.

7.2.1   Our approach

Our aim till now has been to see if a simple explicit construction of the COH can be worked out at the static limit, and check the effectiveness of such construction. We consider an inverted Gaussian potential for our model V_{ext} in one dimension.

$$V_{ext}(x) = -A_0 e^{-\frac{\alpha(x-\beta)^2}{2\gamma^2}} \tag{7.32}$$

where, A_0 is depth of the potential, β is the peak position and γ defines the width of the potential.
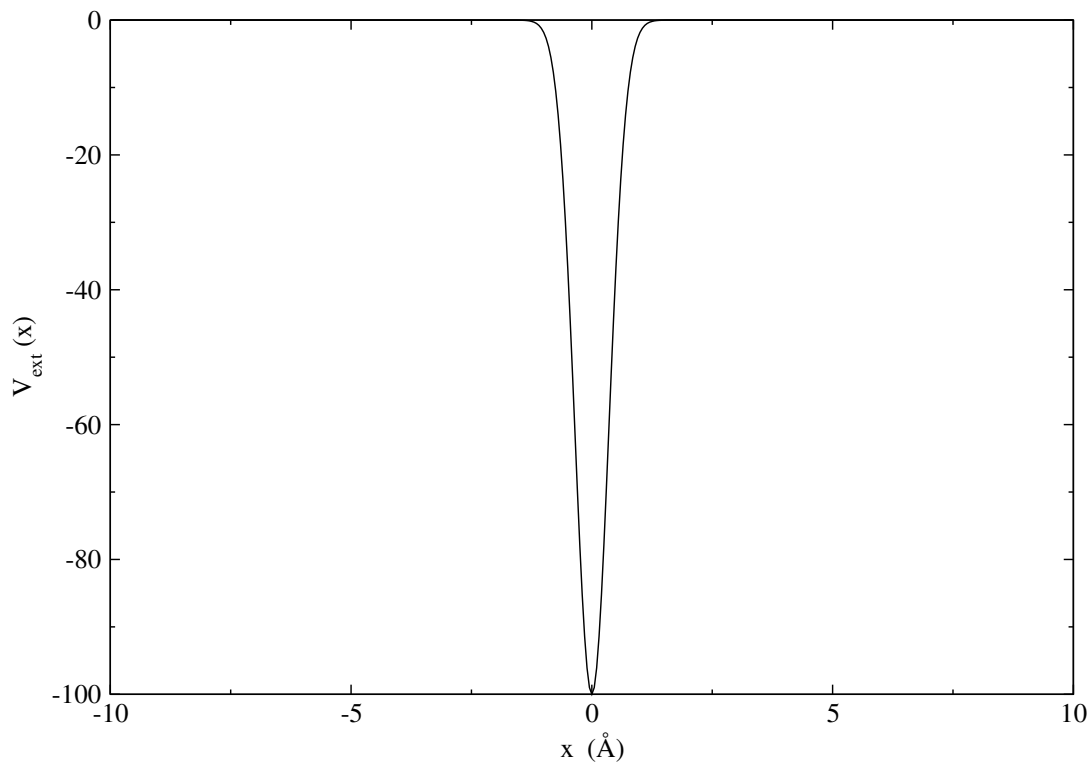

Figure 7.1: Inverted Gaussian potential

For simplicity we consider spinless Fermions in this work. We also consider $k = 0$ case only for this work. First we calculate the independent particle polarizability matrix in static lilimt (i.e., by setting $E = 0$ in equation(7.31)) using the single-particle eigenvalues and eigen functions obtained by solving the Schrodinger
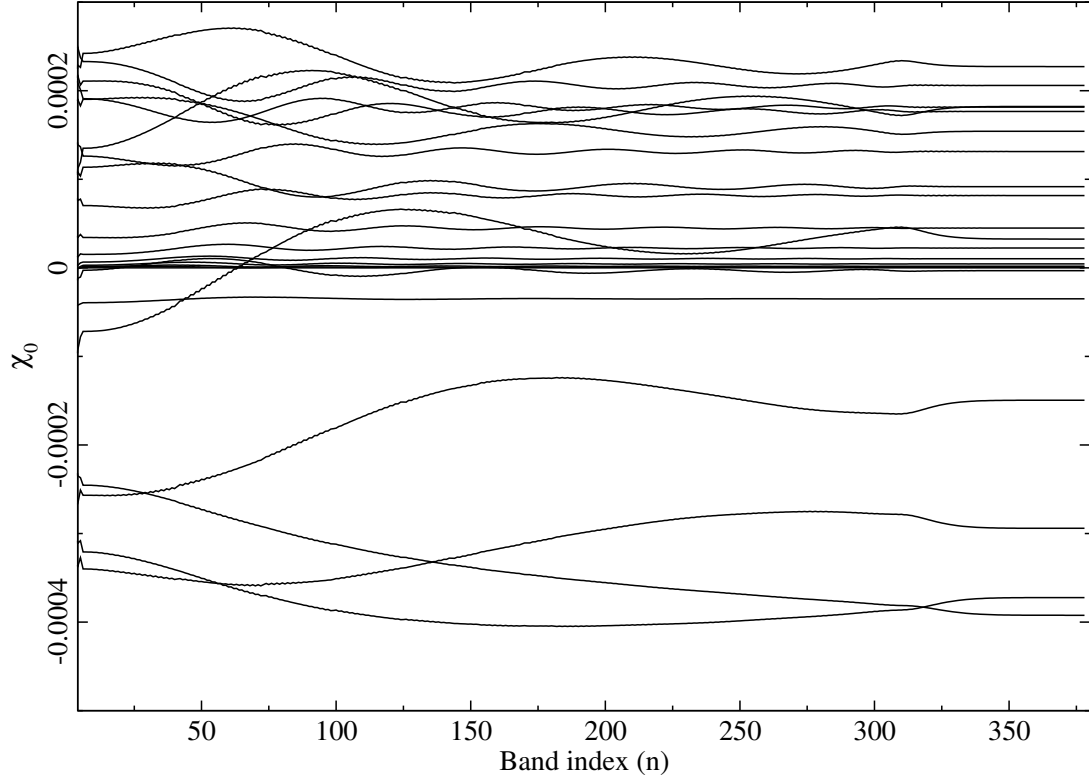
Figure 7.2: Convergence of χ_0 with respect to the bands (n). The dotted line in Fig.7.3(a) indicates the elements of χ_0 which are ploted here.

equation self-consistently for one electron with a Coulomb repulsion term.

Convergence of different elements of χ_0 matrix at the static limit is shown in Fig.[7.2]. We have ploted the elements of χ_0 for 3 electrons in well and as evident from the plot that a lot of empty states required to converge χ_0.

Contour plots of χ_0 shown in Fig.[7.3](a) and (c) for 2 and 3 electrons respectively, which indicate a rather complicated structure with systematic fluctuation about the centre of external potential with few nodes. Total polarizability χ is computed from equation(7.27) within the RPA approximation and a contour plot is shown in Fig.[7.3](b,d) for 2 and 3 electrons.

As evident from Fig.[7.3], the structure of χ_0 and χ are similar owing to the magnitude of χ_0 being much less than 1.

We calculate the RPA dielectric function at static limit using equation(7.29) and then compute the screened interaction W. Subsequently, screened exchange and the COH parts of Σ are calculated using equation(7.21) and equation(7.22) respectively.
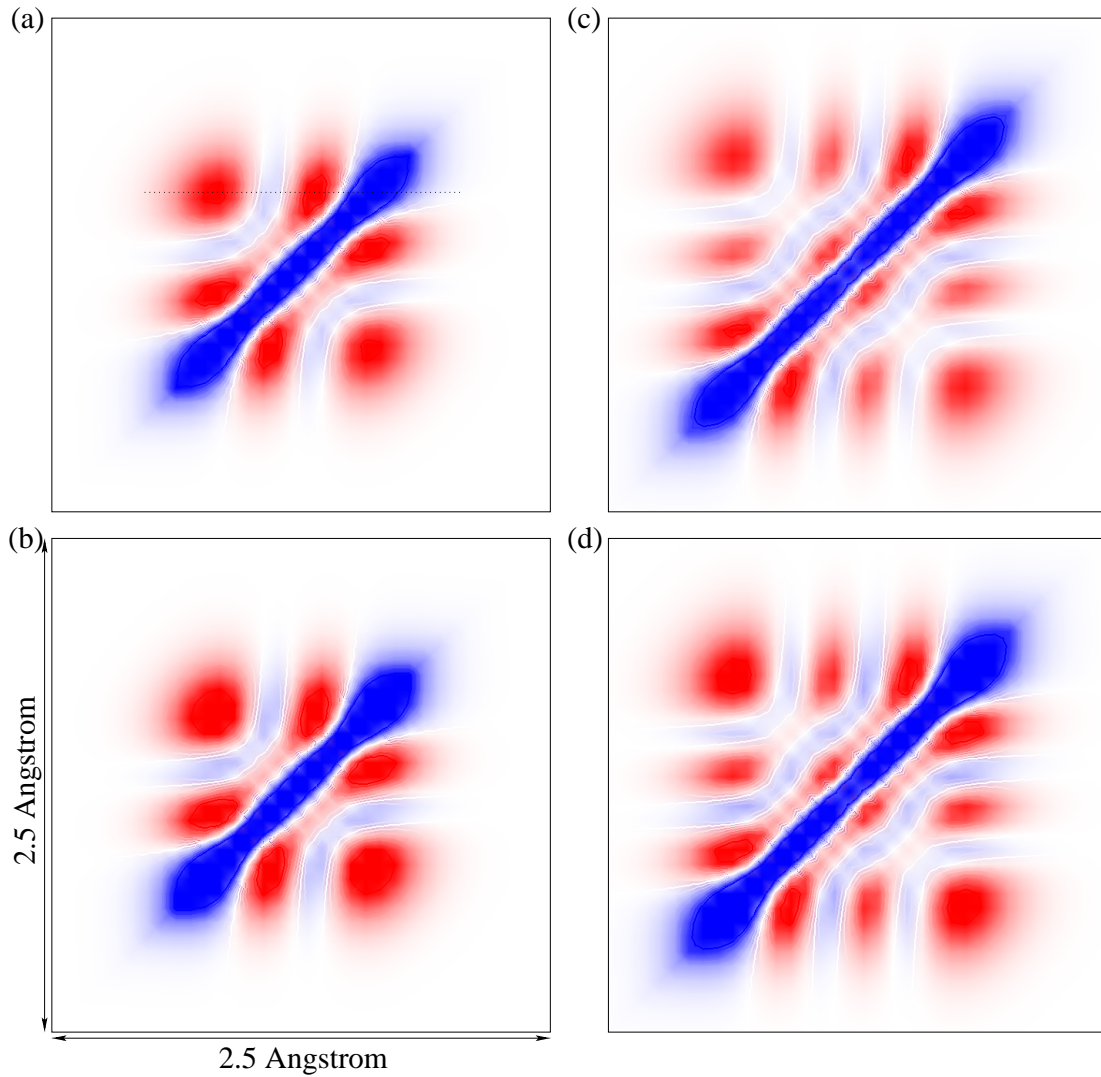
Figure 7.3: Contour plot of (a) χ_0 and (b) χ for 2 electrons in a well. Contour plot of (c) χ_0 and (d) χ for 3 electrons in a well.

In Fig.[7.4](a) and (b) contour plots of COH is shown for 2 and 3 electrons respectively. To understand the structure of the COH we ploted $\Sigma_{COH}(x, x')$ for different x values with by varying x' which is shown in Fig.[7.5] for 2 and 3 electrons. As evident in Fig.[7.5](a,b), the inherent structure of the COH has systematic variation with deviation of x from the centre of the potential. Such a systematic structure of the COH appears to suggest that the basic nature of COH may be reproducible using any analytic bound state corresponding to potential of same symmetry as that of the original V_{ext}.

To test the idea we considered simple harmonic oscillator potential and derived
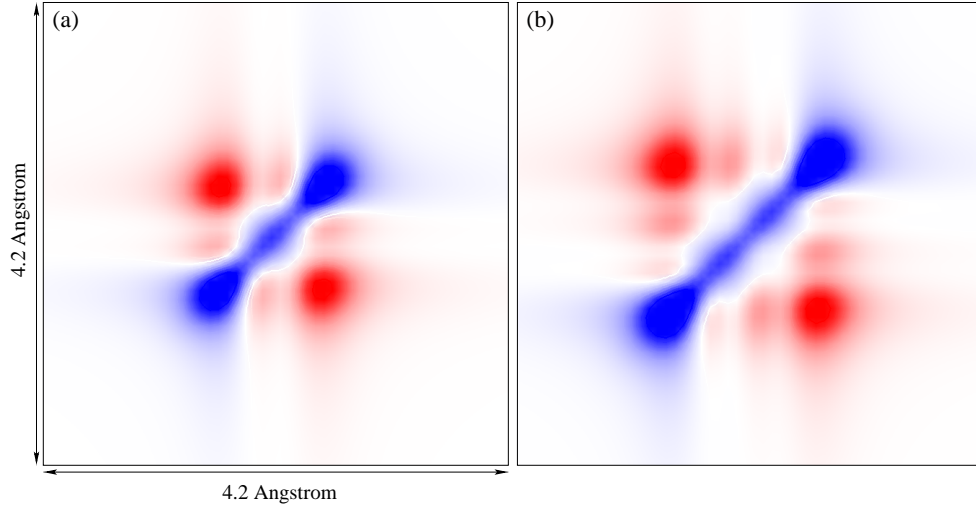
Figure 7.4: Contour plot of core region of the COH part of self-energy operator for (a) 2 and (b) 3 electrons in a single well.
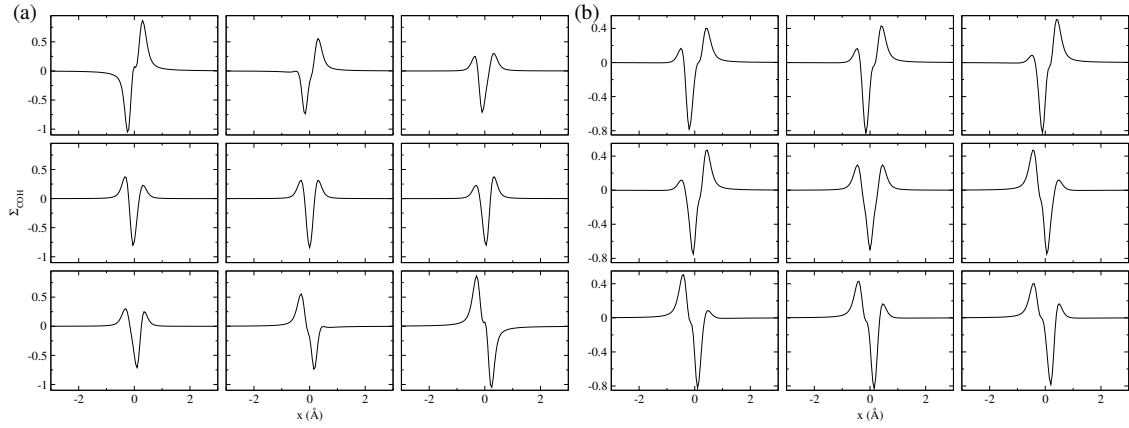
Figure 7.5: Structure of the Coulomb hole part of self-energy operator for (a) 2 and (b) 3 electrons in a single well.

analytical expressions for the Coulomb hole term using the analytic eigen functions. We start with writing the wave functions of the simple harmonic oscillator:

$$\phi_n^{HO}(x) = \left(\frac{\zeta^2}{\pi}\right)^{1/4} \frac{1}{\sqrt{2^n n!}} H_n(\zeta x) e^{-\frac{\zeta^2 x^2}{2}} \tag{7.33}$$

with $n = 0, 1, 2, ...$, where H_n is the Hermite polynomials.

To calculate χ_0 at first we approximated the summation from HOMO-1 to LUMO+1 states in Eqn.(7.31) since the states near Fermi level are expected to
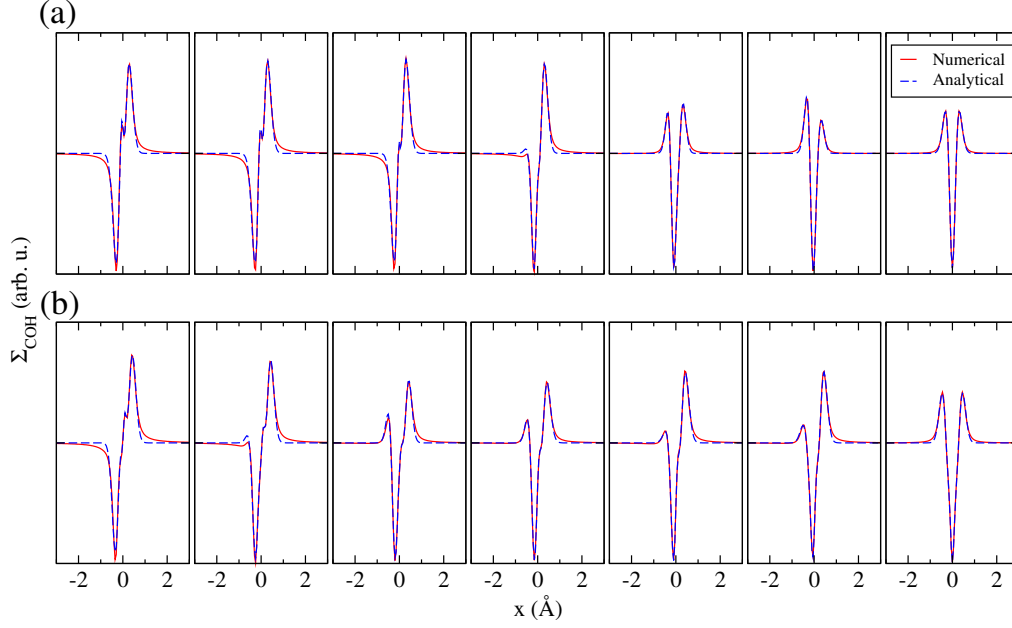
Figure 7.6: Fitted (analytical) along with numerical Coulomb hole term (Σ_{COH}) for (a) 2 and (b) 3 electrons in a well.

contribute the most to the summation over $\{n, n'\}$ owing to the lowering of the denominator as we approach the Fermi energy from the occupied and the unoccupied manifolds. Using the χ_0 the screened interaction within RPA is written as:

$$W = \epsilon^{-1}V_c = (1 + V_c\chi_0)V_c = V_c + V_c\chi_0 V_c \tag{7.34}$$

which renders COH as:

$$\Sigma_{COH} \simeq W - V_c = V_c\chi_0 V_c. \tag{7.35}$$

We compute the Σ_{COH} using the wave functions of the simple harmonic oscillator [Eqn.(7.33)] in χ_0 [equation(7.31)] leading to an analytical form for COH as:

$$\begin{aligned} \Sigma_{COH}\left(x, x'\right) = & \frac{1}{2}\delta\left(x - x'\right)v\left(x, x'\right)^2 \times \\ & Ae^{-\zeta^2\left(x^2 + x'^2\right)}\sum_{i=0}^{2N}\left(B_i x^i\right)\left(B_i' x'^i\right) \end{aligned} \tag{7.36}$$

where, N is the number of electrons present in the system. The coefficients A, B and B' contain all the constants which accumulate as we derive the above equation
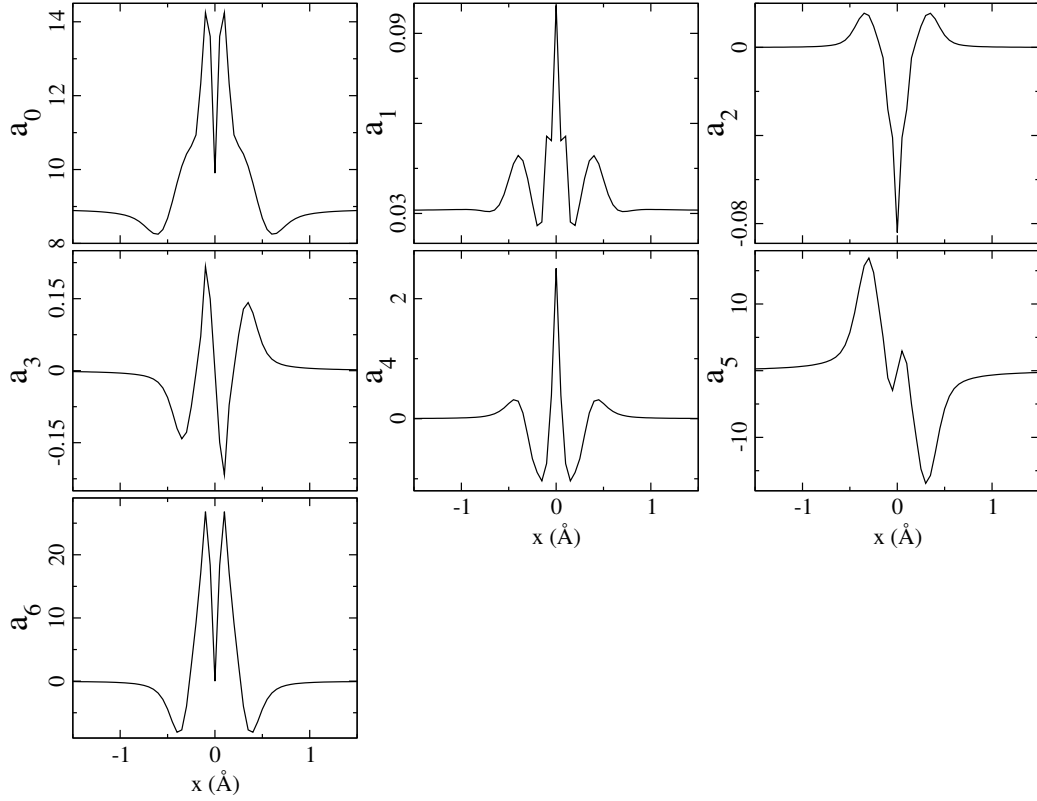
Figure 7.7: Variation of the fitted coefficients of the COH for 2 eletrons in a well using the Eqn.7.37.

from Eqn.(7.33).

For each x' of the $\Sigma_{COH}(x, x')$ we get a function from the above equation as

$$f_{COH}(x) = \frac{e^{-a_0 x^2}}{a_1 + |x|^2} \sum_{i=0}^{2N} a_{2+i} x^i \qquad (7.37)$$

which represents the inherent structure of the Coulomb hole term.

We have now analytical function(7.37) to try if we can fit the Σ_{COH} for the given V_{ext}. In Fig.[7.6](a) and (b) we have plotted the numerical and fitted Σ_{COH} with 2 and 3 electrons respectively confined by the chosen V_{ext} and we can see that the fitting is reasonable. The ability to fit Σ_{COH} obtained using eigenstates HOMO-1 to LUMO+1 of the harmonic oscillator, to that of the converged Σ_{COH} of the given V_{ext}, implies the possibility to arrive at simple analytical models for the COH which can be incorporated in an appropriate localized basis. The variation of the fitting

parameters as a function of x plotted in Fig.7.7 for the V_{ext} considered also implies a systematic dependence which can be parametrised and adopted in a multiple well scenario representing a system of atoms.

7.3   Future direction

Motivated by the reproducibility[Fig.(7.6)] of the Coulomb-hole by fitting the analytic expression[Eqn.(7.37)] based on COH calculated with states from HOMO-1 to LUMO+1 of a harmonic oscillator and the systematic variation of fitting coefficients we next plan to constrct analytic approximations for the fitting parameteers and check for their generality over a representative set of V_{ext}. The next step will be to extend the construction of the model COH for multiple wells and then to three dimensions. Our ultimate objective in this direction is to involve the hybrid atomic Wannier orbitals (HAWO) proposed in Chapter 4 in construction of model COH. Our intution is based on our findings that the self-energy correction to the tight-binding parameters are rather local and might predominantly determined by the immidiate neighborhood. HAWOs being naturally directed towards coordinations should be appropriate for the purpose. Further it will be imperative to build in the construction of COH within a pseudopotential constructed with the hybrid atomic orbitals (HAO) of isolated atoms.

7.4   Conclusions

In conclusion, we present an inexpensive method to model the Coulomb hole (COH) part of the self-energy operator Σ in one dimension. We have used an inverted Gaussian potential and explicitly calculated the screened exchange and COH parts of Σ within the random phase approximation. We have demonstrated that the COH of the chosen V_{ext} can be fitted to a model COH constructed with few eigenfunctions of a simple harmonic oscillator about the Fermi energy. The fitting parameters have

systematic dependence on the chosen parameters of the chosen V_{ext}. The accuracy of the fitting suggests the possibility to construct model COH for the real system of atoms in some appropriate localized basis, which can possible be incorporated either as a route towards computationally inexpensive construction of χ within the GW framework, or perhaps at the same footing as the pseudo-potentials.

References

[1] Pierre Hohenberg and Walter Kohn, *Physical review*, **136**, B864 (1964).

[2] Walter Kohn and Lu Jeu Sham, *Physical review*, **140**, A1133 (1965).

[3] Kostya S Novoselov et al., *science*, **306**, 666–669 (2004).

[4] Lars Hedin, *Physical Review*, **139**, A796 (1965).

[5] Lars Hedin and Stig Lundqvist. "Effects of electron-electron and electron-phonon interactions on the one-electron states of solids". In: *Solid state physics*. Vol. 23. Elsevier, 1970, 1–181.

[6] Mark S Hybertsen and Steven G Louie, *Physical Review B*, **34**, 5390 (1986).

[7] Thomas A Niehaus et al., *Physical Review A*, **71**, 022508 (2005).

[8] Jan Wilhelm et al., *The journal of physical chemistry letters*, **9**, 306–312 (2018).

[9] Giuseppe Del Re, *Theoretica chimica acta*, **1**, 188–197 (1963).

[10] Joydeep Bhattacharjee and Umesh V Waghmare, *Physical Review B*, **71**, 045106 (2005).

[11] Gregory H Wannier, *Physical Review*, **52**, 191 (1937).

[12] Neil W Ashcroft, N David Mermin, et al. *Solid state physics*. 1976.

[13] John C Slater and George F Koster, *Physical Review*, **94**, 1498 (1954).

[14] GF Koster and JC Slater, *Physical Review*, **95**, 1167 (1954).

[15] ND Drummond et al., *Physical review letters*, **95**, 096801 (2005).

[16] C Delerue, M Lannoo, and G Allan, *Physical review letters*, **84**, 2457 (2000).

[17] Tamás Demján et al., *The Journal of chemical physics*, **141**, 064308 (2014).

[18] Douglas R Hartree. "The wave mechanics of an atom with a non-Coulomb central field. Part I. Theory and methods". In: *Mathematical Proceedings of the Cambridge Philosophical Society*. Vol. 24. 1. Cambridge university press. 1928, 89–110.

[19] Vladimir Fock, *Zeitschrift für Physik*, **61**, 126–148 (1930).

[20] M. Born and R. Oppenheimer, *Annalen der Physik*, **389**, 457–484 (1927).

[21] J. C. Slater, *Phys. Rev.* **34**, 1293–1322 (1929).

[22] L. H. Thomas, *Mathematical Proceedings of the Cambridge Philosophical Society*, **23**, 542–548 (1927).

[23] E. Fermi, *Zeitschrift für Physik*, **48**, 73–79 (1928).

[24] DR Hamann, M Schlüter, and C Chiang, *Physical Review Letters*, **43**, 1494 (1979).

[25] David Vanderbilt, *Physical review B*, **41**, 7892 (1990).

[26] Charles G Broyden, *IMA journal of applied mathematics*, **6**, 222–231 (1970).

[27] Roger Fletcher, *The computer journal*, **13**, 317–322 (1970).

[28] Donald Goldfarb, *Mathematics of computation*, **24**, 23–26 (1970).

[29] David F Shanno, *Mathematics of computation*, **24**, 647–656 (1970).

[30] FD Murnaghan, *Proceedings of the national academy of sciences of the United States of America*, **30**, 244 (1944).

[31] Kurt R. Brorsen et al., *The Journal of Physical Chemistry Letters*, **8**, 2076–2081 (2017).

[32] Viktor N. Staroverov et al., *Phys. Rev. B*, **69**, 075102 (2004).

[33] Philipp Haas, Fabien Tran, and Peter Blaha, *Phys. Rev. B*, **79**, 085104 (2009).

[34] John P Perdew, Kieron Burke, and Yue Wang, *Physical Review B*, **54**, 16533 (1996).

[35] George B Arfken and Hans J Weber. *Mathematical methods for physicists.* 1999.

[36] John C Inkson. *Many-body theory of solids: an introduction.* Springer Science & Business Media, 2012.

[37] Henrik Bruus and Karsten Flensberg. *Many-body quantum theory in condensed matter physics: an introduction.* Oxford university press, 2004.

[38] Alexander L Fetter and John Dirk Walecka. *Quantum theory of many-particle systems.* Courier Corporation, 2012.

[39] Murray Gell-Mann and Francis Low, *Physical Review*, **84**, 350 (1951).

[40] Nathan Wiser, *Physical Review*, **129**, 62 (1963).

[41] Mark S Hybertsen and Steven G Louie, *Physical Review B*, **35**, 5585 (1987).

[42] Jack Deslippe et al., *Computer Physics Communications*, **183**, 1269–1289 (2012).

[43] Younan Xia and Naomi J Halas, *MRS bulletin*, **30**, 338–348 (2005).

[44] Song-Yuan Ding et al., *Nature Reviews Materials*, **1**, 1–16 (2016).

[45] Charles M Lieber and Zhong Lin Wang, *MRS bulletin*, **32**, 99–108 (2007).

[46] Marcus Elstner and Gotthard Seifert, *Philosophical Transactions of the Royal Society A: Mathematical, Physical and Engineering Sciences*, **372**, 20120483 (2014).

[47] Nicola Marzari and David Vanderbilt, *Physical review B*, **56**, 12847 (1997).

[48] Joydeep Bhattacharjee and Umesh V Waghmare, *Physical Review B*, **73**, 121102 (2006).

[49] Xiaofeng Qian et al., *Physical Review B*, **78**, 245112 (2008).

[50] Dominik Gresch et al., *Physical Review Materials*, **2**, 103805 (2018).

[51] Stephen Carr et al., *Physical Review Research*, **1**, 033072 (2019).

[52] Arrigo Calzolari et al., *Physical Review B*, **69**, 035108 (2004).

[53] CESARE Franchini et al., *Journal of Physics: Condensed Matter*, **24**, 235602 (2012).

[54] Jeil Jung and Allan H MacDonald, *Physical Review B*, **87**, 195450 (2013).

[55] John P Perdew and Mel Levy, *Physical Review Letters*, **51**, 1884 (1983).

[56] John P Perdew and Alex Zunger, *Physical Review B*, **23**, 5048 (1981).

[57] John P Perdew, Kieron Burke, and Matthias Ernzerhof, *Phys Rev Lett*, **77**, 3865 (1996).

[58] Matteo Cococcioni, *Correlated Electrons: From Models to Materials Modeling and Simulation; Verlag des Forschungszentrum Jülich: Jülich, Germany*, (2012).

[59] Jeng-Da Chai and Po-Ta Chen, *Physical Review Letters*, **110**, 033002 (2013).

[60] Rickard Armiento and Stephan Kümmel, *Physical Review Letters*, **111**, 036402 (2013).

[61] AD Becke and Marc R Roussel, *Physical Review A*, **39**, 3761 (1989).

[62] Axel D Becke, *The Journal of chemical physics*, **98**, 1372–1377 (1993).

[63] Jochen Heyd, Gustavo E Scuseria, and Matthias Ernzerhof, *The Journal of chemical physics*, **118**, 8207–8215 (2003).

[64] Giovanni Onida, Lucia Reining, and Angel Rubio, *Reviews of modern physics*, **74**, 601 (2002).

[65] Steven G Louie and Marvin L Cohen. *Conceptual foundations of materials: a standard model for ground-and excited-state properties.* Elsevier, 2006.

[66] Ferdi Aryasetiawan and Olle Gunnarsson, *Reports on Progress in Physics*, **61**, 237 (1998).

[67] Fabien Bruneval, *The Journal of Chemical Physics*, **145**, 234110 (2016).

[68] Kristian S. Thygesen and Angel Rubio, *The Journal of Chemical Physics*, **126**, 091101 (2007).

[69] Jan Wilhelm et al., *The journal of physical chemistry letters*, **9**, 306–312 (2018).

[70] D. Foerster, P. Koval, and D. Sánchez-Portal, *The Journal of Chemical Physics*, **135**, 074105 (2011).

[71] Akitaka Sawamura et al., *Journal of Applied Physics*, **121**, 235704 (2017).

[72] Jin Yu, Mikhail I Katsnelson, and Shengjun Yuan, *Physical Review B*, **98**, 115117 (2018).

[73] Irene Aguilera, Christoph Friedrich, and Stefan Blügel, *Physical Review B*, **100**, 155147 (2019).

[74] Yeongsu Cho and Timothy C Berkelbach, *The Journal of Physical Chemistry Letters*, **10**, 6189–6196 (2019).

[75] Li Yang et al., *Physical Review Letters*, **99**, 186801 (2007).

[76] Per-Olov Löwdin, *The Journal of Chemical Physics*, **18**, 365–375 (1950).

[77] Paolo Giannozzi et al., *Journal of physics: Condensed matter*, **21**, 395502 (2009).

[78] Patrik Fazekas. *Lecture notes on electron correlation and magnetism*. Vol. 5. World scientific, 1999.

[79] Linus Pauling, *Journal of the American Chemical Society*, **53**, 1367–1400 (1931).

[80] John C Slater, *Physical Review*, **37**, 481 (1931).

[81] G Doggett, *Proceedings of the Physical Society*, **86**, 393 (1965).

[82] Rev McWeeny, *Reviews of Modern Physics*, **32**, 335 (1960).

[83] G Del Re, U Esposito, and M Carpentieri, *Theoretica chimica acta*, **6**, 36–44 (1966).

[84] Alan E Reed, Larry A Curtiss, and Frank Weinhold, *Chemical Reviews*, **88**, 899–926 (1988).

[85] R McWeeny and G Del Re, *Theoretica chimica acta*, **10**, 13–22 (1968).

[86] JN Murrell, *The Journal of Chemical Physics*, **32**, 767–770 (1960).

[87] I Mayer, *The Journal of Physical Chemistry*, **100**, 6249–6257 (1996).

[88] I Mayer, *Chemical physics letters*, **242**, 499–506 (1995).

[89] a) JP Foster and F Weinhold, *Journal of the American Chemical Society*, **102**, 7211–7218 (1980).

[90] John C Slater, *Physical Review*, **36**, 57 (1930).

[91] Warren J Hehre, Robert F Stewart, and John A Pople, *The Journal of Chemical Physics*, **51**, 2657–2664 (1969).

[92] Thom H Dunning Jr, *The Journal of chemical physics*, **90**, 1007–1023 (1989).

[93] Chang-Guo Zhan and Zhen-Min Hu, *Theoretica chimica acta*, **84**, 511–520 (1993).

[94] AB Rives and F Weinhold, *International Journal of Quantum Chemistry*, **18**, 201–209 (1980).

[95] MS Gopinathan, *Journal of Molecular Structure: THEOCHEM*, **169**, 379–388 (1988).

[96] Carol A Baxter and David B Cook, *International journal of quantum chemistry*, **60**, 173–183 (1996).

[97] EF Kirkwood and DB Cook, *Theoretica chimica acta*, **44**, 139–149 (1977).

[98] Jiali Gao et al., *The Journal of Physical Chemistry A*, **102**, 4714–4721 (1998).

[99] Jingzhi Pu, Jiali Gao, and Donald G Truhlar, *The Journal of Physical Chemistry A*, **108**, 632–650 (2004).

[100] IV Popov, AL Tchougreeff, and R Dronskowski, *Low Temperature Physics*, **46**, 655–670 (2020).

[101] Michael Victor Berry, *Proceedings of the Royal Society of London. A. Mathematical and Physical Sciences*, **392**, 45–57 (1984).

[102] Raffaele Resta, *Reviews of modern physics*, **66**, 899 (1994).

[103] RD King-Smith and David Vanderbilt, *Physical Review B*, **47**, 1651 (1993).

[104] Joydeep Bhattacharjee and Umesh V Waghmare, *Physical Review B*, **73**, 121102 (2006).

[105] Jean-François Cardoso and Antoine Souloumiac, *SIAM journal on matrix analysis and applications*, **17**, 161–164 (1996).

[106] Herman H Goldstine, Francis J Murray, and John Von Neumann, *Journal of the ACM (JACM)*, **6**, 59–96 (1959).

[107] JM Foster and SFi Boys, *Reviews of Modern Physics*, **32**, 300 (1960).

[108]   Hiroshi Tatewaki and Sigeru Huzinaga, *The Journal of Chemical Physics*, **71**, 4339–4348 (1979).

[109]   R Bruce King, *Coordination Chemistry Reviews*, **197**, 141–168 (2000).

[110]   Denis Rafael Nacbar, Allan Victor Ribeiro, and Alexys Bruno-Alfonso, *Materials Research*, **17**, 1474–1476 (2014).

[111]   DM David Jeba Singh et al., *The Journal of Physical Chemistry A*, **109**, 7339–7342 (2005).

[112]   Joydeep Bhattacharjee, *The journal of physical chemistry letters*, **6**, 1653–1660 (2015).

[113]   Rita Maji and Joydeep Bhattacharjee, *The Journal of Physical Chemistry C*, **123**, 16731–16740 (2019).

[114]   Nicola Marzari et al., *Reviews of Modern Physics*, **84**, 1419 (2012).

[115]   Young-Su Lee, Marco Buongiorno Nardelli, and Nicola Marzari, *Physical review letters*, **95**, 076804 (2005).

[116]   Xiaofeng Qian, Ju Li, and Sidney Yip, *Physical Review B*, **82**, 195442 (2010).

[117]   Pino D'Amico et al., *Physical Review B*, **94**, 165166 (2016).

[118]   Luis A Agapito et al., *Physical Review B*, **93**, 125137 (2016).

[119]   Sheng-Ying Yue et al., *Physical Review B*, **95**, 085207 (2017).

[120]   Ilya V Popov et al., *Physical Chemistry Chemical Physics*, **21**, 18138–18148 (2019).

[121]   Kenneth B Wiberg, *Accounts of chemical research*, **29**, 229–234 (1996).

[122]   Murray Gell-Mann and Keith A Brueckner, *Physical Review*, **106**, 364 (1957).

[123]   Ph Nozieres and D Pines, *Il Nuovo Cimento (1955-1965)*, **9**, 470–490 (1958).

[124] Paul C Martin and Julian Schwinger, *Physical Review*, **115**, 1342 (1959).

[125] Alexander N Rudenko and Mikhail I Katsnelson, *Physical Review B*, **89**, 201408 (2014).

[126] Alexander Grüneis et al., *Physical Review B*, **78**, 205425 (2008).

[127] Jean-Yves Raty and G Galli, *Journal of Electroanalytical Chemistry*, **584**, 9–12 (2005).

[128] Jean-Yves Raty et al., *Physical review letters*, **90**, 037401 (2003).

[129] Takao Sasagawa and Zhi-xun Shen, *Journal of applied physics*, **104**, 073704 (2008).

[130] Felix Bloch, *Zeitschrift fur Physik*, **52**, 555–600 (1928).

[131] CM Goringe, DR Bowler, and E Hernandez, *Reports on Progress in Physics*, **60**, 1447 (1997).

[132] P Vogl, Harold P Hjalmarson, and John D Dow, *Journal of physics and chemistry of solids*, **44**, 365–378 (1983).

[133] C Tserbak, HM Polatoglou, and G Theodorou, *Physical Review B*, **47**, 7104 (1993).

[134] Adrian P Sutton et al., *Journal of Physics C: Solid State Physics*, **21**, 35 (1988).

[135] Leif Goodwin, AJ Skinner, and DG Pettifor, *EPL (Europhysics Letters)*, **9**, 701 (1989).

[136] CZ Wang, KM Ho, and Che Ting Chan, *Physical review letters*, **70**, 611 (1993).

[137] James L Mercer Jr and MY Chou, *Physical Review B*, **49**, 8506 (1994).

[138] I Kwon et al., *Physical Review B*, **49**, 7242 (1994).

[139] Madhu Menon and KR Subbaswamy, *Physical Review B*, **47**, 12754 (1993).

[140] Th Frauenheim et al., *Physical Review B*, **52**, 11492 (1995).

[141] Noam Bernstein and Efthimios Kaxiras, *Physical Review B*, **56**, 10488 (1997).

[142] Otto F Sankey and David J Niklewski, *Physical Review B*, **40**, 3979 (1989).

[143] JP Proot, C Delerue, and G Allan, *Applied Physics Letters*, **61**, 1948–1950 (1992).

[144] Cet Delerue, G Allan, and M Lannoo, *Physical Review B*, **48**, 11024 (1993).

[145] YM Niquet et al., *Physical Review B*, **62**, 5109 (2000).

[146] F Trani et al., *Physical Review B*, **72**, 075423 (2005).

[147] Xiaofeng Qian et al., *Physical Review B*, **78**, 245112 (2008).

[148] Arash A Mostofi et al., *Computer physics communications*, **178**, 685–699 (2008).

[149] M Heidari Saani, M Kargarian, and A Ranjbar, *Physical Review B*, **76**, 035417 (2007).

[150] Patrice Simon and Yury Gogotsi, *Nanoscience and technology: a collection of reviews from Nature journals*, 320–329 (2010).

[151] Ananthakumar Ramadoss and Sang Jae Kim, *Carbon*, **63**, 434–445 (2013).

[152] John R Miller and Patrice Simon, *Science Magazine*, **321**, 651–652 (2008).

[153] Antonino Salvatore Arico et al., *Materials for sustainable energy: a collection of peer-reviewed research and review articles from Nature Publishing Group*, 148–159 (2011).

[154] Montree Sawangphruk et al., *Carbon*, **60**, 109–116 (2013).

[155] Ming Zhou et al., *Chemical Physics Letters*, **581**, 64–69 (2013).

[156] Guoping Wang, Lei Zhang, and Jiujun Zhang, *Chemical Society Reviews*, **41**, 797–828 (2012).

[157] Patrice Simon and Yury Gogotsi, *Accounts of chemical research*, **46**, 1094–1103 (2013).

[158] Yanwu Zhu et al., *science*, **332**, 1537–1541 (2011).

[159] Maher F El-Kady et al., *Science*, **335**, 1326–1330 (2012).

[160] Xiao Huang et al., *Chemical Society Reviews*, **41**, 666–686 (2012).

[161] Yan Wang et al., *The Journal of Physical Chemistry C*, **113**, 13103–13107 (2009).

[162] Ji Chen, Chun Li, and Gaoquan Shi, *The journal of physical chemistry letters*, **4**, 1244–1253 (2013).

[163] Dale AC Brownson, Dimitrios K Kampouris, and Craig E Banks, *Journal of Power Sources*, **196**, 4873–4885 (2011).

[164] ZJ Li et al., *Applied Surface Science*, **258**, 3726–3731 (2012).

[165] Li Li Zhang and XS Zhao, *Chemical Society Reviews*, **38**, 2520–2531 (2009).

[166] Brandon C Wood et al., *The Journal of Physical Chemistry C*, **118**, 4–15 (2014).

[167] Fang Chen et al., *Journal of the American Chemical Society*, **131**, 9908–9909 (2009).

[168] Eunsu Paek et al., *The Journal of Physical Chemistry C*, **117**, 5610–5616 (2013).

[169] Chenguang Liu et al., *Nano letters*, **10**, 4863–4868 (2010).

[170] Xiaowei Yang et al., *science*, **341**, 534–537 (2013).

[171] Jung Joon Yoo et al., *Nano letters*, **11**, 1423–1427 (2011).

[172] Bong Gill Choi et al., *ACS nano*, **5**, 7205–7213 (2011).

[173] Yongcai Qiu, Xinfeng Zhang, and Shihe Yang, *Physical Chemistry Chemical Physics*, **13**, 12554–12558 (2011).

[174] Hyung Mo Jeong et al., *Nano letters*, **11**, 2472–2477 (2011).

[175] Baojiang Jiang et al., *Applied Surface Science*, **258**, 3438–3443 (2012).

[176] Li Sun et al., *Rsc Advances*, **2**, 4498–4506 (2012).

[177] Alexander J Pak, Eunsu Paek, and Gyeong S Hwang, *Carbon*, **68**, 734–741 (2014).

[178] Yi Ding, Yanli Wang, and Jun Ni, *Applied Physics Letters*, **95**, 123105 (2009).

[179] Hyoungki Park et al., *Applied Physics Letters*, **100**, 253115 (2012).

[180] Yungang Zhou et al., *The Journal of Physical Chemistry C*, **116**, 7581–7586 (2012).

[181] Sirichok Jungthawan, Sukit Limpijumnong, Jer-Lai Kuo, et al., *Physical Review B*, **84**, 235424 (2011).

[182] Natalia Berseneva et al., *Physical Review B*, **87**, 035404 (2013).

[183] Pushkar Mishra et al., *Optical Materials*, **110**, 110476 (2020).

[184] M Yeganeh et al., *Solid State Communications*, **305**, 113750 (2020).

[185] Rex W Godby, Michael Schlüter, and LJ Sham, *Physical Review B*, **37**, 10159 (1988).